ASSESSING THE IMPACT OF SPATIAL RAINFALL VARIABILITY ON THE QUANTIFICATION OF FLOOD HAZARD AND EXPOSURE: A CASE STUDY OF THE ITAJAÍ-AÇU RIVER BASIN, BRAZIL
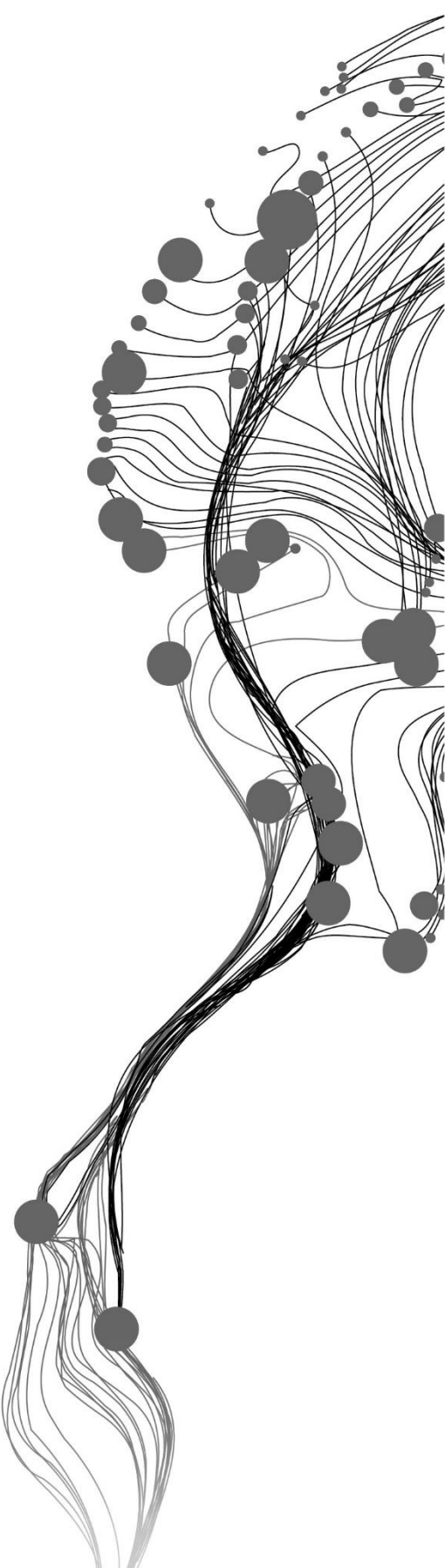
CASSIANO BASTOS MOROZ
August, 2021

SUPERVISORS:

Prof. Dr. V. G. Jetten
Dr. D. Alkema

ADVISOR:

Dr. N. C. Kingma

ASSESSING THE IMPACT OF SPATIAL RAINFALL VARIABILITY ON THE QUANTIFICATION OF FLOOD HAZARD AND EXPOSURE: A CASE STUDY OF THE ITAJAÍ-AÇU RIVER BASIN, BRAZIL

CASSIANO BASTOS MOROZ

Enschede, The Netherlands, August, 2021

SUPERVISORS:
Prof. Dr. V. G. Jetten
Dr. D. Alkema

ADVISOR:

Dr. N. C. Kingma

THESIS ASSESSMENT BOARD:
Prof. Dr. C. J. van Westen (Chair)
Dr. R. van Beek (External Examiner, University Utrecht)

ABSTRACT

The risk to flash floods and riverine floods have been accentuated by rapid urbanization, population growth, and migration, especially in low- and middle-income countries. Additionally, climate change tends to intensify this risk by increasing the magnitude and frequency of hydrometeorological hazardous events. In this context, the quantification of the three components of the risk equation is essential to support better mitigation and adaptation strategies. These components are hazard, exposure, and vulnerability. This research aimed to investigate how the spatial rainfall variability impacts the quantification of flood hazard and exposure in a large catchment area. The Itajaí-Açu river basin, in southern Brazil, was selected as a case study area. First, the study conducted a validation of multiple gauge- and satellite-derived rainfall products to select the most suitable alternative for the analysis. The modified Kling-Gupta efficiency (KGE) was adopted as a statistical parameter to compare the rainfall products against reference rain gauge measurements. For this analysis, two satellite-derived rainfall products were selected: GSMaP and IMERG. As an attempt to improve the accuracy of the satellite estimates, this study also tested two merging techniques to combine satellite and gauge rainfall: mean bias correction (MBC) and residual inverse distance weighting (RIDW). In a later stage, the selected rainfall product was adopted to generate two rainfall scenarios of spatially distributed (SD) and spatially uniform (SU) design storms. The design storms were generated from intensity-duration-frequency (IDF) curves through the alternating block method. These rainfall scenarios were then adopted as input rainfall in the OpenLISEM hydrological model, which was previously calibrated with the 2013 historical flood event, presenting a Nash-Sutcliffe efficiency (NSE) of 0.97. The simulations were performed for the return periods of 2, 5, 10, and 25 years. The results of the rainfall validation indicated a strong potential of the merging techniques to decrease the bias and improve the accuracy of satellite rainfall estimates. In this sense, RIDW proved to be the most stable technique. Regarding the satellite products, GSMaP presented the best results for the region, with higher KGE values, and it was selected as a rainfall input in the methodology. In its turn, the analysis of the design storms indicated a high spatial rainfall variability in the region, as indicated by significant differences among the IDF curves in different locations of the basin. This variability was also demonstrated through the analysis of the total flooded area and the exposed urban area, classified by flood depth, in each one of the seven sub-catchments in the basin. Overall, changes in flood depth seemed to be more sensitive to the adopted rainfall scenario when compared with changes in flood extent, with variations of more than 400% depending on the sub-catchment and return period. In its turn, the variations in flood peak discharge and total water volume were up to 23.76% and 20.74%, respectively, at the outlets of the sub-catchments. While this research provided a large-scale analysis of the impacts of spatial rainfall variability on flood hazard and exposure in the Itajaí-Açu river basin, it is necessary to conduct more site-specific studies with high-resolution hydrological models and a stronger focus on a specific urban area. The Municipality of Blumenau is recommended as a possible case study area.

Keywords: Spatial rainfall variability, Satellite rainfall, GSMaP, IMERG, Hydrological modelling, OpenLISEM, Flood hazard, Flood exposure.

ACKNOWLEDGEMENTS

TABLE OF CONTENTS

LIST OF FIGURES

LIST OF TABLES

LIST OF ABBREVIATIONS

ANA	National Water Agency (Brazil)
CEPED UFSC	Center for Studies and Research in Civil Defense and Engineering at the Federal University of Santa Catarina
DTM	Digital Terrain Model
Embrapa	Brazilian Agriculture Research Corporation
IBGE	Brazilian Institute of Geography and Statistics
INPE	National Institute of Space Research (Brazil)
IPCC	Intergovernmental Panel on Climate Change
ITC	Faculty of Geo-Information Science and Earth Observation, University of Twente
JAXA	Japanese Aerospace Exploration Agency
MapBiomas	Brazilian Annual Land Use and Land Cover Mapping Project
NASA	National Aeronautic and Space Administration (U.S.A.)
SDS-SC	Secretariat for Sustainable Economic Development of the State of Santa Catarina
SIGSC	Geographic Information System of the State of Santa Catarina
UN	United Nations
WMO	World Meteorological Organization

1 INTRODUCTION

1.1 Background

Natural disasters have caused intense damage, with an increase in human and economic losses in the last decades (IPCC, 2012). From 2005 to 2015, more than 1.5 billion people were affected by disasters in the world, with more than 1.4 million injuries and 700 thousand deaths (UNDRR, 2015). This impact has been accentuated by rapid urbanization that, not exclusively, low- and middle-income countries are or will be soon facing, induced by population growth and migration (Thomson et al., 2020; Wolff, 2020). Alongside urbanization, climate change is likely to increase the frequency and intensity of extreme weather events, thus altering the dynamics of hydrometeorological hazards (IPCC, 2012). In this scenario, disaster risk mitigation and adaptation strategies have been receiving increased attention in the major international frameworks from the UN, including the Sustainable Development Goals (SDGs), the Sendai Framework for Disaster Risk Reduction, the New Urban Agenda, and the Paris Agreement.

In literature, disaster risk is often defined as a combination of hazard, exposure, and vulnerability (Klonner, Marx, Usón, de Albuquerque, & Höfle, 2016; Pitidis, Tapete, Coaffee, Kapetas, & de Albuquerque, 2018; van Westen, Damen, & Feringa, 2013), which are dynamic components in time and space (IPCC, 2012). Therefore, the identification, quantification, and prediction of these components are essential to support better planning practices focused on making cities and communities more resilient, as intended by SDG 11. While several studies have been working on the development of more robust physically-based, remote sensing-based, and data-driven methods for probabilistic hazard assessment, the uncertainties in model parameters and predictions remain a challenge (Refice, D'Addabbo, & Capolongo, 2018). In the scope of flood hazard, the representation of rainfall events is one of the most important driving forces in the simulation of hydrological processes (Sun et al., 2018). Wright, Mantilla, and Peters-Lidard (2017) highlighted the effects of rainfall patterns on hydrological processes, which can result in a diverse spectrum of flood hazard scenarios. On one hand, intense and localized rainfall events, often of short duration, can bring severe damage to urban areas that are exposed to flash floods and urban flooding. On the other hand, long duration distributed rainfall over entire catchments, even if of low intensity, can gradually saturate the soil layers, resulting in more surface runoff that contributes to riverine floods. Therefore, the correct representation of the intensity, duration, and space-time structure of rainfall events is essential in hydrological modelling.

While gauge stations can provide accurate rainfall measurements, they have limited capacity to represent the spatial patterns of rainfall, as the representativeness of the measurements decreases when moving away from the gauge locations (Jongjin, Jongmin, Dongryeol, & Minha, 2016; Marra, Morin, Peleg, Mei, & Anagnostou, 2017; Nerini et al., 2015; Woldemeskel, Sivakumar, & Sharma, 2013; Yang et al., 2017). This limitation is intensified in mountainous and tropical regions with complex weather systems, which present high spatial and temporal rainfall variability, often not captured by gauge interpolation methods (Beck et al., 2017; Manz et al., 2016). Some rain gauges can also present long periods of missing measurements (Dinku, Hailemariam, Maidment, Tarnavsky, & Connor, 2014), resulting in uncertainties in the analysis of annual maxima. To overcome these limitations, satellite products are often presented as an alternative to providing spatially continuous rainfall estimates at finer temporal resolutions. However, the indirect estimations derived from retrieval algorithms are subject to inaccuracies (Manz et al., 2016; Nerini et al., 2015; Woldemeskel et al., 2013).

1.2   Justification and research problem

Recent efforts have been made to conduct a large-scale evaluation of the performance of several satellite-derived rainfall products (Amorim, Viola, Junqueira, de Oliveira, & de Mello, 2020; Baez-Villanueva et al., 2018; Beck et al., 2017; Zambrano-Bigiarini, Nauditt, Birkel, Verbist, & Ribbe, 2017). In general, researchers conclude that the accuracy of these products has a strong influence on the physiographic characteristics of the study area, including climate and topography. The specific user needs or application should also be taken into account, as satellite products perform differently when representing different rainfall parameters such as maxima, totals, or the space-time structure of rainfall events (Beck et al., 2017). Therefore, while these studies provide important insights about the available satellite products and how the rainfall estimates are influenced by environmental factors, a catchment-specific validation is strongly recommended to select the most suitable dataset for specific purposes (Baez-Villanueva et al., 2018; Beck et al., 2017; Zambrano-Bigiarini et al., 2017).

In addition to satellite-derived products, merging techniques are also presented as promising solutions to combine the accuracy of gauge measurements with the spatial and temporal continuity of satellite data. It was observed that these techniques have the potential to decrease the bias of satellite-derived products in estimating rainfall intensities, which tend to be underestimated (Manz et al., 2016; Nerini et al., 2015; Woldemeskel et al., 2013). In this context, bias refers to all sources of errors associated with the indirect estimates from satellite sensors. This includes, for example, the positioning of the instruments or the incorrect interpretation of surface and atmosphere properties by the precipitation algorithms (Smith, Arkin, Bates, & Huffman, 2006). The benefits and performance of the merging techniques are highly dependent on the gauge network density and the level of spatial variability of the rainfall events in the region (Dinku et al., 2014; Jongjin et al., 2016; Manz et al., 2016; Woldemeskel et al., 2013). Nerini et al. (2015) and Manz et al. (2016) contributed to a better understanding of the characteristics of multiple merging techniques through a comparative study of nonparametric and geostatistical methods. The authors identified a strong dependence of the geostatistical methods on dense gauge networks. In contrast, nonparametric methods proved to be more robust in areas with a sparse gauge network, as they adopt the entire satellite-derived estimates in the adjustment process. Additionally, methods that perform spatially explicit interpolation (e.g. residual inverse distance weighting) instead of adopting spatially uniform correction factors (e.g. mean bias correction) proved to be more consistent, particularly in large spatial scales (Dinku et al., 2014; Manz et al., 2016). The challenge relies on whether a merging technique is required and, if required, which is the most suitable method.

In the scope of probabilistic risk assessment, researchers have been exploring the applicability of satellite and merged satellite-gauge rainfall for the generation of intensity-duration-frequency (IDF) curves (Marra et al., 2017; Noor, Ismail, Shahid, Asaduzzaman, & Dewan, 2021; Y. Sun, Wendi, Kim, & Liong, 2019). IDF curves are widely adopted in the assessment of hydrometeorological hazard processes (Marra et al., 2017; Peleg et al., 2018), as they allow the estimation of probable rainfall events, the so-called design storms (Wright et al., 2017). The generation of IDF curves is based on the statistical analysis of extreme rainfall values (Marra et al., 2017; Y. Sun et al., 2019), often extracted from long-term historical rain gauge measurements (Wright et al., 2017). In this process, disaggregation methods are a common alternative when observations are not available at sub-daily scales, but the uncertainties in the temporal distribution of rainfall remain a challenge (Wright et al., 2017). In addition, the representativeness of an IDF curve decreases moving away from the gauge location, thus their accuracy is highly dependent on the availability and density of the rain gauge network (Marra et al., 2017). Therefore, satellite products at fine temporal resolutions and continuous spatial coverage provide an opportunity to assimilate the spatial and temporal variability of

extreme rainfall events into the IDF curves (Noor et al., 2021). But the process is not so straightforward, and biases in satellite-derived rainfall estimates demand a critical analysis of the results.

In this context, with the increasing availability of remote sensing-derived data, the application of satellite rainfall provides a new opportunity in data-scarce regions: to better represent the spatial variability of extreme rainfall events. This is particularly relevant given the sensitivity of hydrological models to the spatial patterns of rainfall, as demonstrated in previous studies. Peleg, Blumensaat, Molnar, Fatichi, & Burlando (2017) evaluated the impacts of spatial rainfall variability in a small urban catchment through the simulation of spatially distributed rainfall events, stochastically generated from gauge and weather radar data. The results indicated a high relevance of the spatial variability of rainfall on the assessment of flood hazards, especially for larger return periods. Another similar study was conducted by Arnaud, Bouvier, Cisneros, & Dominguez (2002), who applied uniform and non-uniform rainfall inputs to simulate the hydrological response of four catchment areas from 20 to 1,500 km². Differences in peak discharges ranged from 10 to 80%, depending on the size of the catchment and the adopted return period.

So far, little is known about the spatial rainfall variability in data-scarce regions, which have few or no ground observations from rain gauges and weather radars. This research gap impairs the accurate assessment of flood hazard, as previously explained by the sensitivity of hydrological models to the scape-time structure of rainfall (Arnaud et al., 2002; Peleg et al., 2017). In addition, exposure remains an under-researched component of the risk equation. Most studies evaluated the influence of the rainfall variability on hydrological processes through the analysis of the simulated hydrographs, including peak discharge and water volume (Arnaud et al., 2002; Bárdossy & Das, 2008; Ochoa-Rodriguez et al., 2015; Peleg et al., 2017). However, it is essential to understand the influence of the rainfall variability on exposure, once risk only exists if there is an intersection between the hazard and the elements-at-risk (van Westen et al., 2013).

1.3   Research objective

Given the research gaps and opportunities presented in Chapter 1.2, the objective of this research is to evaluate to which extent the assumption of spatial rainfall variability impacts the quantification of flood hazard and exposure in a large catchment area. The Itajaí-Açu river basin, in southern Brazil, was selected as a case study area. To achieve this goal, a range of sub-objectives and research questions were identified, as presented below.

Sub-objective 1: To evaluate the accuracy of multiple rainfall products in representing the spatial variability and intensity of rainfall.

- How to merge gauge and satellite-derived rainfall data to provide more accurate and spatially continuous rainfall estimates?
- What is the potential of the satellite-gauge merging methods to improve the accuracy of satellite-derived rainfall products?
- Which rainfall product (among gauge, satellite and merged satellite-gauge) provides the most accurate rainfall estimates, focusing on the representation of spatial variability?

Sub-objective 2: To develop a framework accounting for the spatial rainfall variability in probabilistic flood hazard assessments.

- How to produce probable rainfall events (design storms) that represent the spatial rainfall variability over large catchment areas?
- To which extent the spatial rainfall variability influences the estimation of intensity-duration-frequency (IDF) curves and design storms?

Sub-objective 3: To set up a distributed hydrological model representing the conditions of a historical flood event.

- What was the spatial and temporal variability of rainfall during the historical flood event?
- How accurate are the model outputs compared to the observed discharge measurements and flood extent?

Sub-objective 4: To simulate scenarios of spatially uniform and spatially distributed probable rainfall events in the calibrated model.

- What is the contribution of each sub-catchment to the total water volume at the main outlet?
- Which factors influence flood exposure in the Itajaí-Açu river basin?
- How sensitive are flood hazard and exposure to a transition from spatially uniform to spatially distributed rainfall?

Chapter 2 introduces the case study area. Chapter 3 presents the research methodology, with a detailed description of each process adopted to address the research objectives and questions. In its turn, Chapter 4 presents the results associated with the processes described in the methodology. Chapter 5 critically discusses the research sub-objectives and the obtained results, with a further comparison with related research. Finally, Chapter 6 concludes the study through a summary of the main findings and provides recommendations for future research.

2   SETTING THE STAGE

2.1   Case study area

The Itajaí-Açu river basin is located in the State of Santa Catarina, in southern Brazil, with its limits between the latitudes 26°22'34"S to 27°52'34"S and the longitudes 48°38'17"W to 50°21'25"W. The basin has a total area of approximately 15,113 km² (INPE, 2008) and is home to more than 1.5 million inhabitants (Fleischmann, Collischonn, Paiva, & Tucci, 2019; Speckhann, Borges Chaffe, Fabris Goerl, Abreu, & Altamirano Flores, 2018). The catchment area is drained by the Itajaí-Açu river – the main river channel – and tributaries, a drainage system of around 1.55 km of watercourses per km² that flows into the Atlantic Ocean (Comitê do Itajaí, 2010). The catchment is constituted by seven main sub-catchment areas (Comitê do Itajaí, 2010). Upstream, the Itajaí-Açu river is originated in the confluence of the Itajaí do Oeste and Itajaí do Sul rivers. Moving downstream, the river receives the contribution from the Itajaí do Norte, Benedito, Luiz Alves, and Itajaí-Mirim rivers, in this order. An overview of the study area is presented in Figure 1.
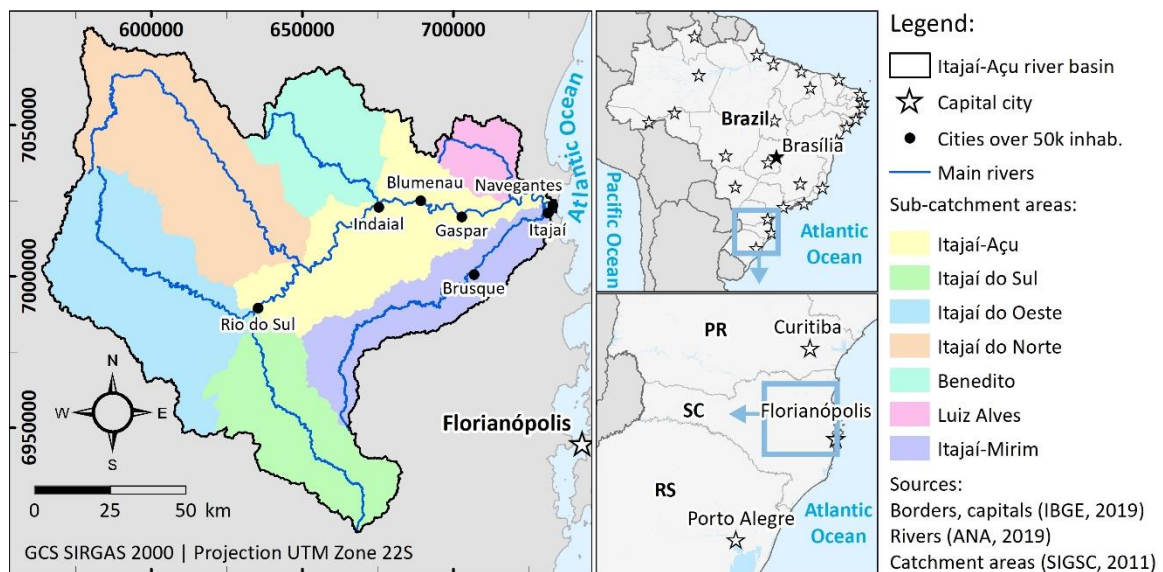
Figure 1: Location of the Itajaí-Açu river basin and sub-catchment areas.

The climate in the basin is classified as Köppen Cfa or humid subtropical, with hot and humid summers and cold to mild winters (Fleischmann et al., 2019). In summer, the hot and humid weather, with tropical air masses and the influence of the Atlantic Ocean, contributes to convective processes, with the occurrence of isolated rainstorms (dos Santos, Tornquist, & Marimon, 2014; Espíndola & Nodari, 2013). These events are sometimes intensified by cold fronts, resulting in heavy rainfall, electric discharges, gusting winds, and hail. In winter, intense cold fronts, often associated with extratropical cyclones, reach southern Brazil, bringing more rainfall to the region (Murara, Acquaotta, Garzena, & Fratianni, 2019). On average, the annual temperature in the basin is between 19 to 21°C (Comitê do Itajaí, 2010) and the annual precipitation is around 1,610 mm (Speckhann et al., 2018). The basin is monitored by 57 rain gauges under the responsibility of ANA, among manual and telemetric, apart from other gauges operated by private companies. While not necessarily classified as a data-scarce region, data gaps and inconsistencies in gauge measurements are a challenge, bringing uncertainties to the statistical analysis of extreme rainfall events.

Regarding the topography, the elevation ranges from 0 to 1,758 m, with the main river channel flowing in the west-east direction towards the Atlantic Ocean. The terrain is predominantly mountainous, with 29.50%

of its area with steep (15 to 30%) and 40.22% with either extremely (30 to 60%) or excessively steep (> 60%) slopes. Gentle (3 to 9%) or little to none (0 to 3%) slopes cover only 10.70% and 5.88% of the basin, respectively, while moderately slopes (9 to 15%) cover 13.70% of its area. Figure 2 illustrates the topography of the basin.
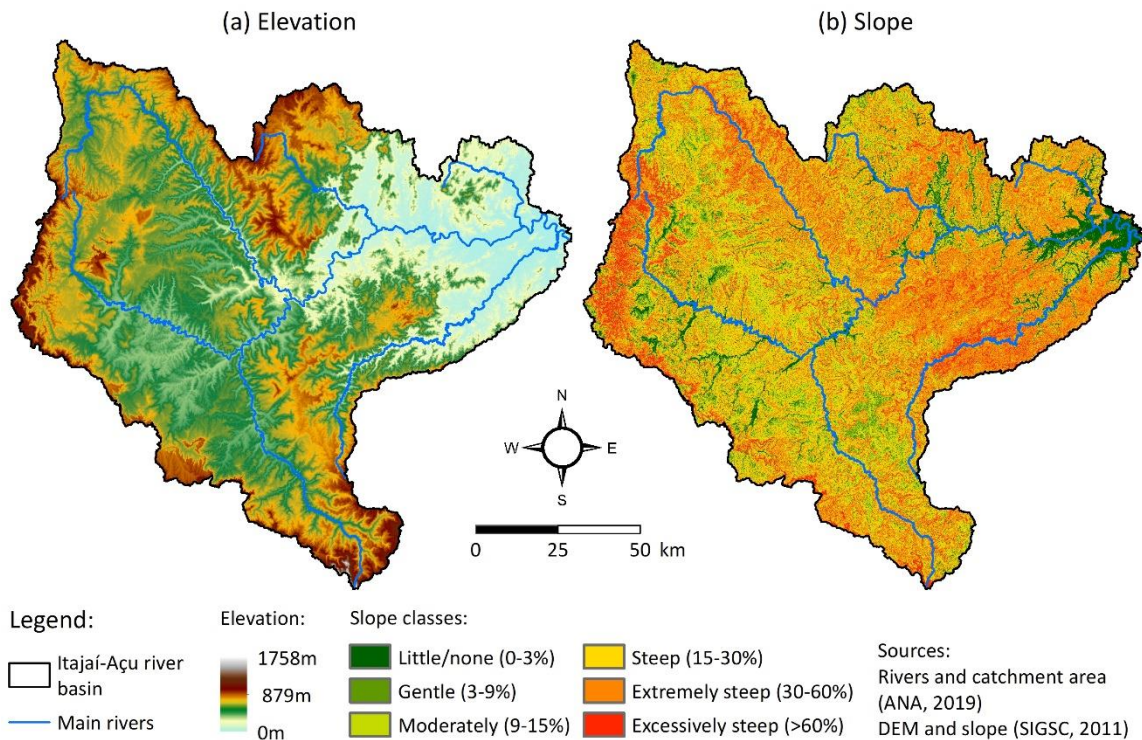
Figure 2: Elevation (a) and slope classes (b) in the Itajaí-Açu river basin.

The mountainous topography influenced the occupation process by concentrating the urban areas in the few flatter areas in the valley bottoms, which have been affected by floods since the first settlements dating back to the middle of the 19th century (de Paula, Nodari, & Espíndola, 2014; Mendonça de Moura, Vieira, & Bohn, 2015). In the following years, the urban expansion along the river banks exacerbated the flood exposure, intensifying the damages in the region (de Paula et al., 2014). In this context, although the basin represents less than 1% of the Brazilian population and 0.2% of its territorial area (IBGE, 2020), it encompassed 3 of the 10 cities with the highest number of people affected by natural disasters in Brazil from 1991 to 2012 (CEPED UFSC, 2013; Fleischmann, Collischonn, & Paiva, 2018; Fleischmann et al., 2019). In contrast, the basin is predominantly vegetated, with only 2.39% of its area covered by urban infrastructure. The predominant land-use classes are natural forest (rainforest), farming, and forest plantation, which covers, respectively, 56.11%, 31.26%, and 9.74% of the basin (MapBiomas, 2020). Figure 3 illustrates the land use classes in the basin and presents images of urban areas in different sections of the main river.
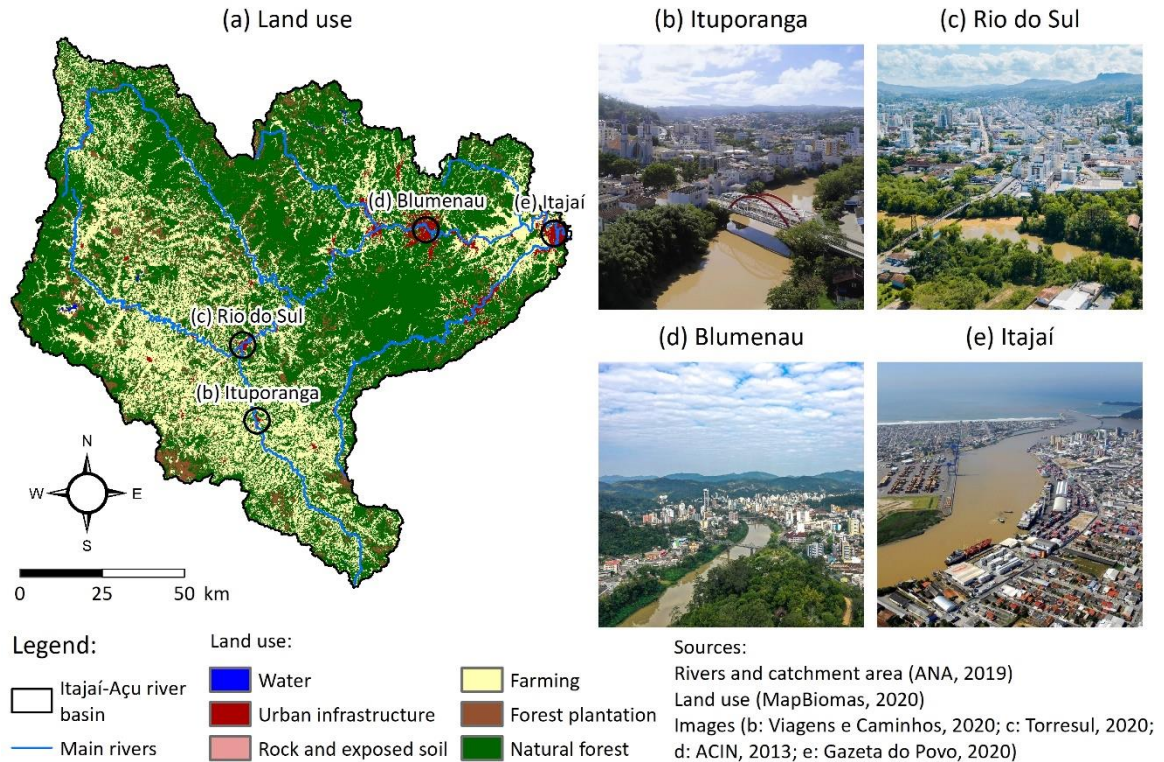
Figure 3: Land use classes in the Itajaí-Açu river basin (a) and images of the urban areas of Ituporanga (b), Rio do Sul (c), Blumenau (d), and Itajaí (e). The circular markers in the map (a) indicate the location of the images.

The Itajaí-Açu river basin has been constantly affected by floods. The highest water level of the last 100 years occurred in 1984, when the Itajaí-Açu river reached 15.34 m at the location of Blumenau (AlertaBlu, 2020), inundating around 70% of the urban area (de Paula et al., 2014). Another massive event occurred in 2008, classified as the worst disaster in the basin's history. Intense storms preceded by continuous rainfall during the previous months saturated the soil layers, resulting in several landslides, mudflows, flash floods, and riverine floods (Murara et al., 2019). It is estimated that 266 thousand people were affected, 23 thousand were displaced and 29 died only in the two most populous cities of the basin, Itajaí and Blumenau (CEPED UFSC, 2013). Three years later, in 2011, more than 302 thousand people were affected and 668 were displaced in Blumenau when the river reached 12.60 m (CEPED UFSC, 2013). Apart from these events, several floods have occurred in the basin since the beginning of the 21st century, as presented in Table 1. As a reference, the threshold for riverine floods at the location of Blumenau is a water level of 8 m.

Table 1: Historical flood events in the Itajaí-Açu river basin from 2000 to 2020. Source: AlertaBlu (2020).

Year	Date	Water level in Blumenau
2017	June 06th	8.52
2017	June 01st	8.71
2015	October 23rd	10.03
2014	June 29th	8.13
2014	June 09th	10.18
2013	September 23rd	10.51
2011	September 09th	12.60
2011	August 31st	8.50
2010	April 26th	8.46
2009	September 29th	8.06
2008	November 24th	11.52
2001	October 1st	11.02

3   RESEARCH METHODOLOGY

The flowchart of the research methodology is presented in Figure 4. Further explanation of the processes is presented in the following subchapters.
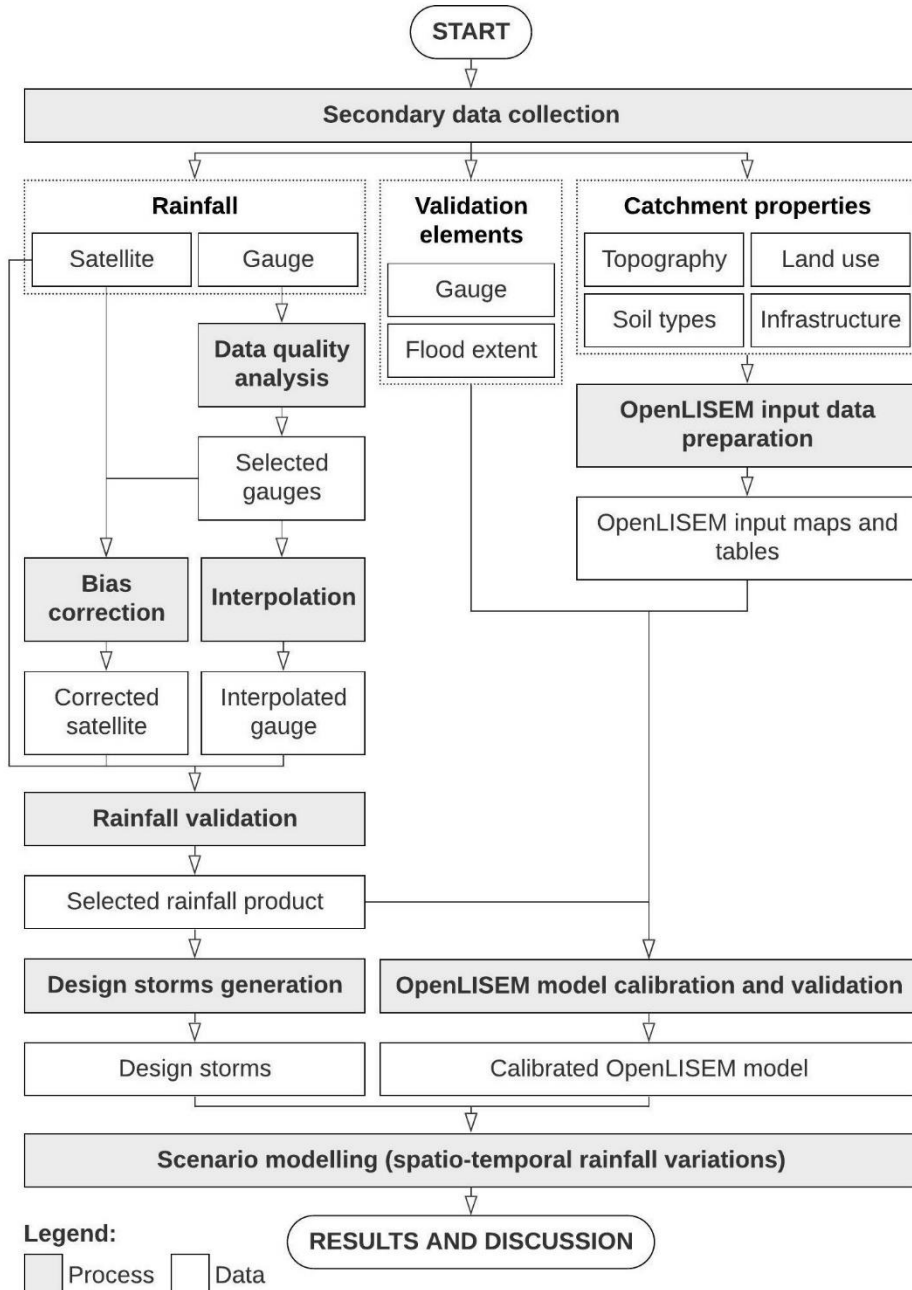
Figure 4: Flowchart of the research methodology.

As most of the processes were executed in Python and Google Earth Engine, a GitHub repository[1] was created to store all scripts developed in the research. The scripts were added to folders named with the number of the chapter they refer to. As an example, the script developed for Chapter 3.2 is located in the

[1] GitHub repository: github.com/cassianomoroz/ITC_masterthesis

folder named "chapter_3.2". Throughout the methodology chapter, references are presented to indicate the scripts associated with each process.

3.1 Collection of secondary data

The research methodology started with the collection of the required secondary data, including rainfall measurements, validation elements, and catchment properties. The rainfall data were retrieved from the HidroWeb Portal (ANA, n.d.), an integrated database of all gauges that constitute the Brazilian Hydrometeorological Network (RHN). Hourly measurements could not be adopted because of the short temporal coverage of the existing telemetric stations in the basin. Instead, daily measurements from 38 manual rain gauges were selected (see Appendix 1 for the complete list), which are collected every morning at 07:00 (GMT-3). The HidroWeb Portal (ANA, n.d.) was also adopted to obtain discharge measurements from the stream gauge Blumenau (PCD), essential for the calibration of the hydrological model. A single stream gauge was adopted because it is the only telemetric station in the downstream section of the Itajaí-Açu river. Adding to the discharge measurements, historical flood maps were provided upon request by the Municipality of Blumenau, which enabled the spatial validation of the simulated flood extent. Figure 5 presents the location of adopted gauges and the municipality where historical flood maps were available.
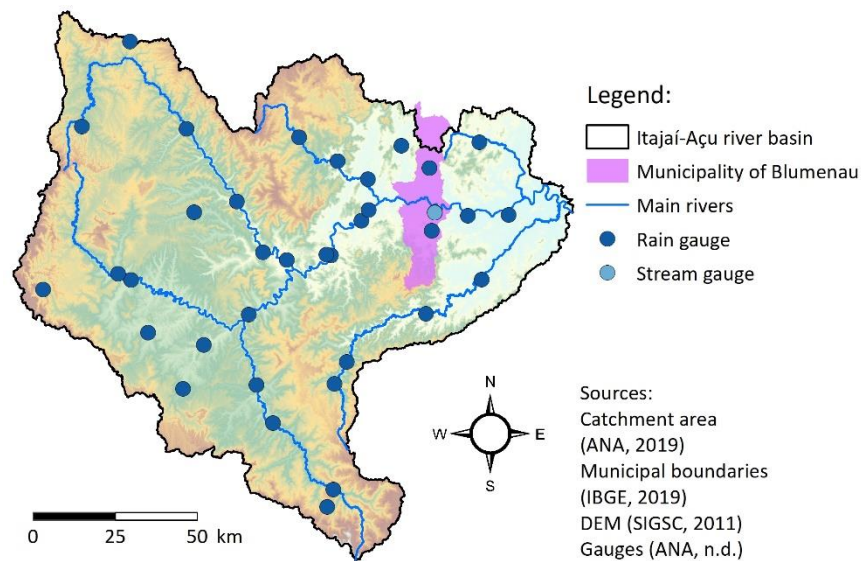
Figure 5: Available rain and stream gauges in the Itajaí-Açu river basin.

Alongside the gauge-based measurements, the satellite-derived rainfall products to be validated were selected based on the available products highlighted by Beck, Vergopolan, et al. (2017) and Sun et al. (2018). The wide set of products was filtered according to the following criteria: (1) the current continuity of the mission, (2) the product's availability in the Google Earth Engine database, (3) at least 0.1° of spatial resolution, (4) hourly temporal resolution, and (5) 20 years of temporal coverage. Based on these specifications, two products were selected: (1) the Integrated Multi-satellitE Retrievals for GPM (IMERG), and (2) the Global Satellite Mapping of Precipitation (GSMaP), both products of the Global Precipitation Measurement (GPM) mission, a joint mission between JAXA and NASA. IMERG provides half-hourly rainfall estimates at 0.1° of spatial resolution and temporal coverage from June 2000 to the present. In its turn, GSMaP provides hourly rainfall estimates at 0.1° of spatial resolution and temporal coverage from March 2000 to the present.

For the catchment properties, the data requirements were obtained from the documentation of the OpenLISEM model, the distributed hydrological model adopted in the research (Jetten & De Roo, 2018). The model inputs can be derived from sources of rainfall, topography, land use, soil type, and infrastructure.

To represent the topography, a 1-meter spatial resolution DTM was adopted, retrieved from SIGSC (SDS-SC, 2012). The high-resolution DTM was generated from airborne images through aerophotogrammetry and has a vertical accuracy of 0.39m (Fleischmann et al., 2019). Land-use information was obtained from MapBiomas (2020), a project that provides historical land-use maps for the entire Brazilian territory, recently expanded to other South American countries. The project relies on the Google Earth Engine platform to classify Landsat images, resulting in annual land-use maps at 30-meter spatial resolution from 1985 to 2019. In its turn, the platform SoilGrids (2020) was adopted to extract the soil profile properties. The platform applies machine learning techniques to provide global soil maps at a 250-meter spatial resolution based on soil profile observations and environmental covariates (de Sousa et al., 2020). To represent the existing infrastructure in the basin, two elements were considered: buildings and roads. The platform MapBiomas (2020) was also used for the buildings, represented as the land-use class urban infrastructure. Finally, the road system network was obtained from BC250 (IBGE, 2019), the Brazilian continuous cartographic base on a scale of 1:250,000.

3.2 Data quality control of rain gauges measurements
A data quality control procedure was conducted to select the time series of rain gauge measurements to be adopted in the hydrological studies. The method (see GitHub: chapter_3.2/script1) encompassed a range of data completeness and consistency tests, as described in the following subchapters. While there are multiple spatial analysis techniques to evaluate the consistency of rainfall data through principles of spatial correlation, single-station methods were preferred. Spatial correlation methods require a dense gauge network, especially in areas with complex terrain and very localized rainfall events – such as the Itajaí-Açu river basin – where they often present a high degree of spatial variability (WMO, 2008, 2018).

3.2.1 Consistency tests
Initially, the collected rain gauge measurements were converted to time series from 01-07-2000 to 01-07-2020, a period of 20 years that is also covered by the selected satellite-derived products, IMERG and GSMaP. Internal consistency tests were adopted to identify physically impossible values such as negative measurements (Michaelides, 2008; WMO, 2018). After, tolerance tests were conducted to highlight extreme rainfall events (WMO, 2018), set as measurements over 200 mm/day, which were checked against historical flood events made available by AlertaBlu (2020), the flood forecasting system of the Municipality of Blumenau. Gauges with negative measurements or daily rainfall over 200 mm that are not related to historical floods were eliminated. As a final step, the rainfall time series were visually checked through plotted histograms. Visual inspection is the basis of most quality control techniques, as it allows rapid and effective identification of anomalies such as long periods of constant measurements (Michaelides, 2008; WMO, 2008).

3.2.2 Completeness tests
Later, completeness tests were performed to verify data gaps in the time series of the pre-selected rain gauges, as suggested by Michaelides (2008). Data completeness is a critical factor in the analysis of rainfall time series, especially in extreme value statistics that involve the extraction of the annual maxima (WMO, 2018). To enable all processes of the inverse distance weighting (IDW) interpolation, bias correction, and validation of the rainfall products, two groups of rain gauges were created.

The first group (here referred to as Group 1) included the gauges with measurements over the entire period from July 2000 to July 2020 and a maximum of two consecutive days with missing values. This threshold was adopted considering the uncertainties of the adopted temporal interpolation methods, which assume that the conditions right before and after the data gaps are similar to the missing values (WMO, 2018).

Group 1 was adopted to perform the IDW interpolation of gauge measurements and the bias correction of satellite estimates, as both processes require complete time series. The days with missing values were filled with the temporal disaggregation of the rainfall measurement right after the gap. This method was select based on the assumption that, in manual gauge stations, missing records are often associated with accumulated rainfall totals, resulted from the absence of gauge readings in the previous days (WMO, 2008). Therefore, the succeeding rainfall measurement was divided by 2 or 3 in the case of one or two consecutive missing values, respectively. The resulting estimated value was then adopted to fill the missing values and to update the rainfall measurement after the gap.

The second group (here referred to as Group 2) included the gauges sharing at least one calendar year in common of complete time series, which was adopted to validate the rainfall products. Only the years in common were considered to guarantee an unbiased spatial validation of the rainfall products so that the validation parameters were always related to the same period regardless of which gauge was adopted as a reference. Also, the calendar year was adopted as a minimum period to enable the aggregation of the daily measurements into 3-daily and monthly totals. To find the balance between the number of gauges and common years with complete measurements, all combinations of gauges and years were tested. The optimal combination was selected through the inspection of the plotted maps, which were used to identify the most uniform spatial distribution of rain gauges sharing a representative period with complete data.

After finalizing the data quality control, daily measurements from each selected rain gauge were aggregated into 3-daily and monthly totals. This procedure generated a dictionary of daily, 3-daily, and monthly gauge measurements, which were adopted as a baseline in the following processes of the methodology. The results of the data quality control are presented in Chapter 4.1.

3.3   Interpolation of rain gauge measurements

In general, discrete observations of single or few rain gauges are not adequate to generate rainfall inputs, as they do not account for the spatial variations of rainfall (WMO, 2009). In this sense, hydrological studies usually rely on methods to estimate areal rainfall distribution from discrete data. In literature, the most common methods are Thiessen polygon (Pathiraja et al., 2018; B. B. Shrestha & Kawasaki, 2020; Su et al., 2020), inverse distance weighting (IDW) (Fensterseifer, Allasia, & Paz, 2016; J. Zhang, Fan, He, & Chen, 2019), and more complex geostatistical methods such as ordinary kriging (Manz et al., 2016; Nerini et al., 2015). While geostatistical methods are often being applied to interpolate rainfall data, it was observed that these techniques often do not perform significantly better than mathematical methods (WMO, 2018), especially when a dense gauge network is not available (Manz et al., 2016; Nerini et al., 2015). Therefore, the IDW interpolation was selected to estimate rainfall amounts over the basin.

IDW is a mathematical estimation method that combines observations from multiple neighboring gauges to estimate the rainfall amount in a specific location. The method is based on the assumption that closer gauges have a larger weight on the rainfall estimation at the target location (WMO, 2018). In this research, the IDW interpolation was performed on daily timesteps using as source locations the gauges from Group 1 (see Chapter 3.2). The method generated continuous rainfall data at the same spatial resolution and extent of the satellite images, resulting in a baseline for comparison with satellite-derived and merged satellite-gauge rainfall estimates. The interpolation was performed (see GitHub: chapter_3.3/script1) based on the equation provided by D. Shrestha (2020), as presented below:

$$V_0 = \frac{\sum_{i=1}^{n} \frac{V_i}{D_i}}{\sum_{i=1}^{n} \frac{1}{D_i}} \tag{1}$$

Where V_0 is the predicted value at point 0; V_i is the observed daily rainfall at gauge i; D_i is the distance between the gauge i and the point 0; and n is the number of rain gauges adopted in the interpolation.

As a final step, the interpolated data was adopted as a source to extract gauge-based daily rainfall estimates at the location of the gauges from Group 2 (see Chapter 3.2). These estimates were later aggregated into 3-daily and monthly totals to be validated against other rainfall products, as demonstrated in Chapter 3.5.

3.4　　Bias correction of satellite-derived rainfall estimates

This chapter aims to answer the following research questions:

Sub-objective 1: To evaluate the accuracy of multiple rainfall products in representing the spatial variability and intensity of rainfall.

- How to merge gauge and satellite-derived rainfall data to provide more accurate and spatially continuous rainfall estimates?

As a further step in the methodology, satellite and gauge rainfall data were combined through merging techniques, as an attempt to generate accurate and spatially continuous rainfall estimates. In this research, considering the sparse gauge network in the basin, two nonparametric methods were tested: mean bias correction (Nerini et al., 2015) and residual inverse distance weighting (Dinku et al., 2014). For both methods, a point-to-pixel approach was adopted to associate discrete and continuous data, thus assuming that the measurements at a rain gauge are comparable with the satellite-derived estimates at the pixel in which the gauge is located. Therefore, as an initial step, half-hourly (IMERG) and hourly (GSMaP) rainfall time series were extracted at the location of each rain gauge from Groups 1 and 2 (see GitHub: chapter_3.4/script1). These estimates were then aggregated into daily, 3-daily, and monthly totals (see GitHub: chapter_3.4/script2). In this step, the reporting times of the satellite-derived estimates (GMT) were advanced in 3 hours to match the time zone in the study area (GMT-3). Additionally, the time 07:00 was adopted as a transition time to the next day instead of 00:00 to account for the collection time of the measurements in the manual rain gauges. Finally, the resulting time series were adopted as input data to perform both merging methods (see GitHub: chapter_3.4/script3), as described in the following subchapters.

3.4.1　　Mean bias correction

The mean bias correction (MBC) was adopted to evaluate the performance of a spatially uniform method over a large catchment such as the Itajaí-Açu river basin. MBC corrects the satellite-derived rainfall estimates based on a multiplicative bias correction factor, which is averaged over the entire spatial domain. Therefore, the method assumes a uniform bias in space, thus not reflecting the spatial heterogeneity of rainfall. The validity of this assumption was evaluated through the spatial validation of the merged satellite-gauge product, as described in Chapter 3.5. The method was applied based on the descriptions presented by Nerini et al. (2015), where the correction factor is calculated at each timestep according to the equation:

$$B_T = \frac{\sum_{j=1}^{n} Z_G(x_j)}{\sum_{j=1}^{n} Z_S(x_j)} \tag{2}$$

Where B_T is the correction factor B at the timestep T; n is the number of available rain gauges from Group 1 (see Chapter 3.2); and $Z_G(x_j)$ and $Z_S(x_j)$ are the gauge measurements and the satellite-derived rainfall estimates at the gauge location j, respectively.

The method was applied for two different timestep intervals, 3-daily and monthly. Daily timesteps were not considered because of temporal mismatches that are common between the satellite-derived estimates and

gauge measurements. In this context, longer timesteps can minimize these residual mismatches between time boundaries (Beck et al., 2017). The list of correction factors over the entire 20-year period of rainfall data was then adopted to calculate the satellite-derived estimates at the location of the gauges from Group 2 (see Chapter 3.2). This was executed by multiplying the original half-hourly (IMERG) and hourly (GSMaP) rainfall estimates at timestep t by the correction factor B related to the same timestep. At the end, the corrected products were aggregated into daily, 3-daily, and monthly totals, to be adopted in the process of validation (see Chapter 3.5).

3.4.2   Residual inverse distance weighting

As a second method, the residual inverse distance weighting (RIDW) was adopted to evaluate the performance of a method reflecting the spatial heterogeneity of rainfall. The method was executed based on the methodology described by Dinku et al. (2014), later tested by Manz et al. (2016). Analogously to MBC, the 3-daily and monthly timestep intervals were adopted.

Initially, for each timestep over the 20 years of rainfall data, the difference between the gauge and satellite rainfall data was calculated at the location of each gauge from Group 1 (see Chapter 3.2). These differences were then interpolated through the IDW method (Chapter 3.3). In this step, the satellite images were used as a reference and the coordinates of their pixel centers were adopted as target locations. Because of the mismatch between the timestep intervals (3-daily, monthly) and the temporal resolution of the products (half-hourly, hourly), the interpolated differences were proportionally disaggregated at each pixel. This was done according to the percentage contribution of the satellite-rainfall estimates to the total rainfall at the timestep, as indicated in the following equation:

$$D_{d,t} = \frac{Z_{S,t}}{Z_{S,T}} * D_T \qquad (3)$$

Where $D_{d,t}$ is the disaggregated difference D_d at time t; $Z_{S,t}$ is the satellite-derived rainfall estimate Z_G at time t; $Z_{S,T}$ is the aggregated satellite-derived rainfall estimate Z_G at timestep T; and D_T is the total difference at timestep T.

The disaggregated differences were added back to satellite-derived rainfall estimates at the location of the rain gauges from Group 2 (see Chapter 3.2). Finally, the corrected products were aggregated into daily, 3-daily, and monthly totals to enable the validation process (see Chapter 3.5).

3.5   Validation of rainfall products

This chapter aims to answer the following research questions:

Sub-objective 1: To evaluate the accuracy of multiple rainfall products in representing the spatial variability and intensity of rainfall.

- – What is the potential of the satellite-gauge merging methods to improve the accuracy of satellite-derived rainfall products?
- – Which rainfall product (among gauge, satellite and merged satellite-gauge) provides the most accurate rainfall estimates, focusing on the representation of spatial variability?

A validation process was performed to select the best unbiased rainfall product by comparing their estimates with the reference measurements from the rain gauges from Group 2 (see Chapter 3.2). An overview of the evaluated products and their corresponding codes is presented in Table 2. Extensive literature research was conducted to identify the most suitable validation method. It was observed that a point-to-pixel approach is often applied to correlate satellite and/or reanalysis rainfall estimates with gauge measurements (Amorim et al., 2020; Baez-Villanueva et al., 2018; Beck et al., 2017; Zambrano-Bigiarini et al., 2017). In this case, the

rain gauges are adopted as a reference, thus assuming they are a representation of reality. Some of the most adopted statistical indices are modified Kling-Gupta efficiency (KGE) (Amorim et al., 2020; Baez-Villanueva et al., 2018), root mean square error (RMSE) (Amorim et al., 2020; Baez-Villanueva et al., 2018), and percent bias (PBIAS) (Amorim et al., 2020; Baez-Villanueva et al., 2018). Another common approach is the validation of the rainfall products through continuous hydrological modelling, with the comparison between the simulated and observed river discharges. Examples of this validation method can be found in the studies of Amorim et al. (2020) and Beck, Vergopolan, et al. (2017).

Table 2: Evaluated rainfall products.

Code	Source	Method
IDW	Gauge	IDW
GOr	GSMaP	Original product
GM3	Merged GSMaP-gauge	MBC timestep 3-daily
GMm	Merged GSMaP-gauge	MBC timestep monthly
GR3	Merged GSMaP-gauge	RIDW timestep 3-daily
GRm	Merged GSMaP-gauge	RIDW timestep monthly
IOr	IMERG	Original product
IM3	Merged IMERG-gauge	MBC timestep 3-daily
IMm	Merged IMERG-gauge	MBC timestep monthly
IR3	Merged IMERG-gauge	RIDW timestep 3-daily
IRm	Merged IMERG-gauge	RIDW timestep monthly

In this research, statistical indices were adopted for validation, given that continuous hydrological modelling of such a large catchment area would demand complex computing solutions to be run within an acceptable time. KGE was adopted as the main evaluation index, as it proved to be more suitable than RMSE and PBIAS because of its ability to represent both the temporal dynamics, volume, and distribution of rainfall (Baez-Villanueva et al., 2018; Zambrano-Bigiarini et al., 2017). The index is calculated through the combination of three components, to be named bias ratio, variability ratio, and linear correlation. By representing different components, KGE does not only provide an overall evaluation of the rainfall products but also helps to understand the sources of mismatches (Baez-Villanueva et al., 2018). The bias ratio (β) measures the tendency of the products to underestimate (β<1) or overestimate (β>1) the observed gauge measurements, presenting its optimal value at the unity. The variability ratio (γ) measures the dispersion of the rainfall products when compared with the observed gauge measurements, also presenting its optimal value at the unity. The linear correlation (r) measures the temporal rainfall dynamics, where the minimum value -1.0 represents a perfect negative correlation, the maximum value 1.0 represents a perfect positive correlation, and a value of 0 represents the absence of correlation. Finally, KGE represents the overall performance of the product and presents its optimal value at the unity (Baez-Villanueva et al., 2018).

The validation process (see GitHub: chapter_3.5/script1) started with the calculation of the three components of KGE. The indices were calculated independently for each gauge from Group 2 (see Chapter 3.2). Therefore, it was possible to assess how the rainfall products represent the spatial variability of rainfall, and if their estimations are consistent over the entire basin. The equations were obtained from Baez-Villanueva et al. (2018), as follows:

$$\beta = \frac{\mu_S}{\mu_O} \tag{4}$$

Where μ_S and μ_O are the arithmetic mean of observations and the corresponding mean of estimates, respectively.

$$\gamma = \frac{\frac{\sigma_S}{\mu_S}}{\frac{\sigma_O}{\mu_O}} \tag{5}$$

Where σ_S and σ_O are the standard deviation of observations and the corresponding standard deviation of estimates, respectively.

$$r = \frac{\sum_{i=1}^{n}(O_i - \bar{O})(S_i - \bar{S})}{\sqrt{\sum_{i=1}^{n}(O_i - \bar{O})}\sqrt{\sum_{i=1}^{n}(S_i - \bar{S})}} \tag{6}$$

Where n is the number of observations; O_i and S_i are the observed and the corresponding estimated rainfall values at day i, respectively; $\bar{O}$ and $\bar{S}$ are the arithmetic mean of observations and the corresponding mean of estimates, respectively.

As the last step, the KGE index was calculated through the combination of the three components, according to the following equation:

$$KGE = 1 - \sqrt{(\beta - 1)^2 + (\gamma - 1)^2 + (r - 1)^2} \tag{7}$$

The indices were calculated for each one of the 11 evaluated rainfall products (see Table 2) at daily, 3-daily, and monthly temporal scales. The adoption of 3-daily totals was recommended by Beck et al. (2016). The authors indicated that small temporal mismatches between the gauge and satellite rainfall estimates hinder the correlation of rainfall data on a daily scale. Therefore, both the daily and 3-daily scales were analyzed to investigate the sensitivity of the results. In its turn, monthly totals were also analyzed to provide a more complete evaluation for future studies and to build on previous research on the validation of satellite rainfall. However, the monthly scale was not adopted as a reference in the selection of the rainfall product, given that monthly rainfall totals are not relevant in extreme value statistics.

For 3-daily totals, the observed rainfall measurements were further classified based on their intensity. The selection of 3-daily rather than daily totals was based on the recommendations of Beck et al. (2016), as previously indicated. Instead of adopting fixed absolute thresholds, relative thresholds were calculated for the study region according to the rainfall percentiles at each one of the rain gauges from Group 2 (see Chapter 3.2). Rainfall intensities below the 50th percentile were not considered in this analysis as this research focuses on extreme weather events. Therefore, three intensity classes were defined: between the 50th and the 70th percentile, between the 70th and 90th percentiles, and above the 90th percentile. The adoption of relative thresholds for each gauge resulted in the same sample sizes for the statistical analysis. The KGE index and its components were recalculated for each class to investigate how the products' performance varies according to the rainfall intensity.

Chapters 4.2.1 and 4.2.2 present the results of the overall validation of the rainfall products and the validation per intensity class, respectively. In its turn, Chapter 4.2.3 indicates the rainfall product selected for the further processes of the methodology.

3.6   Definition of design storms

This chapter aims to answer the following research questions:

Sub-objective 2: To develop a framework accounting for the spatial rainfall variability in probabilistic flood hazard assessments.

– How to produce probable rainfall events (design storms) that represent the spatial rainfall variability over large catchment areas?

- To which extent the spatial rainfall variability influences the estimation of intensity-duration-frequency (IDF) curves and design storms?

After the validation process (see Chapter 3.5), the best fit among all rainfall products was adopted to generate design storms, which are hypothetical hyetographs associated with a specific return period (Krvavica & Rubinić, 2020). Design storms are often adopted in disaster risk research because of their ability to associate a hazardous event with a specific probability of occurrence, thus enabling the estimation of the expected annual loss (van Westen et al., 2013). Design storms have been traditionally generated as a spatially uniform event (Peleg et al., 2017), averaged over a specific catchment area. However, the response of the catchment to the spatial patterns of rainfall remains unexplored under the assumption of uniformity. In this research, this uncertainty was addressed through the generation of both spatially uniform and spatially distributed design storms. For the latter, a different design storm was created for each pixel of the rainfall product, resulting in a total of 195 design storms per return period. The design storms were generated from IDF curves, following the steps presented by CPRM (2020) for the development of the *Brazilian Rainfall Atlas*, as demonstrated in the following subchapters (see GitHub: chapter_3.6/script1). It is important to mention that these steps were performed independently for each one of the analyzed pixels. This was made possible through interactive programming solutions in Python and Google Earth Engine.

3.6.1 Extraction of the annual maxima series

The methodology started with the extraction of the series of annual maxima, described as the maximum rainfall registered during an annual time interval for a specific duration (CPRM, 2020). In this research, the time series encompassed 20 hydrological years from July 2000 to June 2020, which refers to the temporal coverage of the analyzed satellite products (GSMaP and IMERG). Hydrological years were adopted to ensure that the rainfall extremes would be identified even if they had occurred in the transition between calendar years, which happens during the wet season (Comitê do Itajaí, 2010). The annual maxima series was extracted for durations of 1, 2, 3, 4, 5, 6, 7, 8, 12, 14, 20, and 24 hours. Longer intervals were adopted after 8 hours because the rainfall intensity tends to stabilize over larger durations (CPRM, 2020).

3.6.2 Calculation of the empirical probability of the extreme rainfall events

Later, the empirical probability of the extreme rainfall events was extracted based on the series of annual maxima. The series was sorted in descending order, and the probabilities were calculated, for each duration, using the Weibull plotting position, as follows:

$$P\left(P > p\right) = \frac{m}{(N+1)} \tag{8}$$

Where $P\left(P > p\right)$ is the probability that the intensity of the event P is higher than the intensity p; m is the position in descending order; and N is the sample size.

3.6.3 Fitting of the annual maxima series to a Gumbel distribution

As a next step, a statistical distribution was fitted to the calculated series of empirical probabilities. The Extreme Value (EV) distribution type I, also known as the Gumbel distribution, was adopted to analyze the frequency of the extreme rainfall events for each duration and pixel. The Gumbel distribution was chosen because it is one of the most adopted and documented theoretical distributions for frequency analysis WMO (2009). Examples of studies that adopted the Gumbel distribution to investigate hazardous processes can be found in Martha, van Westen, Kerle, Jetten, & Vinod Kumar (2013), Pratomo, Jetten, & Alkema (2016), Quan Luna et al. (2014), and Speckhann et al. (2018). First, the Gumbel reduced variate was calculated for each probability according to the following equation:

$$y = -\ln\{-\ln[1 - P(P > p)]\} \qquad (9)$$

Where y is the Gumbel reduced variate; and P $(P > p)$ is the probability that the intensity of the event P is higher than the intensity p (Equation 8).

Finally, a linear function was fitted to the series of annual maxima by adopting the Gumbel reduced variate and the rainfall intensities as the independent and dependent variables, respectively. The coefficient of determination (R²) was calculated to evaluate the goodness of fit of the Gumbel distribution. The results of the fitting of the Gumbel distribution are presented in Chapter 4.3.1.

3.6.4 Calculation of the rainfall intensities for defined return periods

The fitted Gumbel distribution (represented as a linear function) was adopted to calculate the rainfall intensities for a specific probability of occurrence. In this research, design storms were generated for return periods of 2, 5, 10, and 25 years. Analogously to the previous step, the Gumbel reduced variate was initially calculated for the probabilities associated with each return period. In this case, the probability component in Equation 9 was updated according to the following equation:

$$y = -\ln\left[-\ln\left(1 - \frac{1}{T}\right)\right] \qquad (10)$$

Where y is the Gumbel reduced variate; and T is the return period in years.

These values were adopted as the independent variable in the linear function to calculate the rainfall intensity for each return period, duration, and pixel.

3.6.5 Generation of IDF curves

IDF curves were generated by associating the calculated rainfall intensities (y-axis) with their corresponding durations (x-axis) for a specific return period. Therefore, four curves were generated for each pixel of the rainfall product, referring to the return periods of 2, 5, 10, and 25 years. The combinations of intensity-duration were represented in a scatter plot and the consecutive points were connected through linear functions. These functions enabled the calculation of rainfall intensities for all durations between 1 and 24 hours. Chapter 4.3.2 illustrates the generated IDF curves, highlighting the distribution – mean, standard deviation, maximum and minimum – among the pixels over the study area.

3.6.6 Generation of design storms

Finally, the design storms were generated through the alternating block method, which is one of the methods adopted to develop design hyetographs from IDF curves. More information about the method can be found in Chow, Maidment, & Mays (1988). The design storms were generated for 24 hours, divided into hourly time intervals. A 24-hour duration was adopted because of the high time concentration of the catchment. The time of concentration refers to the time that the water takes to move from the hydraulically most distant part of the catchment to its outlet (Dingman, 2015b). Therefore, by adopting a rainfall input with a duration exceeding the time of concentration, it is possible to simulate the equilibrium runoff, which is achieved when all parts of the catchment start contributing to the discharge at the outlet (Dingman, 2015b).

In total, two design storms were created for each return period: a spatially distributed and a spatially uniform. For the first, the spatially distributed IDF curves were adopted to generate maps for each time interval of the 24-hour design hyetograph. This resulted in design storms constituted of several rainfall maps with varying intensities in space. For the latter, a single IDF curve was generated for the entire catchment area by calculating the mean value among all pixels. This curve was adopted to develop an averaged uniform design storm for the study area. Chapter 4.3.3 presents the generated design storms.

3.7   Preparation of OpenLISEM hydrological model

This chapter aims to answer the following research questions:

Sub-objective 3: To set up a distributed hydrological model representing the conditions of a historical flood event.

- − What was the spatial and temporal variability of rainfall during the historical flood event?
- − How accurate are the model outputs compared to the observed discharge measurements and flood extent?

Flood hazard scenarios were simulated with OpenLISEM, an open-source physically-based model that represents the land surface processes of runoff, flooding, and erosion (Jetten & De Roo, 2018). OpenLISEM was selected because of its ability to handle catchment areas of any size and the consolidated literature demonstrating its applicability to model riverine floods and flash floods (Bout & Jetten, 2018; Pérez-Molina, Sliuzas, Flacke, & Jetten, 2017; Umer, Jetten, & Ettema, 2019). In addition, the distributed nature of the model explicitly considers the spatial variability of the input data, thus allowing the definition of spatially distributed design storms. The model was run with a 1D-2D schematization: 1D kinematic overland flow combined with a 2D dynamic flood from channels. The model was settled to account for the processes of interception and infiltration and to include channels and infrastructure. Erosion processes were not included because of the research focus on flood events.

3.7.1   Input data

Initially, the required input data was prepared according to the instructions presented in the documentation of the model (Jetten & De Roo, 2018). In general, all input data can be derived from sources of rainfall, topography, land use, and soil types. An overview of the data requirements and data sources is presented in Table 3. Information about the data collection procedure is demonstrated in Chapter 3.1. The data preparation was performed in ArcGIS and PCRaster through an adaptation of the script made available by Jetten (2015) (see GitHub: chapter_3.7/script1). The following subchapters explain the assumptions and processes adopted to generate the input maps and tables.

Table 3: OpenLISEM data requirements and adopted secondary sources.

Category	Input data	Source
Rainfall	Design storms	GSMaP, IMERG, rain gauges
Topography	DTM	SDS-SC (2012)
	Gradient	Derived from DTM
	Local drainage direction (LDD)	Derived from DTM
	Channel mask	Derived from DTM
	Channel width	Fleischmann et al. (2019)
	Channel depth	Fleischmann et al. (2019)
Land use	Land use classes	MapBiomas (2020)
	Building cover	Derived from land use classes
	Vegetation cover	Derived from land use classes
	Manning's (N)	Jetten & De Roo (2018)
	Surface roughness (RR)	Jetten & De Roo (2018)
	Normalized difference vegetation index (NDVI)	Landsat 5 and 8 collections
	Leaf area index (LAI)	Derived from NDVI
	Canopy storage	Derived from LAI
Soil types	Saturated conductivity (Ksat)	Derived from SoilGrids (2020)
	Average suction at the wetting front (psi)	Derived from SoilGrids (2020)
	Porosity (Thetas)	Derived from SoilGrids (2020)
	Initial moisture content (Thetai)	Derived from SoilGrids (2020)
	Depth	Derived from DTM

Rainfall

As previously mentioned, two design storms (see Chapter 3.6) were tested to evaluate the sensitivity of the hydrological model to the spatial rainfall variability. First, the spatially distributed design storm was prepared as a combination of 24 rainfall maps – referring to the duration of the hyetograph – and a text file associating the maps with their corresponding times. In its turn, the spatially uniform design storm was prepared as a single text file associating the average rainfall intensity with its corresponding time.

Topography

The Digital Terrain Model (DTM) is a primary input in hydrological models such as OpenLISEM, as topography plays an important role in the pathways of the surface runoff movement (Wu, Li, & Huang, 2008). In this research, the original 1-meter DTM (SDS-SC, 2012) was resampled to a spatial resolution of 100 meters. Although the literature indicates that the spatial resolution of the DTM significantly affects the representation of topographic attributes (Tan et al., 2015; Tay, Sagar, & Chuah, 2005; Wu et al., 2008), finer spatial resolutions could not be adopted because of the large dimensions of the catchment area. However, three resampling techniques were evaluated in terms of their ability to represent the topographic attributes: (1) nearest neighbor, (2) bilinear interpolation, and (3) cubic convolution. Because a detailed analysis of the DTM accuracy is not among the objectives of this research, a simplistic evaluation was conducted based on the analysis of geometrical parameters. Studies that performed a similar evaluation were conducted by Tan et al. (2015) and S. Wu et al. (2008). First, the DTM-derived features of the total catchment area and main river length were compared against reference features provided by ANA (2019). Then, the same reference features were adopted to visually inspect the original channel network against the DTM-derived layer. A final selection of the resampling technique was done through the identification of the lowest errors between the reference and the DTM-derived features, supported by the visual inspection of the river network. The results of the evaluation are presented in Chapter 35.

The resampled DTM was then adopted to derive the required input maps of gradient and local drainage direction (LDD). In addition, the flow accumulation was calculated to define the channel network in the catchment, thus generating the channel mask. The origin of the channels was defined considering a minimum upstream drainage area of 1 km². This value was selected to match the DTM-derived network with the reference channel network provided by ANA (2019). Later, the mask of the catchment area was generated by inserting the outlet in the confluence of the Itajaí-Açu river with the Atlantic Ocean. The catchment and channel masks were then applied to clip the gradient and LDD maps. Finally, the dimensions of the channel cross sections were obtained from Fleischmann et al. (2019). The authors adopted locally available data to adjust hydraulic geometric relationships for rectangular cross sections, resulting in the following equations:

$$W = 0.95 * A_d^{0.5} \tag{11}$$

$$H = 0.3 * A_d^{0.3} \tag{12}$$

Where W is the channel (rectangle) width in meters; H is the channel (rectangle) height in meters; and A_d is the drainage area in square kilometers.

In this case, the width and height parameters were calculated from the previously generated flow accumulation map, representing the cumulative drainage area along the channels. Because of the spatial resolution of the model, the channel width was limited to a maximum of 100 meters.

Land use

The land use maps were extracted from the platform MapBiomas (2020) for the years 2013 – to calibrate the model – and 2019 – to simulate the rainfall scenarios based on the most recent map. First, the maps

were reclassified to match the classification adopted by Jetten & De Roo (2018). The new land use classes were adopted to generate input maps of surface roughness (RR) and Manning's surface roughness coefficient (n), according to the values presented by Jetten & De Roo (2018). Later, the class *urban settlement* was adopted to estimate the percentage of building cover in each 100-meter pixel through the *Zonal Statistics* function in ArcGIS. Analogously, the classes *natural tropical forest* and *plantation forest* were adopted to estimate the percentage of vegetation cover. An overview of the reclassification attributions and the adopted coefficients is presented in Table 4. In the case of the channel, the Manning's coefficient was first defined as 0.03, as adopted in previous studies in the catchment (Fleischmann et al., 2018, 2019).

Table 4: Reclassification of land use classes and attributed surface roughness coefficients.

MapBiomas (2020)	Jetten & De Roo (2018)	RR	n
Forest formation	Natural tropical forest	1.00	0.10
Forest plantation	Plantation forest	1.00	0.05
Pasture	Mixed farming	1.00	0.10
Mosaic of agriculture and pasture	Mixed farming	1.00	0.10
Agriculture soy beans	Intensive farming	1.00	0.05
Agriculture other temporary crops	Intensive farming	1.00	0.05
Urban infrastructure	Urban settlement	0.50	0.02
Mining	Rock and exposed soil	0.50	0.02
Other non-vegetated areas	Rock and exposed soil	0.50	0.02
Water	Water	0.10	0.03

The canopy storage was estimated based on the normalized difference vegetation index (NDVI). First, the index was calculated from the red and near-infrared bands of the Landsat 5 – for the year 2013 – and Landsat 8 collections – for the year 2019. The NDVI was adopted to estimate the leaf area index (LAI) according to the equation presented in the PCRaster script developed by Jetten (2015). Finally, the LAI was adopted to calculate the canopy storage according to the equations applied in the OpenLISEM model. Because of the diverse vegetation cover in the catchment, three different canopy storage equations were considered: (1) *broadleaved forest* to represent the land use class *natural tropical forest*; (2) *eucalypt* to represent the land use class *plantation forest* (CanalRural, 2020); (3) *crops* to represent the land use classes *mixed farming* and *intensive farming*.

As a final step, the road infrastructure was obtained from BC250 (IBGE, 2019), the Brazilian continuous cartographic base on a scale of 1:250,000. In all cases, a road width of 12 meters was adopted because the majority of intermunicipal roads are one-lane in the region.

Soil types

To represent the soil types, the platform SoilGrids (2020) was adopted to extract the soil properties of organic carbon, bulk density, and contents of clay, sand, and silt. In total, two soil layers were applied to represent the soil types in the catchment. The depths of the soil layers were estimated as a function of the DTM. In this sense, it was assumed that shallow soils are often located in erosion-prone areas in medium to steep slopes, while deep soils are concentrated in accumulation zones in the valley bottoms. The equations to estimate the depth were obtained from the PCRaster script provided by Jetten & Shrestha (2020) (see GitHub: chapter_3.7/script2). In SoilGrids, the depths from 5 to 15 cm and 60 to 100 cm were selected as representative of the first and second layers, respectively. These values were a recommendation of Jetten & Shrestha (2020). Because SoilGrids do not contain data in urban areas, the *Nibble* function in ArcGIS was applied to fill these gaps with the information from the nearest neighbor with data. In addition, the vegetation cover was adopted to incorporate the effects of compaction on the soil properties. In this case, it was assumed that soils with vegetation cover present lower compaction levels. These effects were incorporated in the calculation of the density factor, which ranged from 1.0 to 0.9 for pixels with 0% to 100% of vegetation cover, respectively.

In a later stage, pedotransfer functions were adopted to translate the obtained soil and vegetation data into the required soil-hydraulic parameters of saturated hydraulic conductivity, average suction at the wetting front, porosity, and initial moisture content. Pedotransfer functions are predictive equations that estimate soil physical properties based on regression-type analyses of soil survey data (Dingman, 2015a). The initial soil moisture content was initially adopted as 50%, where 0% represents the field capacity and 100% represents saturated soil (based on porosity). In the case of the channels, the saturated hydraulic conductivity was assumed as 0. The pedotransfer functions were applied through an adaptation of the PCRaster script provided by Jetten & Shrestha (2020) (see GitHub: chapter_3.7/script2).

3.7.2   Calibration and validation

After the input data preparation, the OpenLISEM hydrological model was calibrated with the 2013 flood. This event was adopted because of the availability of almost complete discharge measurements at 15-minute intervals, which was not present in the major events of 2008 and 2011. During the event, the flood peak occurred on the 23rd of September, with an observed discharge of 4,369 m³/s in the location of the gauge Blumenau (PCD) (see Figure 5).

The calibration procedure started with the selection of the rainfall event to be simulated. This was done through the analysis of the average rainfall over the catchment in September 2013. It was assumed that the limit between two consecutive rainfall events can be defined as the period without rainfall. In this sense, the start time of the simulation was defined as the 21st of September 2013, at 16:00 (GMT-3), which refers to the moment right before the beginning of the most intense rainfall event. The simulation was run until the time when the observed discharge reaches the same intensity as at the beginning, which was identified as the 25th of September 2013 at 03:00 (GMT-3). Therefore, the simulation was performed for a total period of 5,000 minutes with timesteps of 60 seconds. Finally, to account for the previous discharge conditions in the catchment, the baseflow was assumed as the observed discharge at the start time, or 2,300 m³/s at the outlet.

After simulating the initially adopted parameters, the model was calibrated by adjusting the Manning's coefficient and the initial soil moisture content, as often applied in literature (Ghanbarpour, Salimi, & Hipel, 2013; Hessel, Jetten, & Baoyuan, 2003; Hsieh, Hsu, & Li, 2006; Jetten & Maneta, 2011; Lee, Heo, Lee, & Kim, 2017; Umer et al., 2019). The initial parameters (see Chapter 3.7.1) were first modified in intervals of 0.005 – for the Manning's coefficient – and 5% – for the initial soil moisture content. After finding the best combination of both parameters, shorter intervals were adopted to refine the calibration. To avoid equifinality, the calibration was conducted through the visual inspection of the shape of the hydrograph, supported by the calculation of three statistical indices: Nash-Sutcliffe Efficiency (NSE), total runoff volume error, flood peak discharge error. NSE was calculated according to the equation presented by Gupta, Kling, Yilmaz, & Martinez (2009), as follows:

$$NSE = 1 - \frac{\sum_{t=1}^{n}(x_{s,t} - x_{o,t})^2}{\sum_{t=1}^{n}(x_{o,t} - \mu_o)^2} \tag{13}$$

Where n is the total number of timesteps; $x_{s,t}$ is the simulated discharge values at timestep t; $x_{o,t}$ is the observed discharge values at timestep t; and μ_o is the mean of the observed discharge values.

To perform the spatial validation of the hydrological model, the simulated flood extent was compared against the historical flood maps provided by the Municipality of Blumenau. The validation was conducted through the visual inspection of the simulated and observed flood extents and the calculation of the Cohen's Kappa coefficient, as presented by Cohen (1960). Chapters 4.4.2 and 38 present the results of the calibration of the hydrological model and the validation of the flood extent, respectively.

3.8   Simulation of rainfall scenarios

This chapter aims to answer the following research questions:

Sub-objective 4: To simulate scenarios of spatially uniform and spatially distributed probable rainfall events in the calibrated model.

- − What is the contribution of each sub-catchment to the total water volume at the main outlet?
- − Which factors influence flood exposure in the Itajaí-Açu river basin?
- − How sensitive are flood hazard and exposure to a transition from spatially uniform to spatially distributed rainfall?

The calibrated OpenLISEM model (see Chapter 3.7.2) was adopted to simulate the scenarios of spatially distributed and unform design storms (see Chapter 3.6) for each return period. A description of the adopted scenarios is presented in Table 5. The input maps of NDVI, land use classes, and derived information (see Chapter 3.7.1) were updated to account for changing catchment characteristics from 2013 to 2019 – the most recent available maps. In addition, to consider the predominant conditions in the basin, the discharge that is exceeded 90% of the time (Q90) was adopted as a baseflow in the simulations. The Q90 was extracted from Comitê do Itajaí (2010), and refers to a discharge of 217 m³/s at the outlet of the Itajaí-Açu river.

Table 5: Simulated rainfall scenarios.

Code	Design storm	Return period
SD2	Spatially distributed rainfall	2 years
SU2	Spatially uniform rainfall	2 years
SD5	Spatially distributed rainfall	5 years
SU5	Spatially uniform rainfall	5 years
SD10	Spatially distributed rainfall	10 years
SU10	Spatially uniform rainfall	10 years
SD25	Spatially distributed rainfall	25 years
SU25	Spatially uniform rainfall	25 years

The sensitivity of the flood hazard quantification to the spatial rainfall variability was evaluated in terms of the calculated differences in the total runoff volume, flood peak discharge, and flood extent. For volume and discharge, seven sections were analyzed, including the outlets of the sub-catchments, and the main outlet of the Itajaí-Açu river basin. In the case of the flood extent, the analyzed locations were the boundaries of each sub-catchment. Figure 1 illustrates the location of the sub-catchments and their outlets. In addition, the simulated flood depth maps were intersected with the land use class *urban settlement* to provide a simple assessment of flood exposure. The impacts of the spatial rainfall variability on the quantification of flood exposure were evaluated individually for each sub-catchment, as previously described. Chapters 4.5.1 and 4.5.2 present the results of the quantification of flood hazard and exposure, respectively.

4   RESULTS

4.1   Data quality control of rain gauges measurements

The data quality control of the 38 analyzed rain gauges resulted in the selection of the gauges from Groups 1 and 2, as previously explained in the methodology (see Chapter 3.2). When performing the consistency tests, it was observed that no rain gauge presented negative measurements. However, three gauges (2649007, 2649008, and 2649065) presented unusual extreme measurements over 200 mm/day. To further evaluate these possible inconsistencies, the dates associated with the extreme rainfall were checked against the flood records from the Municipality of Blumenau. The gauge 2649007 was maintained in the database because the extreme rainfall happened on the 23rd and 24th of November 2008, which is coincident with one of the largest flood events in the region. On the other hand, the other two gauges were eliminated because the measurements were not associated with any historical flood event, except at the gauge 2649065 on the 22nd of November 2008. An overview of the extreme measurements and their corresponding dates is presented in Table 6.

Table 6: Rain gauges with unusual extreme measurements, corresponding dates and intensities, and association with historical flood events.

Gauge code	Date	Rainfall (mm/day)	Associated flood event
2649007	23-11-2008	243.5	Yes
2649007	24-11-2008	250.9	Yes
2649008	21-01-2010	330.6	No
2649065	06-08-2008	240.3	No
2649065	10-11-2008	415.0	No
2649065	17-11-2008	310.0	No
2649065	22-11-2008	513.0	Yes
2649065	30-11-2008	377.0	No

It is important to highlight that most of the extreme measurements at the gauge 2649065 were also registered in November 2008. Although there is evidence of high rainfall amounts over the region during this period (CEPED UFSC, 2013), the rainfall intensities are much higher than the measurements at the surrounding gauges. In this sense, it is very unlikely that extremes over 300 mm/day were concentrated over a specific location of the basin multiple times during the same month. Therefore, the gauge 2649065 was eliminated together with the gauge 2649008. Finally, the histograms of the remaining gauges were visually inspected. No gauge was eliminated in this step, given that no inconsistencies could be visually identified.

Later, the remaining 35 rain gauges were evaluated for completeness. It was observed that only 4 gauges presented the characteristics to be adopted in Group 1. This includes a temporal coverage of 20 years (July 2000 – July 2020) with a maximum of two consecutive days with missing measurements. On the other hand, all the remaining gauges presented at least one calendar year with complete rainfall data. To select a representative sample of rain gauges for Group 2, the 31 rain gauges were adopted to investigate all possible combinations of gauges and years in common with measurements. An overview of the balance between the number of gauges and years is presented in Figure 6. A maximum number of 29 gauges can be achieved by selecting only one year in common. This value significantly decreases with the increase in the number of years, reaching a minimum of 1 gauge for 16, 17, and 18 years of complete data.
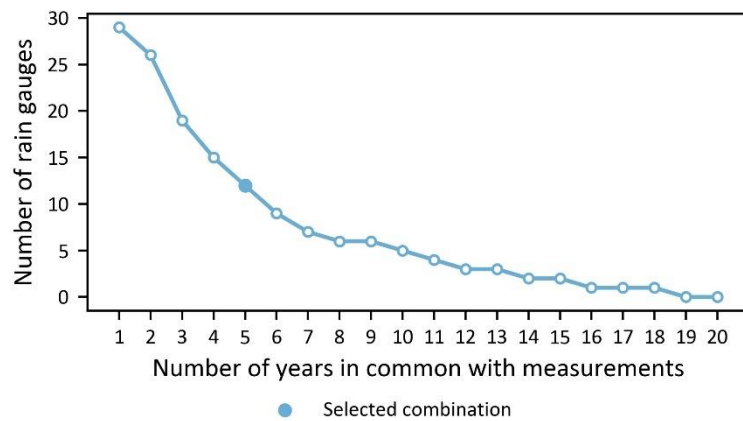
Figure 6: Combinations of the number of rain gauges and the number of common years with complete measurements.

By analyzing the spatial distribution and temporal coverage of all possible combinations, a total of 12 rain gauges were adopted in Group 2, resulting in 5 years of data (2000, 2001, 2002, 2018, and 2019). This combination was selected to find a balance between the number of gauges, their distribution in space (ideally even), and the number of years. Figure 7 illustrates the location of the gauges adopted in Groups 1 and 2 and the gauges that were eliminated from the analysis. A complete description of all rain gauges with observations about the data quality control is presented in Appendix 1.
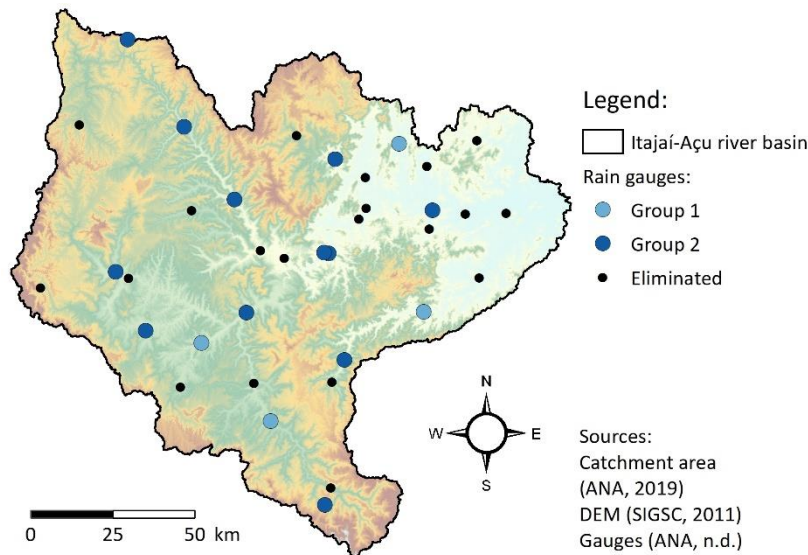
Figure 7: Adopted and eliminated rain gauges, with a distinction between Groups 1 and 2.

4.2 Validation of rainfall products

4.2.1 Overall validation

The validation was performed after generating all the analyzed rainfall products (see Table 2) through the IDW interpolation of gauge measurements (see Chapter 3.3) and the bias correction of satellite estimates (see Chapter 3.4). The modified Kling-Gupta Efficiency (KGE) and the components of bias ratio (β), variability ratio (γ), and linear correlation (r) were calculated as indicated in Chapter 3.5. In an initial step, these indices were calculated for the entire time series, regardless of the rainfall intensity. Figure 8 presents the performance (y-axis) of the rainfall products for daily, 3-daily, and monthly aggregates (x-axis). Each boxplot represents the distribution of the statistical parameters among the rain gauges adopted for validation

(Group 2). The optimal values of the statistical indices are highlighted as a dashed black line. Outliers were removed from the graph for better visualization.
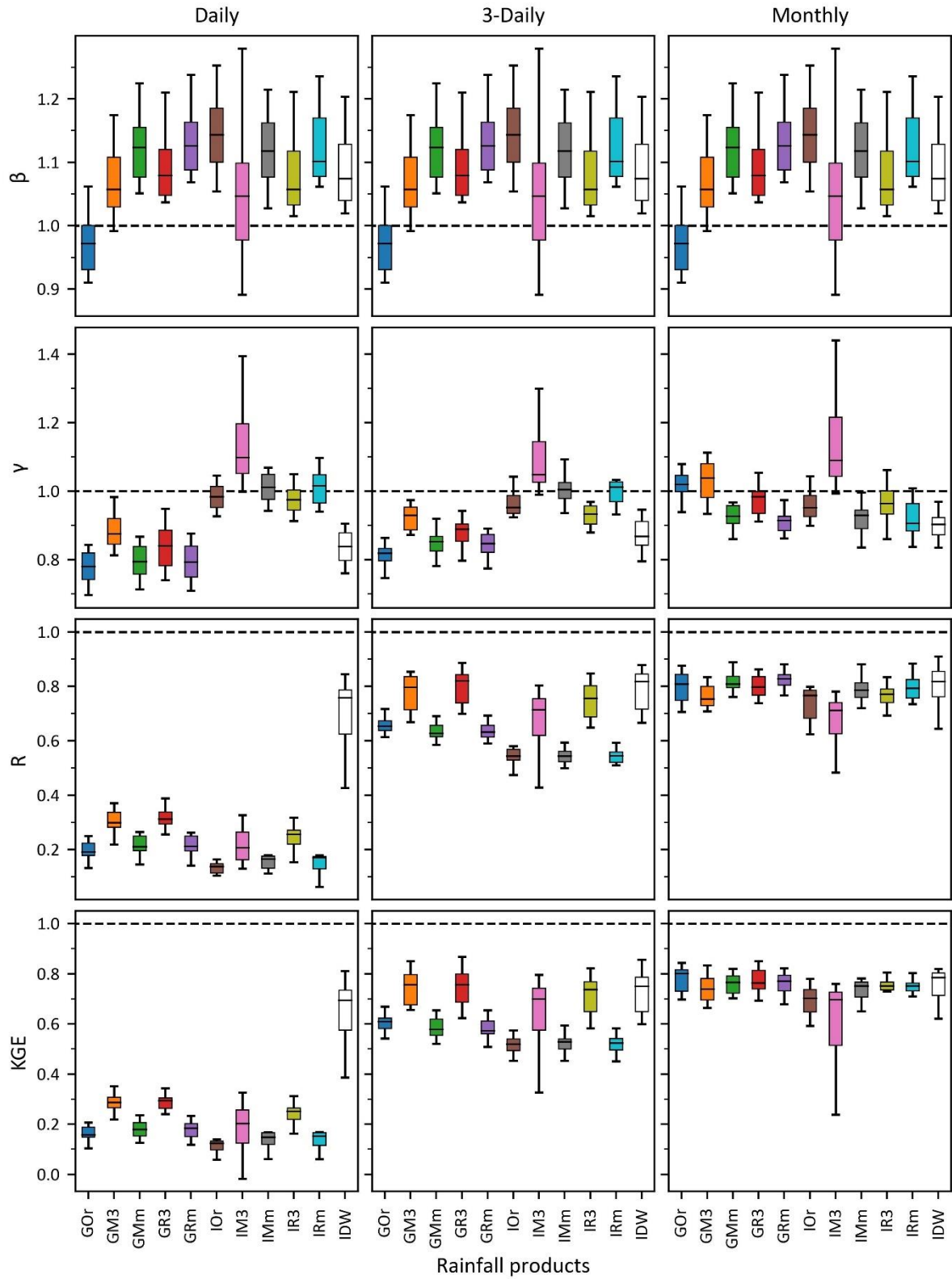
Figure 8: Overall validation of the rainfall products. Statistics of bias ratio (β), variability ratio (γ), linear correlation (r) and modified Kling-Gupta Efficiency (KGE) per product for daily, 3-daily, and monthly totals.

An initial observation of Figure 8 highlights a significant difference in KGE and r for satellite (GOr, IOr) and satellite-gauge (GM3, GMm, GR3, GRm, IM3, IMm, IR3, IRm) products when moving from daily to 3-daily aggregates. While the median values of KGE varied from 0.123 (IOr) to 0.294 (GR3) for daily aggregates, this performance increased to a range from 0.519 (IOr) to 0.756 (GM3, GR3) for 3-daily aggregates. In the case of monthly rainfall totals, all satellite and satellite-gauge products presented a good performance, which is more uniform among products. The median values of KGE varied from 0.697 (IM3) to 0.800 (GOr), a shorter interval when compared with daily and 3-daily aggregates. On the other hand, the gauge-based IDW presented a more similar KGE and r among aggregation classes. The median KGE was calculated as 0.694, 0.750, and 0.785 for daily, 3-daily, and monthly aggregates, respectively. Nevertheless, the performance of satellite-derived rainfall was comparable with the IDW interpolation of rain gauges in the case of 3-daily and monthly aggregates, presenting similar or even better KGE values.

Another important aspect when selecting the optimal rainfall product refers to β, or the tendency to underestimate or overestimate the observed data. It is important to highlight that β does not change among aggregation classes because it is calculated based on the rainfall totals of the entire time series. The bias ratio is extremely important to evaluate the capacity of each product to represent the observed rainfall volumes. This is particularly relevant in hydrological studies such as flood hazard assessments, given that the rainfall volume is associated with the simulated discharges through rainfall-runoff processes. Overall, it was observed that GOr is the only product that tends to underestimate the rainfall amounts. The calculated median β of 0.971 indicated that the product's estimates sum 97.1% of the observed measurements for the entire time series. In addition, all adopted merging techniques (GM3, GMm, GR3, GRm) increased the median β of the GSMaP product. In its turn, IDW and all IMERG-derived (IOr, IM3, IMm, IR3, IRm) products presented a tendency to overestimation, ranging from a median of 1.049 (IM3) to 1.145 (IOr). It is important to highlight that satellite-derived products often present different performances when representing different rainfall intensity classes. Therefore, the validation of the products per intensity class can provide important insights about the ability of the product to represent specific rainfall events. In this study, this analysis was performed based on the rainfall percentiles and is presented in Chapter 29.2.2.

In addition to an overall analysis of median coefficients, boxplots are an important tool to understand how accurately the spatial rainfall variability is captured by each rainfall product. These graphs represent the variability of the statistical indices among all rain gauges adopted for validation. Considering that each rain gauge is associated with a specific location in the basin, the boxplots can represent not only the overall performance of the product but also how consistent they are in space. To support the visualization of this spatial variability, Figure 9 and Figure 10 illustrate the calculated KGE index for each product (y-axis) and each aggregation level (x-axis). The large colored points represent the KGE values at the rain gauges adopted for validation, while the small black points represent the rain gauges that served as a source for the bias correction of satellite products and the interpolation of the gauge measurements.

In this context, it is interesting to analyze the performance of the IDW product, particularly regarding the KGE and r indices. The IDW boxplots presented a high interval between the lowest and highest values, and high variability in the interquartile range (IQR). Taking as an example the KGE values for daily aggregates, the difference between the minimum (0.386) and the maximum (0.811) values was considerably higher than in the other products (except IM3). This high variability contrasted with a median KGE value of 0.694, a significantly better performance than all satellite and satellite-gauge products. When visualizing the performance of IDW for daily aggregates (Figure 10), it is noted that the highest KGE values – from 0.6 to 0.9 – were concentrated in the center and south of the basin, near the source rain gauges.

Figure 9: Spatial validation of the modified Kling-Gupta Efficiency (KGE) per product for daily, 3-daily, and monthly totals (part 1). The black dots represent the source gauges from Group 1.
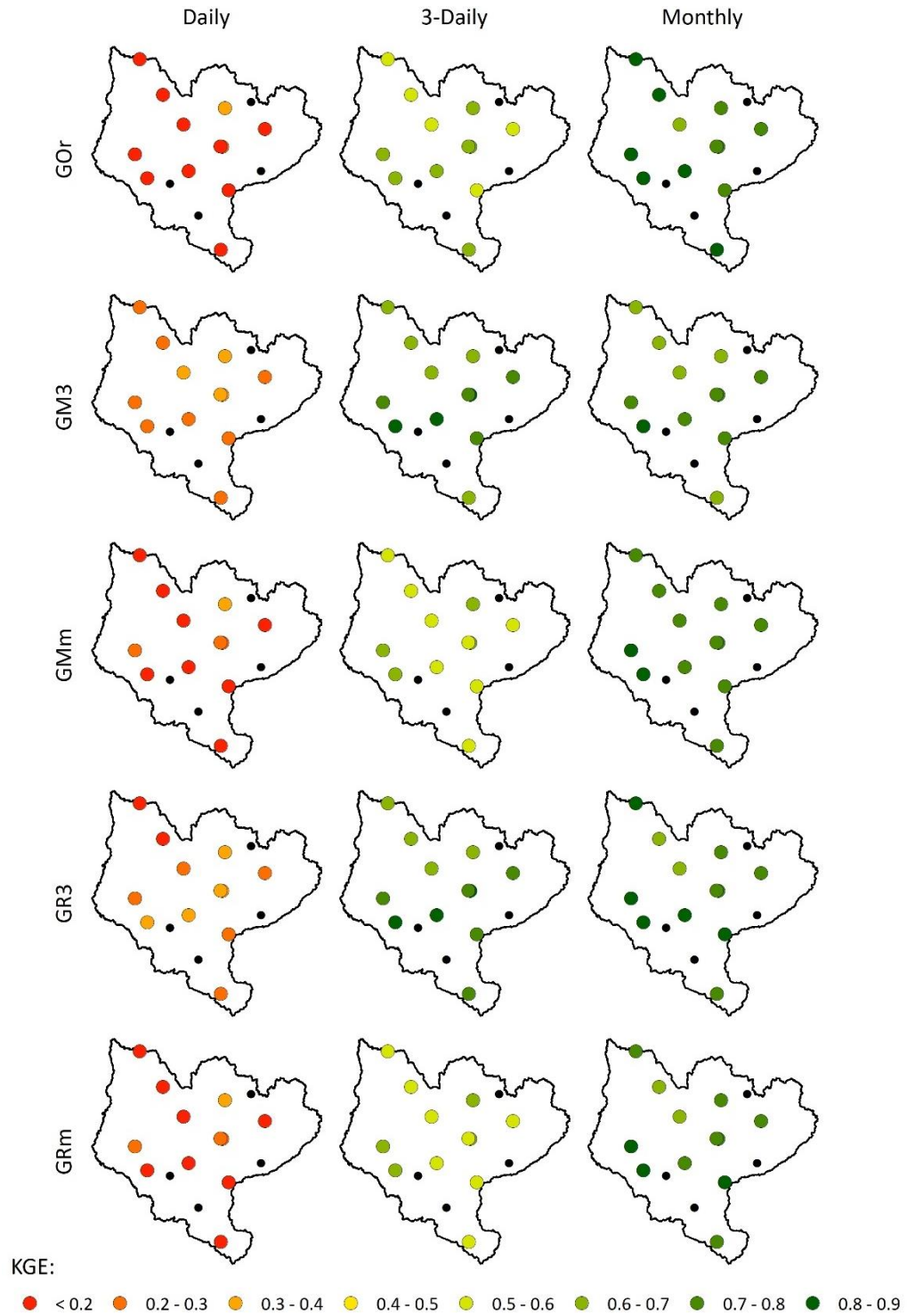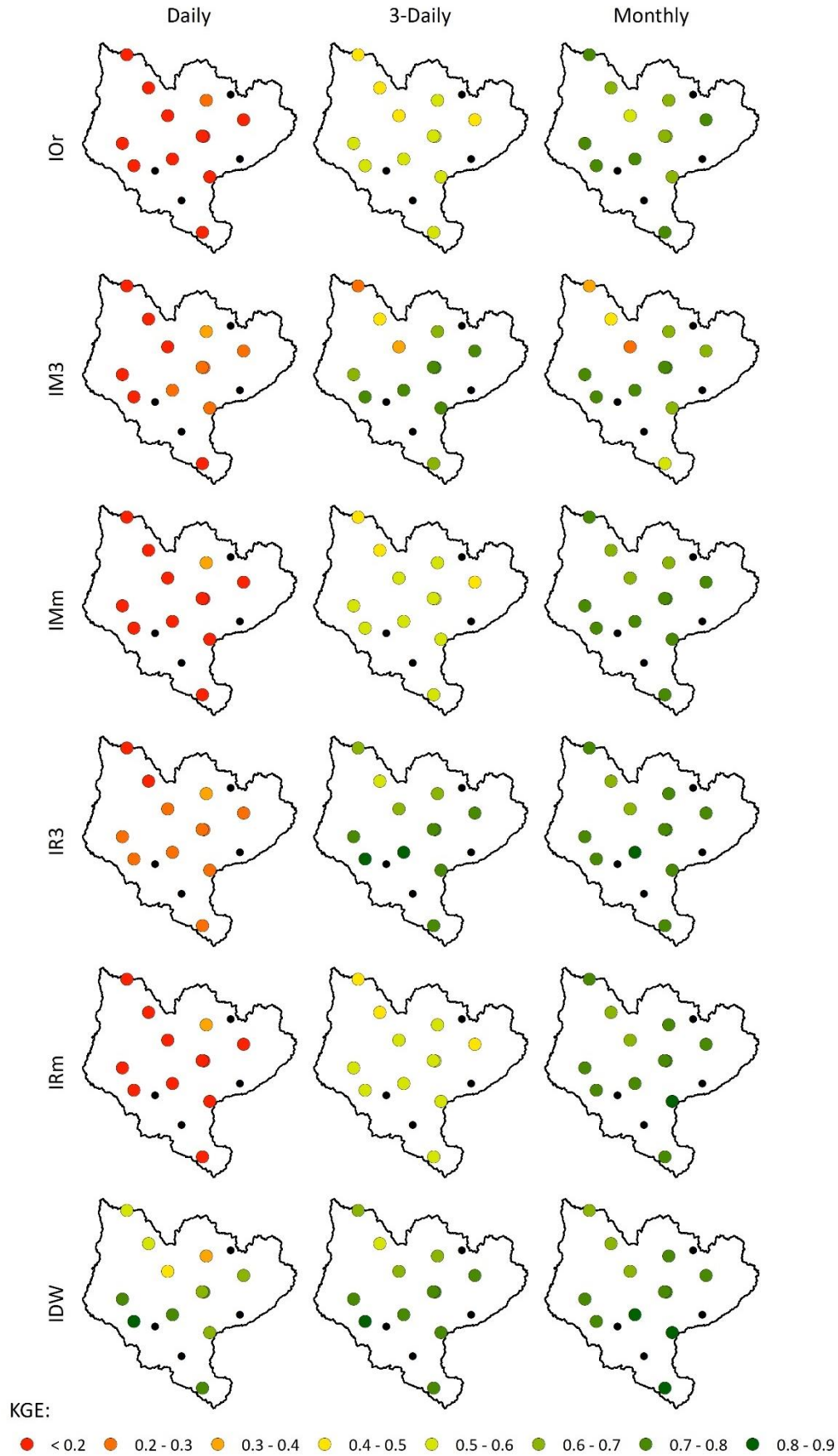
Figure 10: Spatial validation of the modified Kling-Gupta Efficiency (KGE) per product for daily, 3-daily, and monthly totals (part 2). The black dots represent the source gauges from Group 1.

Regarding the satellite-derived products, the merging techniques increased the overall performance of the rainfall estimates for daily and 3-daily aggregates. However, the methods were considerably better when adopting 3-daily timesteps (GM3, GR3, IM3, IR3), as observed in the calculated KGE values (Figure 8). In the case of GSMaP, the merging methods increased the median KGE from 0.158 (GOr) to 0.287 (GM3) and 0.294 (GR3) for daily aggregates, and from 0.608 (GOr) to 0.756 (GM3) and 0.756 (GR3) for 3-daily aggregates. In the case of IMERG, the methods increased the median KGE from 0.123 (IOr) to 0.203 (IM3) and 0.251 (IR3) for daily aggregates, and from 0.519 (IOr) to 0.700 (GM3) and 0.738 (GR3) for 3-daily aggregates. In addition, the GM3 and GR3 presented a slightly better performance than IDW for 3-daily aggregates, with a KGE of 0.756 – for both products – against 0.750. These figures indicated an overall better performance of GSMaP-derived when compared with IMERG-derived rainfall estimates. Regarding the comparison between the merging techniques, RIDW proved to be slightly better than MBC, but the differences were subtle. The only exception was the IM3 product, which presented an unusual variability of the statistical indices among the analyzed gauges, as observed in the boxplots in Figure 8 and the maps in Figure 10.

Despite the potential of the merging techniques to increase the accuracy of satellite estimates, as demonstrated in the previous paragraph, it is essential to evaluate how they affected the representation of the spatial rainfall variability. Notably, both the MBC and RIDW techniques increased the variability of the KGE values among the rain gauges. The GM3, GR3, IM3, and IR3 products presented a higher variability of KGE and r when compared with GOr and IOr for 3-daily aggregates, as represented by the size of the interquartile range in the boxplots. In this context, the analysis of Figure 9 and Figure 10 indicated that the merging techniques have a higher potential to improve the accuracy of the rainfall estimates closer to the locations of the source gauges, with lower KGE concentrated mostly in the north of the basin, which is more distant from the source rain gauges.

4.2.2   Validation per rainfall intensity class

The Kling-Gupta Efficiency (KGE) and its corresponding components of bias ratio (β), variability ratio (γ), and linear correlation (r) were also calculated for three rainfall intensity classes, according to the equations presented in Chapter 3.5. In this case, 3-daily aggregates were adopted as a reference for comparison because of their significantly better performance when compared to daily aggregates. In addition, 3-daily aggregates can still capture storm events, which are smoothed out in monthly aggregates. Figure 11 presents the performance (y-axis) of the rainfall products for the intensity classes of 50th to 70th percentile, 70th to 90th percentile, and above the 90th percentile (x-axis). An overview of the thresholds associated with the rainfall percentiles in each gauge is presented in Appendix 2.

The visualization of Figure 11 highlighted a strong difference of β among the rainfall intensity classes. In one hand, the rainfall products overestimated the rainfall measurements between the 50th and 90th percentiles, ranging from a median β of 1.432 (IR3) to 1.752 (IOr). On the other hand, all products underestimated the measurements above the 70th percentile. In this context, the potential of merging techniques is noteworthy. For GSMaP-derived products, the median β improved from 0.804 (GOr) to 0.952 (GM3) and 0.980 (GR3) between the 70th and 90th percentiles, and from 0.600 (GOr) to 0.840 (GM3) and 0.830 (GR3) above the 90th percentile. In the case of IMERG-derived products, the merging techniques maintained a low bias of the original product between the 70th and 90th percentiles, varying from 0.984 (IOr) to 0.968 (IM3) and 0.973 (IR3). For the 90th percentile, the median β improved from 0.656 (IOr) to 0.805 (IM3) and 0.826 (IR3). It is interesting to notice that the GR3 and IM3 products resulted in a better β when compared with IDW. The IDW product presented a median β of 0.972 between the 70th and 90th percentiles, and 0.819 above the 90th percentile.
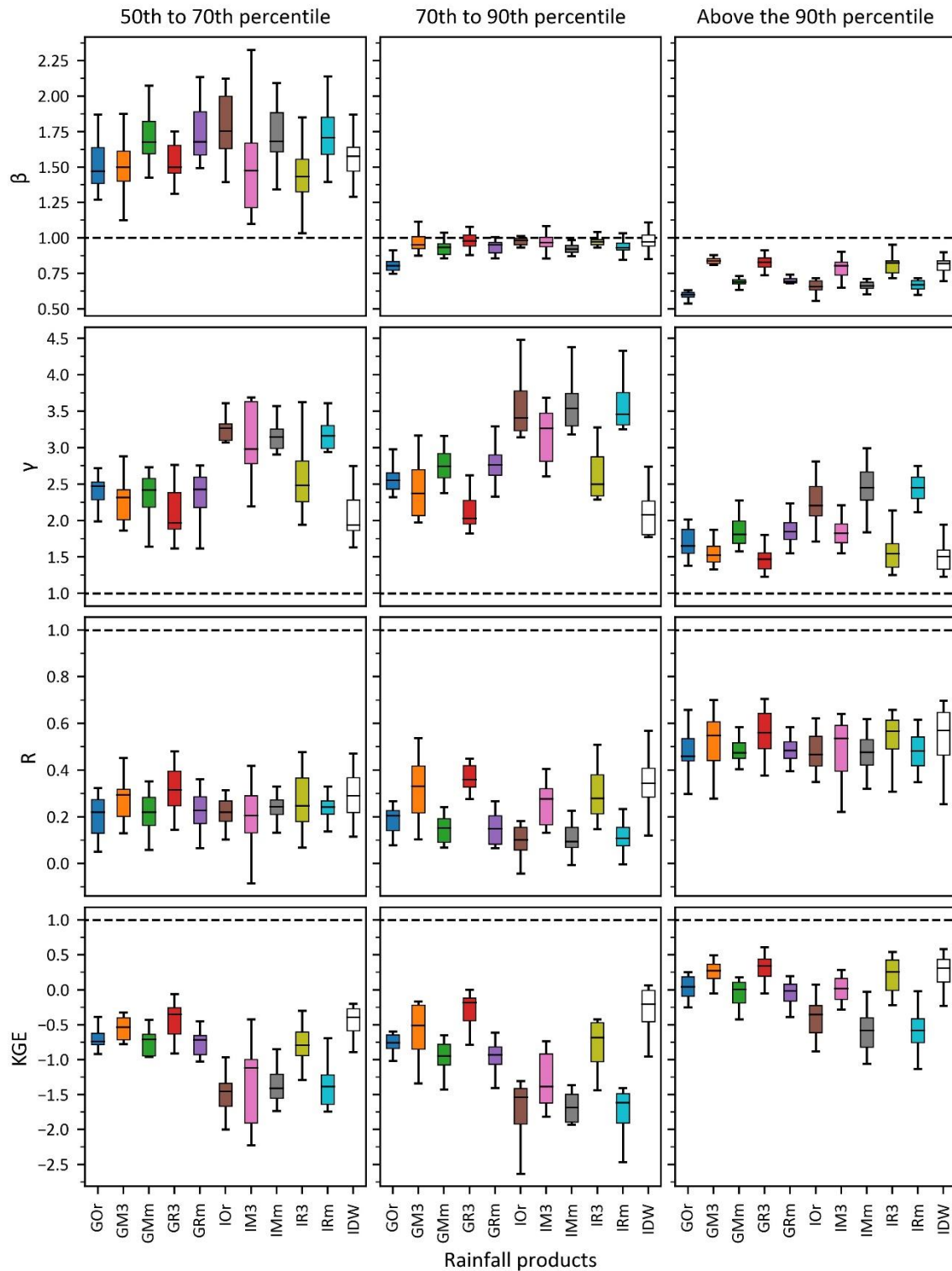
Figure 11: Validation of the rainfall products per intensity class. Statistics of bias ratio (β), variability ratio (γ), linear correlation (r) and modified Kling-Gupta Efficiency (KGE) per product for 3-daily totals.

In terms of KGE, the GR3 product presented the best performance for all intensity classes. The median KGE was calculated as -0.347 between the 50th and 70th percentiles, -0.184 between the 70th and 90th percentiles, and 0.344 above the 90th percentiles. The class above the 90th percentile is related to the representation of rainfall extremes. Therefore, the GR3 product had similar performance with IDW, which

presented a median KGE of 0.314. This pattern was also observed in the median values of r – 0.560 (GR3) against 0.569 (IDW) – and γ – 1.469 (GR3) against 1.505 (IDW). In addition, the comparison highlighted a better performance of GSMaP when compared with IMERG products, as also demonstrated in the overall validation. Between the 50th and 70th percentiles, GOr presented a median KGE of -0.734 against -1.453 for IOr. Between the 70th and 90th percentiles, the median KGE was calculated as -0.753 for GOr against -1.535 for IOr. Finally, for the values above the 90th percentile, the median KGE was calculated as 0.046 for GOr against -0.352 for IOr. A better performance was also observed in the GM3 and GR3 products when compared with IM3 and IR3, respectively.

4.2.3   Selected rainfall product

Overall, GR3 proved to be the most accurate rainfall product to represent the intensities for 3-daily totals, regardless of the intensity class. However, despite this predominantly better performance, the GOr product was preferred as a rainfall input to generate the design storms for the hydrological model (see Chapter 4.3). GOr was selected considering the main objective of this study, which aims to represent the spatial rainfall variability as accurately as possible. Therefore, while the RIDW merging technique presented a high potential to correct satellite estimates, the uncertainties associated with the gauge network density remain a challenge. This is the case of the north of the basin, where there are no rain gauges available to perform the merging technique. This limitation can be better visualized in Figure 9 and Figure 10. In this sense, it was assumed that the adoption of a merging technique could add noises to the representation of spatial patterns, hindering the analysis. This does not mean, however, that the GR3 product should not be applied in hydrological studies. Depending on the users' purposes, the product can provide more accurate estimates of rainfall intensity, considering the potential of the RIDW method to correct bias.

4.3   Generation of design storms

4.3.1   Gumbel distribution

The generation of design storms started with the extraction of the annual maxima series for 12 durations from 1 to 24 hours, as indicated in Chapter 3.6.1. The GOr product was adopted a rainfall input to extract the time series from hourly rainfall estimates. These series were applied to calculate the empirical probability of extreme rainfall events, later converted to the Gumbel reduced variate (see Chapter 3.6.2). Finally, a linear function was fitted to the series of rainfall annual maxima (see Chapter 3.6.3). Ideally, the coefficient of determination (R^2) of the linear function should be 1.0, which represents a perfect correlation between the fitted function and the empirical data. Because the design storms were generated per pixel, a total of 195 linear functions were adopted for each duration, which refers to the number of GOr pixels intersecting the study area. Figure 12 presents the dispersion of the R^2 values among the analyzed pixels, per duration.
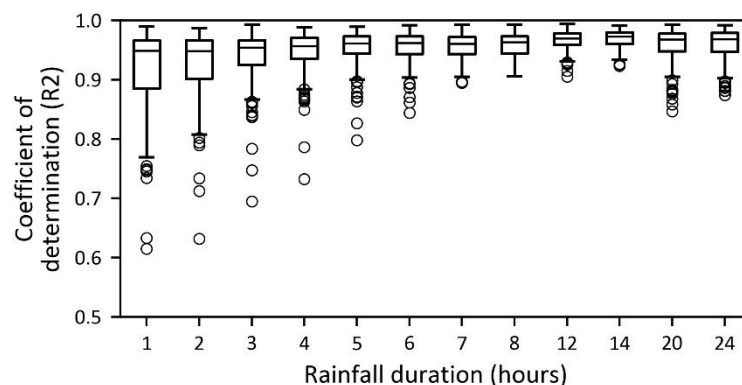
Figure 12: Performance of the Gumbel distribution fitting among pixels, per rainfall duration.

It was observed that the lowest correlations were registered for shorter durations, with R^2 values below 0.8 for durations from 1 to 4 hours, mostly related to outliers. On the other hand, all durations equal to or above 5 hours presented R^2 values between 0.8 and 1.0. In any case, the median R^2 was always higher than 0.95, regardless of the duration. This indicates an overall good fit of the linear functions to the series of rainfall annual maxima, with a few outliers. Figure 13 illustrates the maximum and minimum R^2 values, calculated for a duration of 1 hour. As demonstrated in the graph (b), the lower correlation of 0.61 was attributed to an extreme rainfall intensity that deviates from the linear distribution.
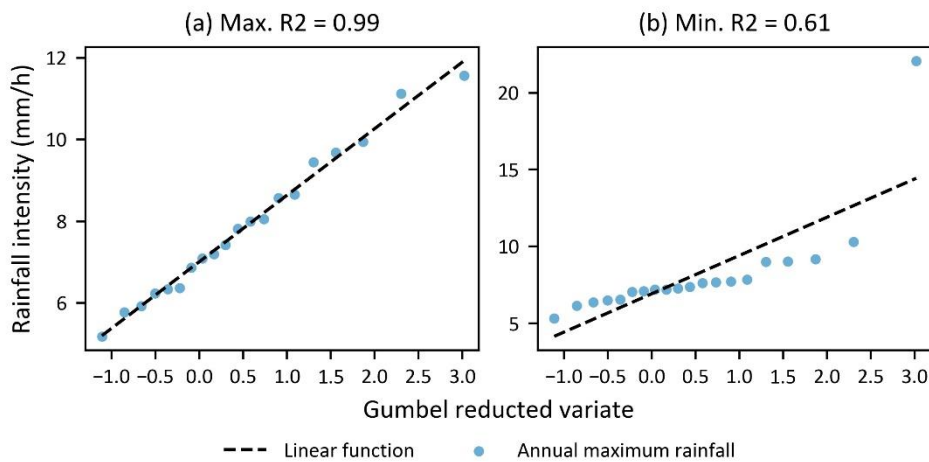
Figure 13: Examples of the maximum (a) and minimum (b) performance of the Gumbel distribution fitting. Both examples were extracted for a rainfall duration of 1 hour.

4.3.2   IDF curves

The fitted linear functions were applied to estimate the rainfall intensities per duration for four return periods – 2, 5, 10, and 25 years – that represent the probability of occurrence of the rainfall events (see Chapter 3.6.4). The combinations of rainfall intensity and duration were then adopted to generate intensity-duration-frequency (IDF) curves, one for each return period (see Chapter 3.6.5). To further investigate the influence of the spatial rainfall variability on the generation of IDF curves, statistical parameters were calculated from the group of 195 curves representing the variability among pixels. This included the mean, maximum, minimum, and standard deviation. Figure 14 presents the results obtained from this analysis. The analysis of the minimum and maximum curves (Figure 14b) demonstrated a considerable spatial variability of the rainfall intensities over the study area, especially in the case of higher return periods and shorter durations. As an example, for a duration of 1 hour, a rainfall intensity of 12 mm/h can be associated with a return period of 5 or 25 years, depending on the location. This overlay can also be visualized in the shaded areas representing the standard deviation (Figure 14a), with several intersections among the return periods of 5, 10, and 25 years.
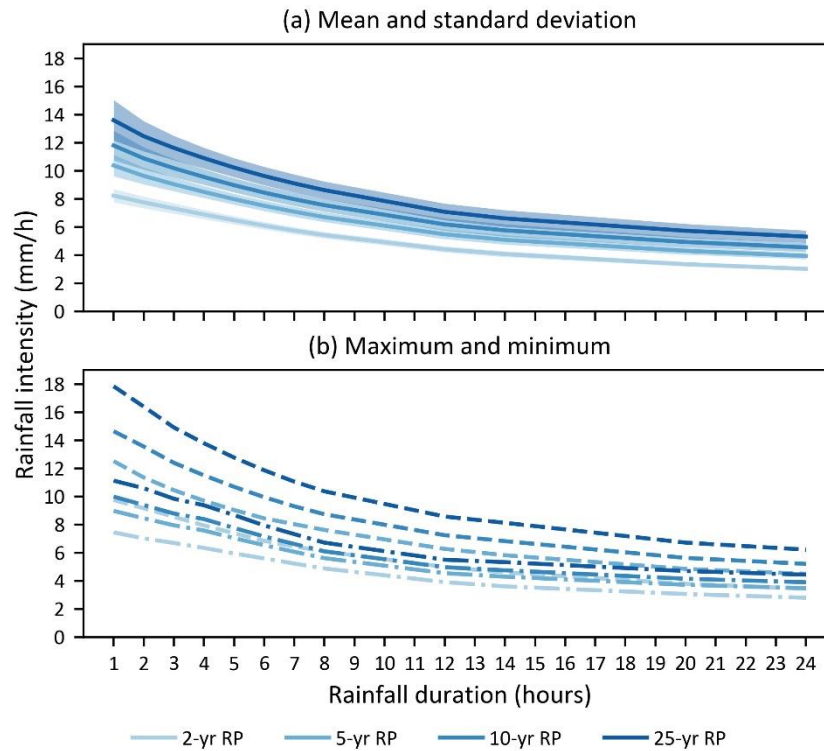
Figure 14: Variability of IDF curves among pixels. (a) Mean and standard deviation values among IDF curves, represented as a solid line and a shaded area, respectively. (b) Maximum and minimum values among IDF curves, represented as a dashed line and a dash-dotted line, respectively.

4.3.3   Design storms

The design storms were generated from the IDF curves according to the method presented in Chapter 3.6.6. The alternating block method was applied to create a rainfall event of 24 hours of duration, divided into hourly intervals. Different hyetographs were generated at the locations of each pixel of the GOr product, thus accounting for the spatial rainfall variability in the region. The generation of design storms resulted in rainfall maps for the analyzed return periods of 2, 5, 10, and 25 years. Figure 15 Figure 18 present the hyetographs and the rainfall totals for each design storm. The hyetographs (a) represent the temporal patterns of the design storms and were calculated as the mean rainfall intensity over the basin. As expected, the hyetographs maintained similar shapes among the different design storms, but the rainfall peak intensity increased from 8.19 to 13.41 mm/h when moving from a return period of 2 to 25 years. In its turn, the maps of cumulative rainfall (b) represent the spatial patterns of the distributed design storms. Notably, the highest rainfall amounts were concentrated in the center and south of the basin, mostly over the Itajaí do Sul, Itajaí do Oeste, and Itajaí-Mirim sub-catchments. In addition, the difference between the minimum and maximum cumulative rainfall was more intense for higher return periods, reaching a variation of 39 mm for 25 years.
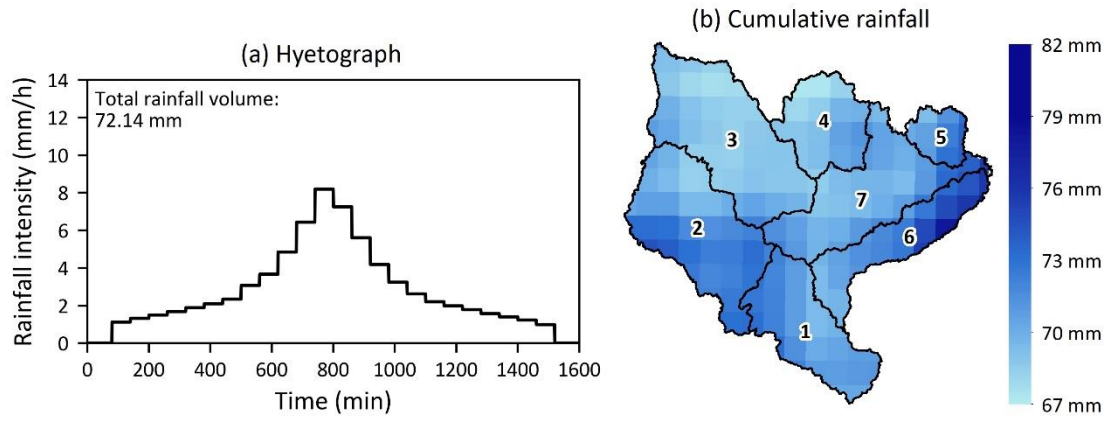
1. Itajaí do Sul | 2. Itajaí do Oeste | 3. Itajaí do Norte | 4. Benedito | 5. Luiz Alves | 6. Itajaí-Mirim | 7. Itajaí-Açu

Figure 15: Mean hyetograph (a) and map of cumulative rainfall (b) for the generated design storm with a return period of 2 years.
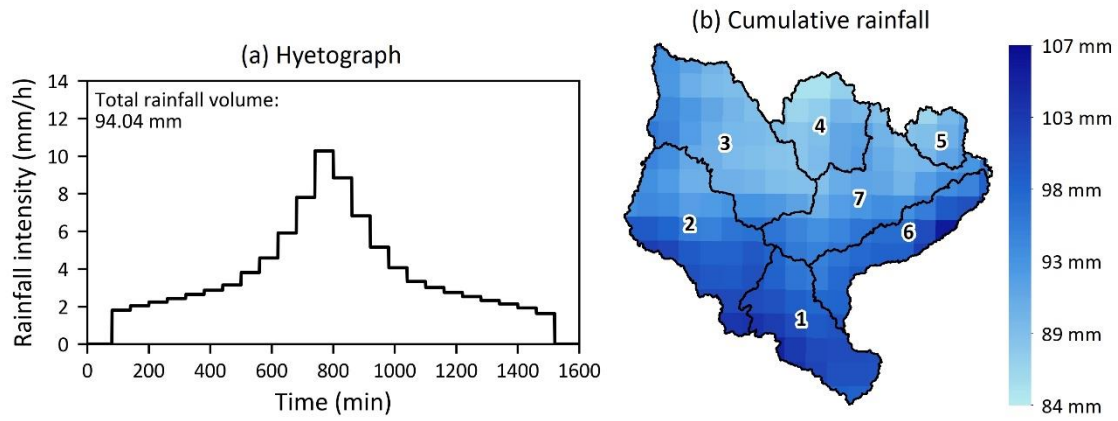
1. Itajaí do Sul | 2. Itajaí do Oeste | 3. Itajaí do Norte | 4. Benedito | 5. Luiz Alves | 6. Itajaí-Mirim | 7. Itajaí-Açu

Figure 16: Mean hyetograph (a) and map of cumulative rainfall (b) for the generated design storm with a return period of 5 years.
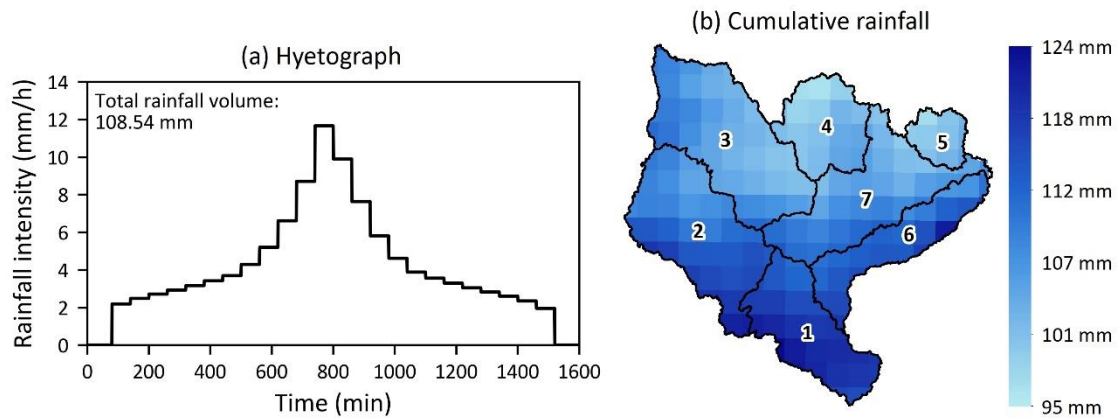
1. Itajaí do Sul | 2. Itajaí do Oeste | 3. Itajaí do Norte | 4. Benedito | 5. Luiz Alves | 6. Itajaí-Mirim | 7. Itajaí-Açu

Figure 17: Mean hyetograph (a) and map of cumulative rainfall (b) for the generated design storm with a return period of 10 years.

1. Itajaí do Sul | 2. Itajaí do Oeste | 3. Itajaí do Norte | 4. Benedito | 5. Luiz Alves | 6. Itajaí-Mirim | 7. Itajaí-Açu
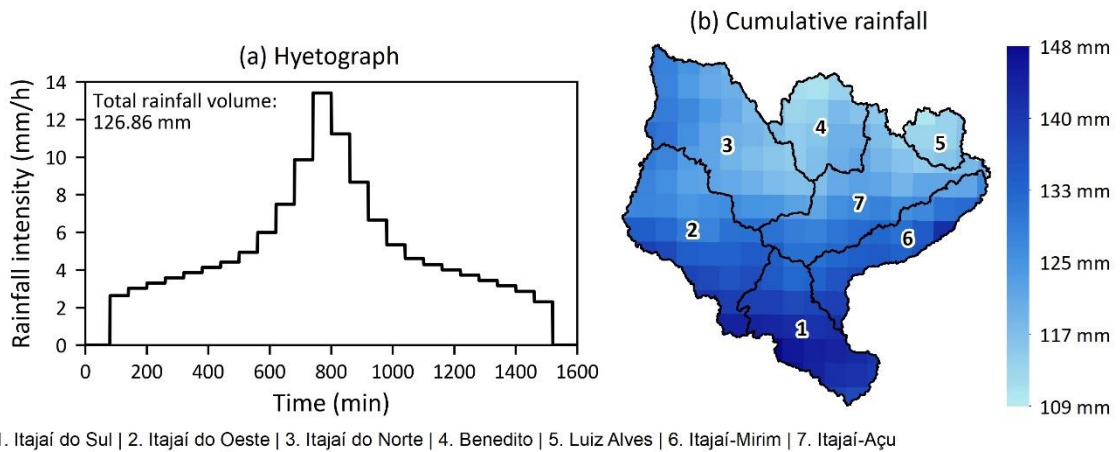
Figure 18: Mean hyetograph (a) and map of cumulative rainfall (b) for the generated design storm with a return period of 25 years.

The generated design storms were applied as rainfall inputs to simulate all scenarios presented in Table 2. In this case, the original rainfall maps were adopted to represent the scenarios of spatially distributed design storms. On the other hand, the hyetographs of the mean rainfall intensity – as presented in Figure 15a to Figure 18a – were adopted to simulate the scenarios of spatially uniform design storms. The results of the simulations are presented in Chapter 39.5.

4.4 Preparation of OpenLISEM hydrological model

4.4.1 Resampling of the DTM

As described in Chapter 3.7.1, the large scale of the analysis required the adoption of a DTM with a coarser resolution in the hydrological model. Therefore, the original DTM was resampled to a spatial resolution of 100 meters. During this process, different resampling techniques were evaluated in terms of their ability to represent the geometry of the basin. Table 7 presents the comparison among the techniques for the estimation of the total catchment area and the main river length. The results demonstrated that the analyzed parameters were highly insensitive to changes in the resampling technique, as previously indicated in the studies of Goyal, Panchariya, Sharma, & Singh (2018), Shen & Tan (2020), and Tan, Ramli, & Tam (2018). The similarity of the results might be influenced by the mountainous topography of the basin, with very well-delimited hydrological features. Another relevant result is the error in the estimation of the main river length. While the total catchment area was overestimated by only 0.10%, the main river network was underestimated by -9.61%, on average. A possible cause for this underestimation is the high amount of river meanders in the basin, which are common on the flat surfaces of the floodplains. In this case, the adoption of a low-resolution DTM possibly affected the delineation of the river network, rectifying the existing meanders on the floodplains, where elevation changes are not substantial.

Table 7: Evaluation of the DTM resampling techniques in comparison with the reference features.

Parameter	DTM-derived			Reference features	Selected technique
	Nearest neighbor	Bilinear interpolation	Cubic convolution		
Total catchment area (km²)	14,881.7	14,881.7	14,881.6	14,866.3	Similar performance (cubic convolution)
Main river length (km)	299.4	299.0	298.7	330.8	Similar performance (nearest neighbor)

A visual inspection was later conducted to further investigate the agreement between the DTM-derived and the reference drainage networks. Figure 19 illustrates the results obtained from this analysis, with a focus on four locations with different characteristics.
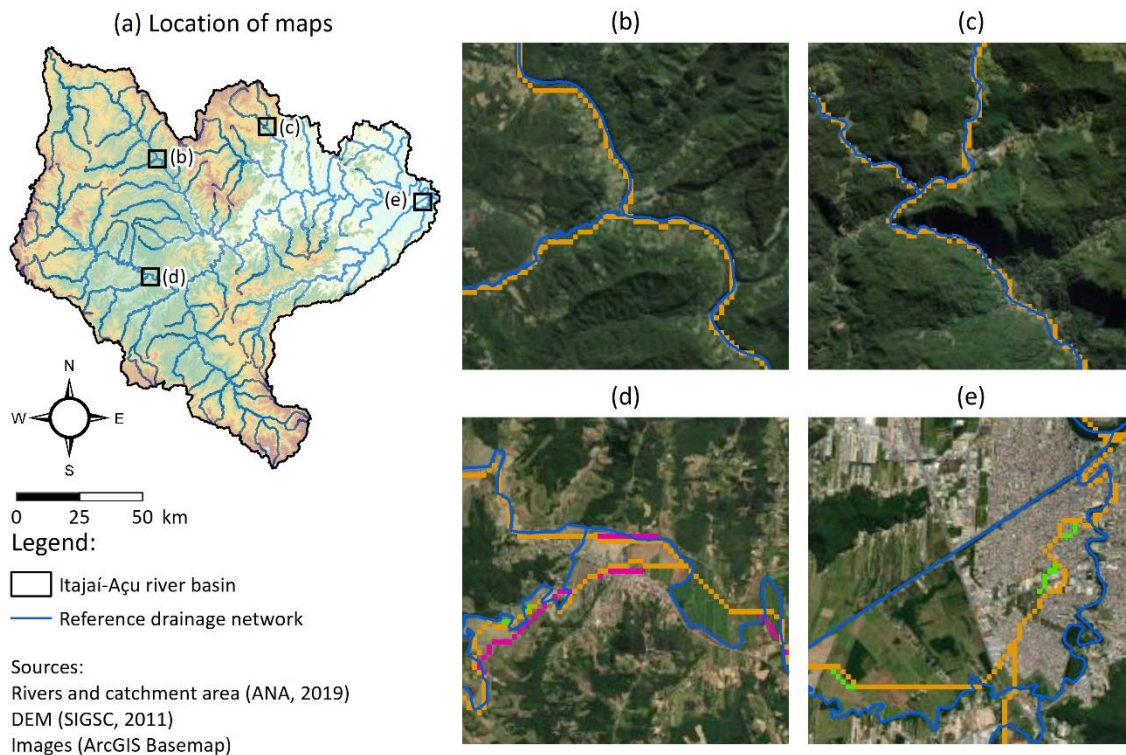
Figure 19: Visual inspection of the DTM resampling techniques of nearest neighbor (orange), bilinear interpolation (green), and cubic convolution (pink) in comparison with the reference features. The predominance of the orange line indicates an overlay of the DTM-derived features.

Analogously to the previous findings, the selection of the resampling technique did not seem to affect the delineation of the drainage network. In addition, the DTM-derived features presented a good agreement with the reference network along narrow valley bottoms surrounded by mountains (Figures 19c and 19d). On the other hand, larger differences were observed on the floodplains (Figures 19e and 19e), where the river delineation seems to be more sensitive, possibly because of smaller elevation changes. Therefore, considering the similar performance of the resampling techniques, the nearest neighbor was preferred. This technique was selected to maintain, as much as possible, the original elevation values of the DTM.

4.4.2   Calibration of the hydrological model

The calibration of the OpenLISEM hydrological model was performed through the simulation of the 2013 historical flood event. To calibrate the model, the parameters were initially settled according to the assumptions presented in Chapter 3.7.1. This includes the estimations of the Manning's roughness coefficient – 0.03 for the channel, Table 4 for the land use classes – and the fraction of initial soil moisture – 50%. Hourly rainfall maps were obtained from GOr, the selected rainfall product. It is important to mention that GOr tends to underestimate the rainfall intensities, especially in the case of extremes. Therefore, the calibration of the model's parameters is essential to minimize these effects, thus producing a more realistic simulation of rainfall-runoff processes.

The 2013 rainfall event was first analyzed in terms of its spatial and temporal characteristics, as illustrated in Figure 20. The rainfall event had a total duration of 1,920 minutes (32 hours), reaching a mean peak intensity of 6.73 mm/h at the minute 1,140 (22-09-2013 02:00 GMT-3), according to the GOr estimates.

The total rainfall volume ranged from 62 to 122 mm over the driest and wettest pixels of GOr, respectively, with an average of 85.36 mm. Average, in this context, refers to the spatial scale, or the mean value among the analyzed pixels. The highest rainfall amounts were observed upstream, concentrated mostly over the Itajaí do Oeste and Itajaí do Norte sub-catchments. The validation of the GOr estimates against 19 rain gauges with measurements on the date of the event indicated a linear correlation of 0.453 and a bias ratio of 0.619, thus highlighting the previously mentioned underestimation of the GOr product.

1. Itajaí do Sul | 2. Itajaí do Oeste | 3. Itajaí do Norte | 4. Benedito | 5. Luiz Alves | 6. Itajaí-Mirim | 7. Itajaí-Açu
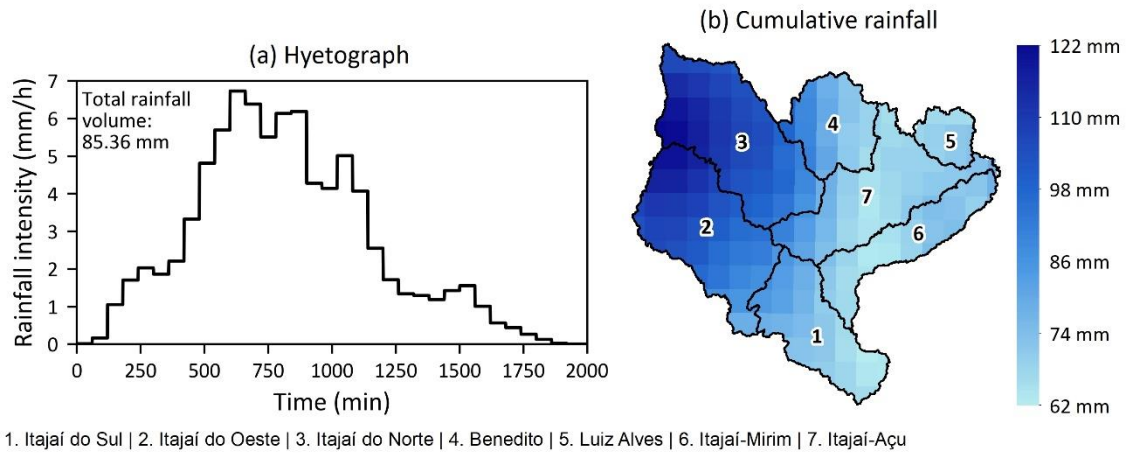
Figure 20: Mean hyetograph (a) and map of cumulative rainfall (b) for the 2013 rainfall event.

The model was calibrated by changing two parameters: the Manning's coefficient of the channels and the initial soil moisture content. This process was performed through a try and error approach, by simulating multiple combinations of the coefficients to find the best representation of the observed hydrograph. In addition to the visualization of the hydrograph, three statistical indices were calculated to support the analysis. These included the Nash-Sutcliffe Efficiency (NSE), and the errors in the estimation of peak intensity and total water volume. An overview of the methodology is presented in Chapter 3.7.2. The best calibration was obtained with a channel Manning's coefficient of 0.055 and 79% of initial soil moisture. According to the classification of Chow (1959), a Manning's between 0.045 and 0.060 represents a winding river with weeds and stones. Figure 21 illustrates the conditions of the riverbeds in four different locations in the Itajaí-Açu river basin. As observed in Figures 21b to 21e, rocks are present in multiple locations along with the drainage system, including in upstream, midstream, and downstream sections of the main rivers. Therefore, the condition in the study area enabled the assumption of a single Manning's coefficient for all channels in the basin.

The calibration process presented an excellent performance, with a calculated NSE of 0.97 at the location of the stream gauge Blumenau (PCD). The error in the flood peak intensity was 0.30%, or 4,369.26 m³/s of observed discharge against 4,382.50 m³/s of simulated. In its turn, the error in the total water volume was calculated as -1.74%, or 851.89 hm³ of observed total water volume against 837.09 hm³ of simulated. Figure 22 presents the hydrographs and the mean hyetograph obtained after calibration. As observed, the shape of the simulated hydrograph matched very accurately the observed hydrograph. This shape is influenced by the spatial and temporal patterns of the triggering rainfall event. Therefore, the calibration supports the assumption that the GOr product has a high potential to represent the spatial rainfall variability over the region, despite its tendency to underestimate intensities.
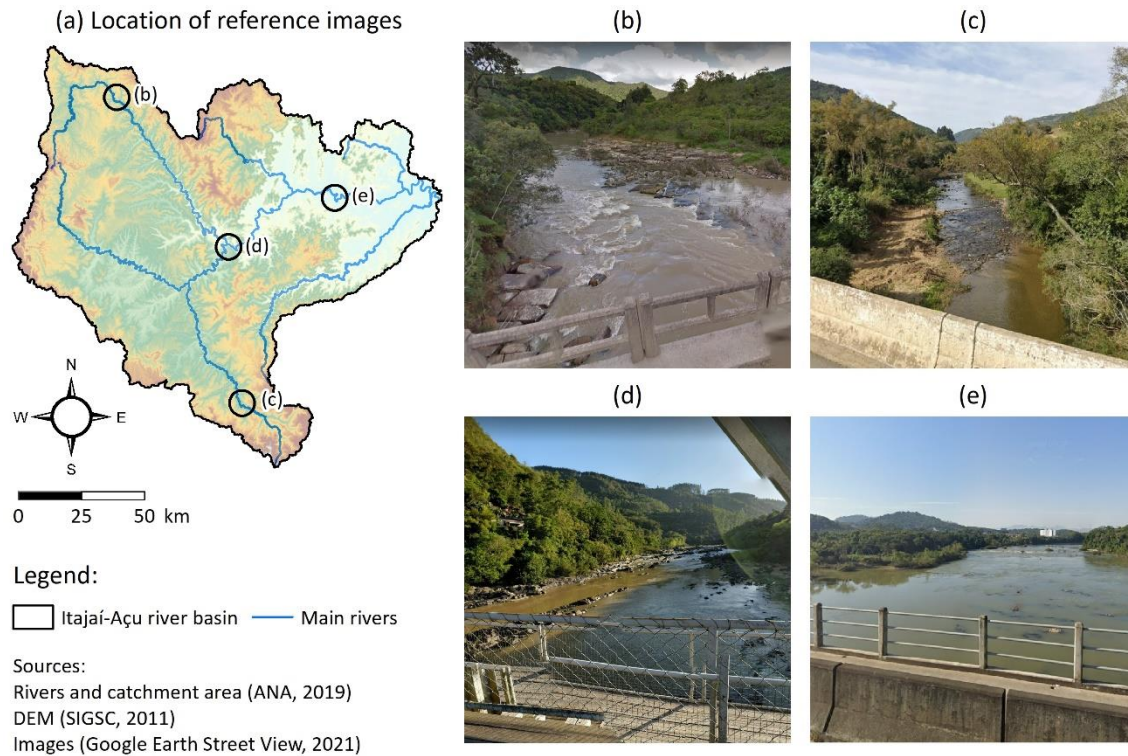
Figure 21: Images of the riverbed conditions in four sections of the Itajaí-Açu river basin. The reference map (a) indicates the location of the images (b), (c), (d), and (e).
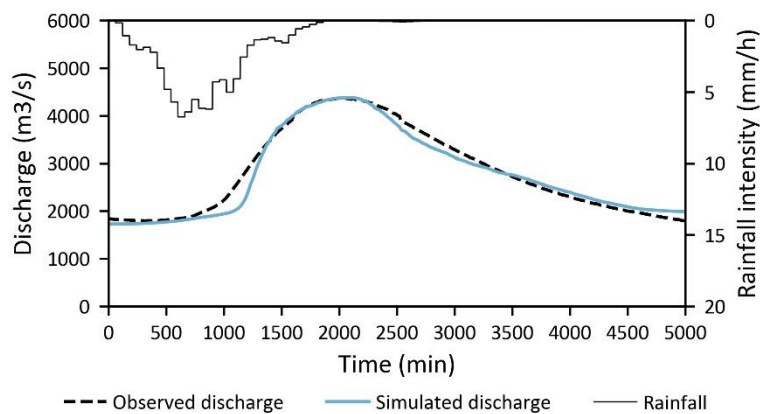
Figure 22: Observed and calibrated hydrographs of the 2013 flood event, with an indication of the triggering hyetograph.

4.4.3   Validation of the flood extent

The simulated flood extent was validated through its comparison with the observed flood in 2013 (see Chapter 3.7.2). Because of the limited availability of information on the extent of historical flood events, only a small area in the Municipality of Blumenau was analyzed. Figure 23 illustrates the comparison between the simulated and observed extents. The mask adopted to calculate the Kappa coefficient is highlighted as a dashed black line. In an initial visual inspection, it was observed that the simulated extent overestimated the flooded area. To further evaluate this hypothesis, the Kappa coefficient was calculated. Overall, the coefficient indicated a moderate agreement between the simulated and observed extents of the flood event, presenting a value of 0.49. In total, the simulated flood extent within the limits of the mask resulted in 647 true positives and 4,146 true negatives against 610 false positives and 292 false negatives. The considerably higher number of false positives against false negatives indicated an overestimation of the simulated event,

as previously observed in the visual inspection. However, considering the large scale of the analysis, a moderate agreement was considered satisfactory for this research, and the calibrated model was adopted for the simulation of the rainfall scenarios.
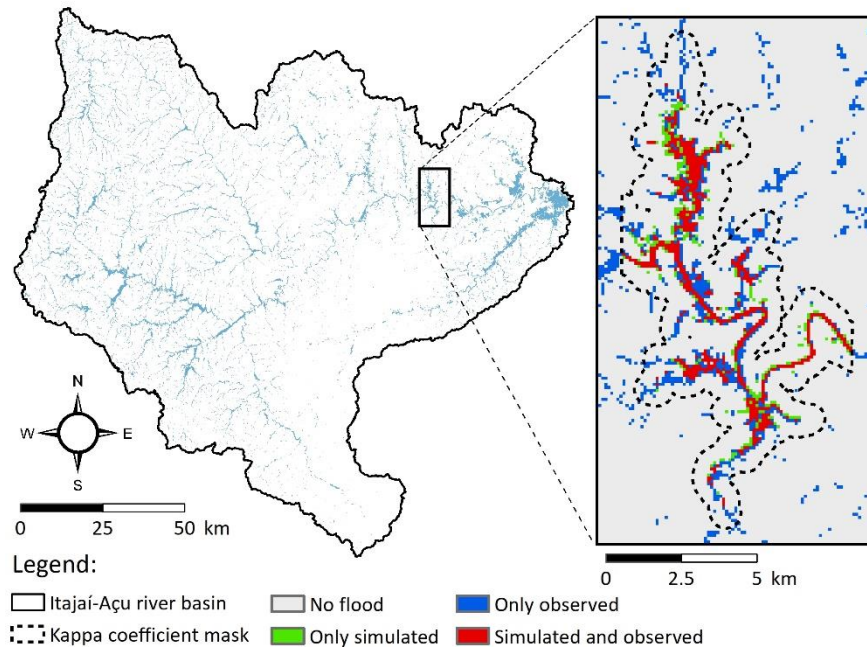
Figure 23: Observed and simulated flood extents of the 2013 event at the location of the Municipality of Blumenau. The dashed black line indicates the boundaries of the Cohen's Kappa coefficient mask.

4.5   Simulation of rainfall scenarios

4.5.1   Flood hazard

The design storms obtained in Chapter 4.3 were simulated in the calibrated hydrological model (see Chapter 4.4) to quantify flood hazard and exposure for the return periods of 2, 5, 10, and 25 years. An overview of the methodology is presented in Chapter 3.8, and the simulated scenarios are described in Table 5. Two different rainfall events were simulated for each return period: spatially distributed (SD) and spatially uniform (SU). The analyses focus on the comparison between both events. It is important to mention that, in all cases, the SD scenario was adopted as a reference. Therefore, positive variations indicate higher values in the SU when compared with the SD scenario, while negative variations indicate lower values.

To start the analysis, Figure 24 presents the simulated hydrographs per scenario. Each graph in the figure represents a section of the river, including the outlets of the sub-catchments and the main outlet of the Itajaí-Açu river basin. A complete overview of the values is presented in Appendix 3. Overall, the SU scenarios presented a considerably higher discharge at the outlets of the Itajaí do Norte, Benedito, and Luiz Alves sub-catchments. The variations were up to 23.76%, as in the case of the Itajaí do Norte sub-catchment for a 2-year event. In the case of the Itajaí do Sul sub-catchment, the SU peak discharge was considerably lower, presenting a maximum variation of -12.84% for a 25-year event. On the other hand, the variations between the SD and SU scenarios were less significant at the outlets of the Itajaí do Oeste and Itajaí-Mirim sub-catchments, and at the main outlet of the basin, with differences lower than $\pm 7\%$. Regarding absolute values, it was observed that the variation between rainfall scenarios increased with higher return periods. In this context, the highest variations in the flood peak discharge were observed at the outlets of the Itajaí do Sul and Itajaí do Norte sub-catchments for a 25-year event. The differences were 208 m³/s and 175 m³/s,

respectively. To exemplify the magnitude of these values, in both cases the variation was higher than the peak discharge at the outlet of the Luiz Alves sub-catchment for the same return period, calculated as 135 m³/s (SD) and 150 m³/s (SU).
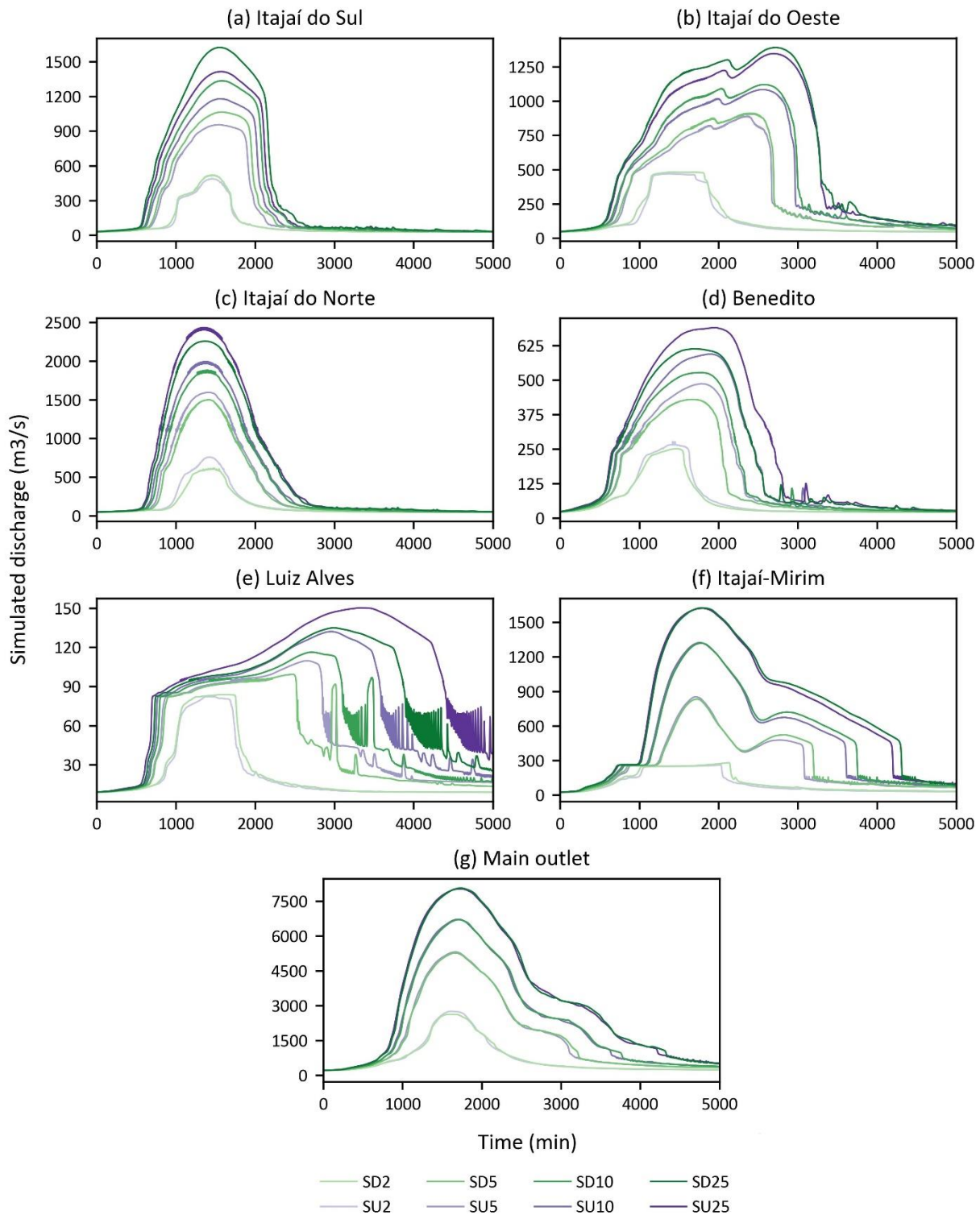
Figure 24: Simulated hydrographs for each rainfall scenario at the analyzed river sections. The color scales indicate the differences between scenarios of spatially distributed (green scale) and uniform (purple scale) rainfall.

Analogously to the peak discharge, the SU scenarios presented a higher total water volume at the outlets of the Itajaí do Oeste, Benedito, and Luiz Alves sub-catchments when compared with the SD scenarios. A

maximum variation of 20.74% was obtained at the outlet of the Luiz Alves sub-catchment for a 25-year event. In the case of the Itajaí do Sul, Itajaí do Oeste, and Itajaí-Mirim sub-catchments, the total water volume was lower in the SU scenarios. A maximum variation of -13.59% was obtained at the outlet of the Itajaí do Sul catchment for a 25-year event. The results at the main outlet of the basin were less sensitive to the rainfall scenarios, with variations lower than ±1.0% for all return periods.
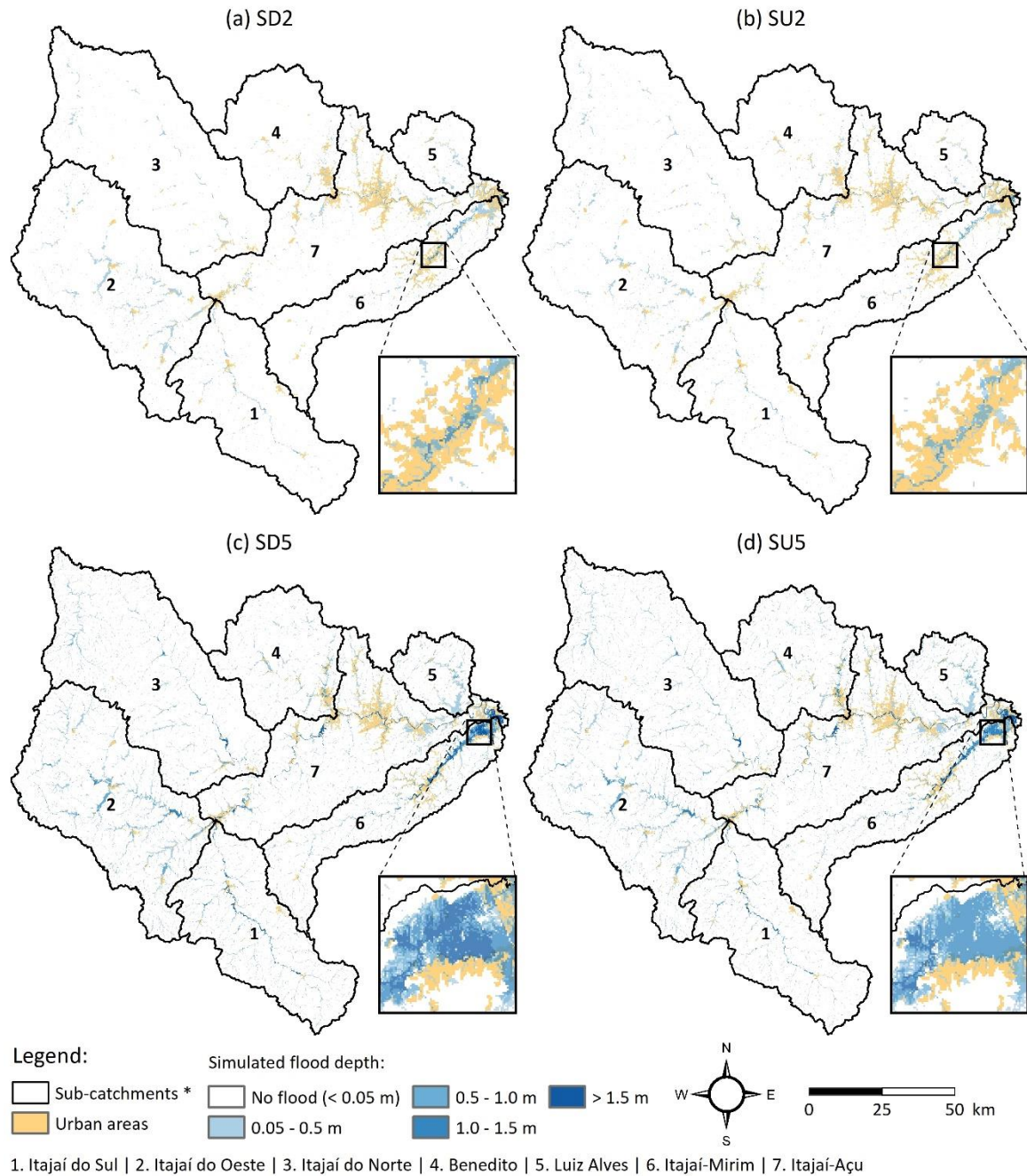
Figure 25: Simulated flood depths for the scenarios of spatially distributed (a, c) and uniform (b, d) design storms, for the return periods of 2 (a, b) and 5 (c, d) years. The small squares highlight locations with differences in flood depth between spatially distributed and uniform rainfall.

Another important analysis is the contribution of each sub-catchment to the total water volume at the main outlet of the Itajaí-Açu river basin. Taking as reference the SD scenarios, the total water volume for a 2-year event was estimated as 446.66 hm³. The largest contribution was from the Itajaí-Açu sub-catchment (23.48%), followed by the sub-catchments of Itajaí do Oeste (19.35%), Itajaí do Norte (17.48%), Itajaí-

Mirim (14.83%), Itajaí do Sul (13.50%), Benedito (8.11%), and Luiz Alves (3.21%). Moving to the less frequent event with a return period of 25 years, a total water volume of 1,931.83 hm³ received the largest contribution from the Itajaí-Mirim sub-catchment (22.67%), followed by the sub-catchments of Itajaí do Oeste (20.21%), Itajaí do Norte (18.36%), Itajaí-Açu (15.72%), Itajaí do Sul (13.85%), Benedito (6.59%), and Luiz Alves (2.56%).

To investigate the effects of these variations on the quantification of flood hazard and exposure, Figure 25 and Figure 26 illustrate the flood extents for each scenario, classified by flood depth.
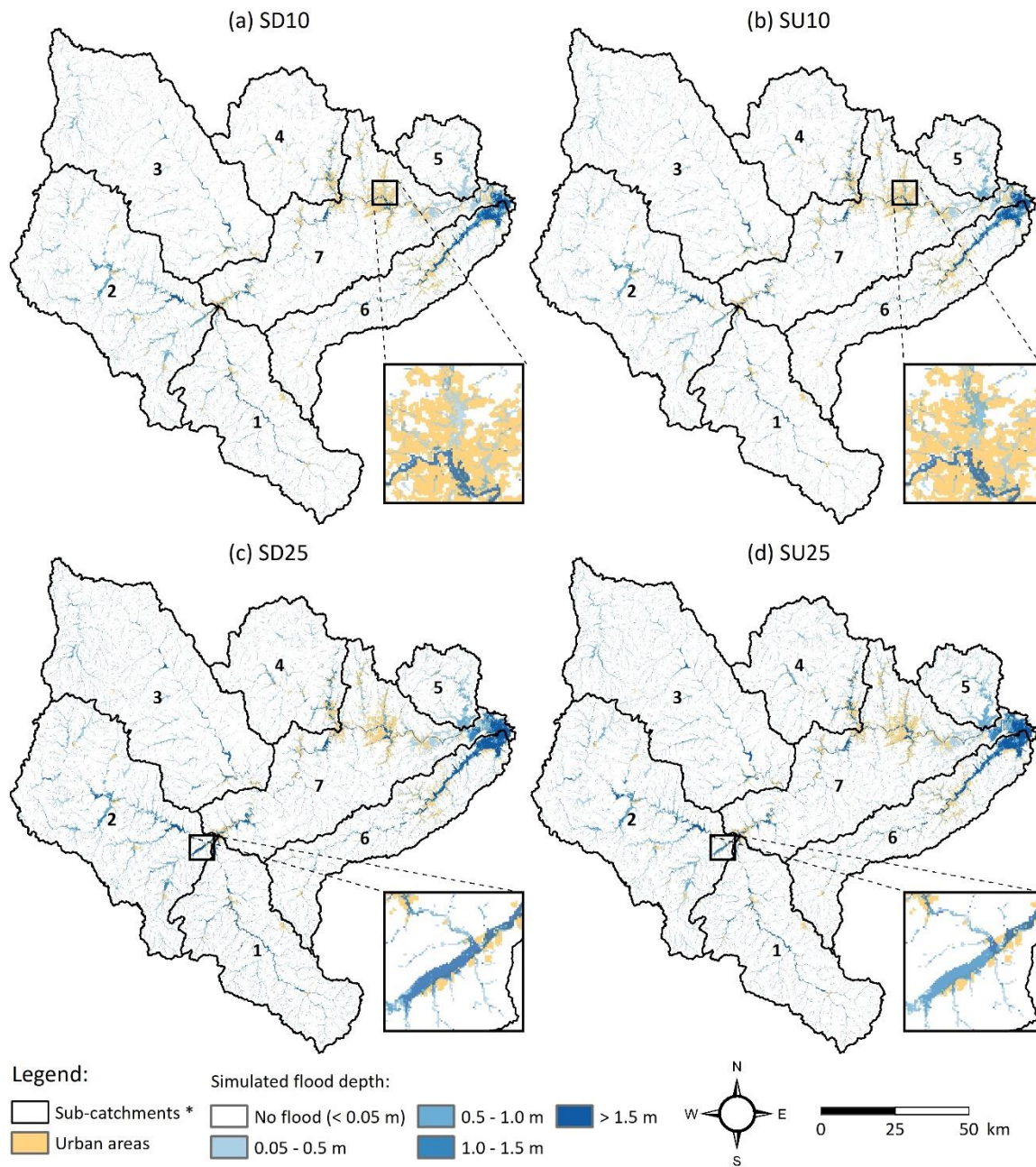
Figure 26: Simulated flood depths for the scenarios of spatially distributed (a, c) and uniform (b, d) design storms, for the return periods of 10 (a, b) and 25 (c, d) years. The small squares highlight locations with differences in flood depth between spatially distributed and uniform rainfall.

It is possible to observe that most of the flooded areas are concentrated near the outlet of the Itajaí-Açu river basin, in the sub-catchments of Itajaí-Açu (7) and Itajaí-Mirim (6). These areas are also coincident with the location of the cities of Itajaí, Navegantes, and Brusque (see Figure 1), which are among the most populous in the region. To further understand the distribution of flood hazard in the study area, Figure 27 presents the quantification of the flooded area in the sub-catchments for the analyzed return periods of 2 (Figure 27a), 5 (Figure 27b), 10 (Figure 27c), and 25 (Figure 27d) years. The two bars in each sub-catchment refer to the SD (left bar) and SU (right bar) rainfall scenarios. A complete overview of the exact values of flooded areas is presented in Appendix 4.

As observed, the 2-year event is characterized by predominantly shallow floods, of less than 0.5 m, with an increase in the total flooded area and the flood depth in less frequent events. For all return periods, the largest flooded extents were observed in the sub-catchments of Itajaí-Açu (7) and Itajaí do Oeste (2). In this context, it is relevant to mention that the Itajaí-Açu (7) sub-catchment encompasses some of the most populous urban areas in the basin, including the cities of Blumenau, Rio do Sul, and parts of Itajaí and Navegantes (see Figure 1). Large flood extents were also observed in the sub-catchments of Itajaí-Mirim (6) – where Brusque and part of Itajaí are located – and Itajaí do Norte (3). In this context, these four sub-catchment are also the areas that greatly contributed to the total water volume at the main outlet of the basin, as indicated in the previous paragraphers. Regarding the total flooded area in the entire Itajaí-Açu river basin, the values varied from 347.01 km² (SD) and 318.66 km² (SU) for a 2-year event to 1,407.57 km² (SD) and 1,405.95 km² (SU) for a 25-year event.
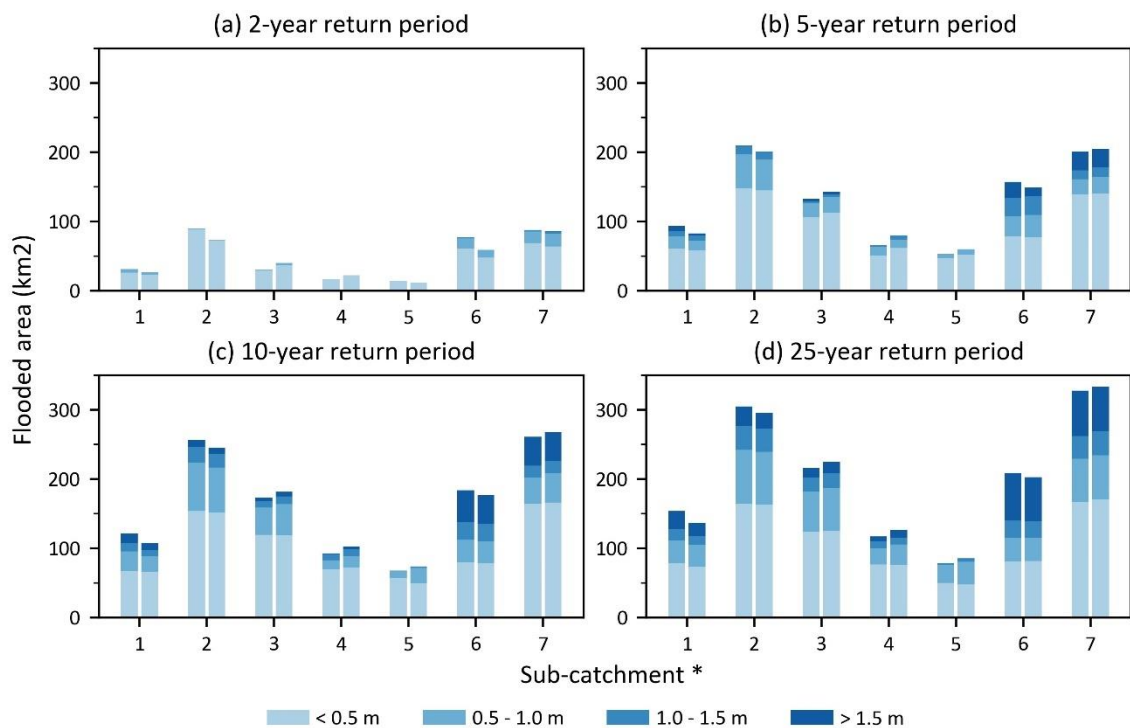
Figure 27: Total flooded area in each sub-catchment for the return periods of 2 (a), 5 (b), 10 (c), and 25 (d) years. The two bars in each sub-catchment indicate the differences between the scenarios of spatially distributed (left bar) and spatially uniform (right bar) design storms.

When comparing the SD and SU scenarios, the total flooded area in the entire basin varied by -8.17% (28.34 km²), 1.00% (9.11 km²), -0.10% (1.17 km²), and -0.11% (1.61 km²) for return periods of 2, 5, 10, and 25 years, respectively. This variation was even more expressive when analyzing each sub-catchment individually. In the case of the 25-year event, the highest variations were observed in the Itajaí do Sul (1)

and Benedito (4) sub-catchments, with differences of -11.15% (17.15 km²) and 8.46% (9.89 km²), respectively. When analyzing all return periods, the highest variation was observed in the Itajaí do Norte (3) sub-catchment for a 2-year event, with an overestimation of the flooded area by the SU scenario of 34.46% (10.23 km²). Another relevant aspect refers to the classes of flood depth. Except for the 2-year event, for all other return periods, the SU scenario resulted in a lower extent of floods deeper than 1.5 m. The differences were of -24.47% (15.28 km²), -5.36% (6.42 km²), and -5.27% (11.03 km²) for 5, 10, and 25 years, respectively. These results highlight a significant underestimation of the extent of deep floods when adopting spatially uniform (SU) rather than spatially distributed (SD) design storms. The percentual variations were even more expressive when analyzing a particular flood depth class in each sub-catchment. The highest variation was observed for a 2-year event in the Itajaí do Norte (3) sub-catchment, where the SU scenario overestimated floods between 0.5 and 1.0 m by 430.90% (2.37 km²). With the increase in the return periods, the variations seemed to be less sensitive to the rainfall scenarios. However, the differences were still significant. As an example, the highest variation for a 25-year event was in the Benedito (4) sub-catchment, with an overestimation of 85.81% (1.82 km²) in floods between 1.0 and 1.5 m.

4.5.2   Flood exposure

To understand the influence of the SD and SU rainfall scenarios on the quantification of exposure, the previously obtained flood depth maps (Figure 25 and Figure 26) were intersected with the land use class *urban infrastructure* to obtain exposure. Figure 28 demonstrates the distribution of the exposed urban areas among the sub-catchments for return periods of 2 (Figure 28a), 5 (Figure 28b), 10 (Figure 28c), and 25 (Figure 28d) years. The two bars in each sub-catchment refer to the scenarios of spatially distributed (left bar) and spatially uniform (right bar) design storms. A complete overview of the exact values of the exposed urban area is presented in Appendix 5.

* 1. Itajaí do Sul | 2. Itajaí do Oeste | 3. Itajaí do Norte | 4. Benedito | 5. Luiz Alves | 6. Itajaí-Mirim | 7. Itajaí-Açu
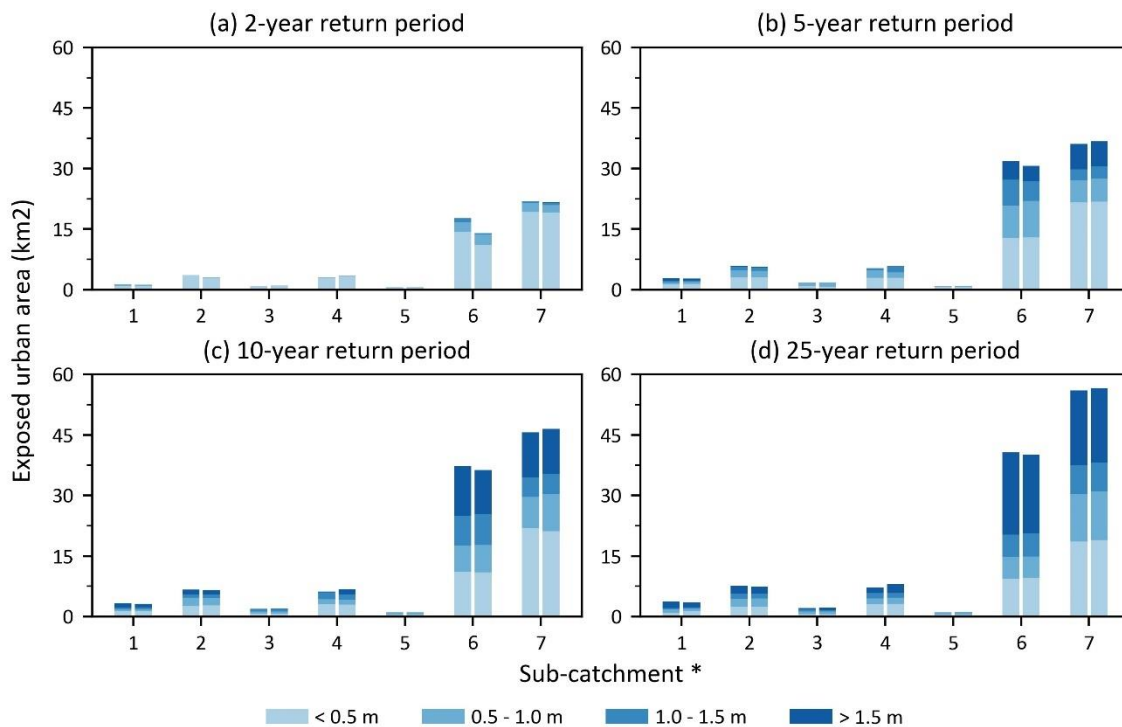
Figure 28: Total exposed urban area in each sub-catchment for the return periods of 2 (a), 5 (b), 10 (c), and 25 (d) years. The two bars in each sub-catchment indicate the differences between the scenarios of spatially distributed (left bar) and spatially uniform (right bar) design storms.

One aspect that stands out is the clear difference in the distribution of exposed urban areas throughout the sub-catchments when compared with the flood hazard analysis in Figure 27. In the case of flood exposure, the Itajaí-Açu (7) and Itajaí-Mirim (6) sub-catchments concentrated at least 80% of the total exposed urban area in the basin, regardless of the rainfall scenario and return period. In its turn, the Itajaí do Oeste (2) and Itajaí do Norte (3) sub-catchments presented very low values of exposed urban area, in contrast with the large extension of the flooded areas (see Figure 27). In addition, the exposed area significantly increased when adopting higher return periods, as expected. The total exposed urban area in the Itajaí-Açu river basin ranged from 49.22 km² (SD) and 44.95 km² (SU) for a 2-year event to 118.60 km² (SD) and 119.02 km² (SU) for a 25-year event. This increase was also accompanied by an increase in the areas exposed to deeper floods. While shallow floods below 0.5 m represented more than 86.5% (SD) and 86.8% (SU) of the total exposed urban area for a 2-year event, this percentage decreased to 29.8% (SD) and 29.9% (SU) for a 25-year event. This expressive decrease was followed by an increase in the percentage of urban areas exposed to floods deeper than 1.5 m, reaching a total of 37.4% (SD) and 36.5% (SU) for a 25-year event.

Regarding the comparison between rainfall scenarios, SU once again underestimated the urban areas exposed to floods deeper than 1.5 m, except in the case of a return period of 2 years. The underestimation was about -8.87% (1.05 km²), -2.49% (0.65 km²), and -1.91% (0.85 km²) for return periods of 5, 10, and 25 years, respectively. However, the 2-year event presented the highest difference in the total exposed area, with a variation between the SU and SD scenarios of -8.65% (4.26 km²) in the entire basin. This variation was mostly caused by an underestimation of -3.71 km² in the Itajaí-Mirim sub-catchment (6). In the case of higher return periods, the quantification of the exposed urban area seemed to be less sensitive to the adopted rainfall scenario, ranging from ±0% to 10% depending on the analyzed sub-catchment, and from ±0% to 0.35% in the entire basin. In this case, the difference between scenarios was more significant when analyzing the variations among flood depth classes. The highest variation among all return periods was observed for a 25-year event in the Luiz Alves (5) sub-catchment, with an underestimation of 321.65% (11.34 km²) of the urban areas exposed to floods between 1.0 and 1.5 m. Equally expressive variations of more than ±140% were also observed in all the other return periods when analyzing a specific flood depth class in a specific sub-catchment.

5   DISCUSSION

This study aimed to investigate to which extent the quantification of flood hazard and exposure is sensitive to the adoption of spatially distributed design storms when compared with the commonly adopted spatially uniform rainfall. One of the strengths of the research was the validation of the rainfall products, including gauge, satellite, and merged satellite-gauge rainfall estimates. The evaluation of multiple products for three temporal scales and different intensity classes provided a complete comparative analysis of their opportunities and limitations. In addition, the method also enabled the comparison of two satellite-derived products (GSMaP and IMERG) and merging techniques (MBC and RIDW), and two timesteps (3-daily and monthly) for each technique. Another strength was the settling of the OpenLISEM hydrological model. The construction of the model involved the collection of multiple secondary data from open sources, both global and from Brazil. The process of data integration brought several opportunities and challenges, which required the definition of assumptions and methodological approaches, as demonstrated throughout the text. This dynamic decision-making process contributed to a stronger familiarization with the study area, which is essential in disaster risk research. It also enabled the testing of the applicability of these data sources (e.g. SoilGrids, MapBiomas, DTM) in hydrological modelling. As a result, this process generated an accurate calibration of the model, although with limitations in the estimation of the flood extent. But improvements can be made, and complete validation of the model with other flood events would significantly support the validity of the research results.

On the other hand, a weakness of the research was the evaluation of the sensitivity of flood hazard and exposure to the rainfall scenarios. The visualization of the IDF curves indeed enabled a critical analysis of how the spatial rainfall variability influenced the generation of the design storms in the study area. Also, the analysis of flood peak discharge, total water volume, flooded area, and exposed urban allowed an overall assessment of the impacts of the spatial rainfall variability on hydrological simulations. In this sense, this research contributed to a further understating of the importance of the space-time structure of rainfall in risk research. However, sub-objective 4 was too broad and ambitious. The presented results had so many scales and locations to be analyzed, that more specific research questions would be required to better focus on a research problem. Therefore, the discussions on the sensitivity of flood hazard and exposure seemed vague and, to a certain extent, inconclusive. In this case, the research could be improved by narrowing down the analysis. This could include, for example, a more detailed evaluation of the satellite-derived rainfall products and resampling techniques, or local analysis of flood hazard and exposure in a specific urban area or section of the river (e.g. focusing on the municipality of Blumenau, where historical flood maps and a telemetric steam gauge are available).

The following subchapters present the main findings of the research sub-objectives, with a critical analysis of the limitations, lessons learned, possible improvements, and a connection with the relevant literature. References are used throughout the text to connect the discussion with its corresponding subchapter of results.

5.1   Sub-objective 1: analysis of rainfall products

The validation of the rainfall products (see Chapters 4.2.1 and 4.2.2) indicated a significant improvement of the KGE values of the satellite products when moving from daily to 3-daily totals. This finding adds to previous observations of temporal mismatches of the satellite-derived rainfall estimates, as described by Beck et al. (2017). In this sense, the aggregation of satellite data into 3-daily totals possibly smoothed out these mismatches, resulting in a better correlation with ground measurements. Because of this low

performance for daily totals, the gauge-based IDW product overperformed all the satellite and satellite-gauge products in this temporal scale. This performance was already expected given that the IDW product was generated through the spatial interpolation of daily gauge measurements. Therefore, the uncertainties of IDW are possibly more associated with the spatial representation of rainfall rather than temporal mismatches. The effects of these spatial uncertainties were demonstrated by the size of the interquartile range of the boxplots in Figure 8 and the high spatial variability of the KGE values in Figure 10.

Regarding the differences between the satellite sources, the results indicated better performance of GSMaP-derived when compared with the IMERG-derived products. As visualized in Figure 8, this difference was mostly explained by a higher linear correlation (r) with the ground observations, thus demonstrating that GSMaP represents more accurately the temporal dynamics of the rainfall time series. In this sense, Rozante, Vila, Chiquetto, Fernandes, & Alvim (2018) compared GSMaP and IMERG daily estimates over southern Brazil, and also identified a better performance of GSMaP, which presented lower values of root mean square error (RMSE) and mean squared error (MSE). In addition, the GSMaP-derived products also proved to have better performance (KGE) for rainfall intensities over the 70th percentile, as demonstrated in Figure 11. However, an observed limitation of the GOr product was its overall tendency to underestimate intensities, as previously highlighted by Rozante et al. (2018). In the case of rainfall intensities over the 90th percentile, both the GOr and IOr products significantly underestimated the rainfall intensities, thus highlighting the limited capacity of the original satellite-derived estimates to capture extremes. This tendency of satellite products to underestimate rainfall extremes was previously demonstrated in studies conducted in China (A. Zhang et al., 2019) and Brazil (Palharini et al., 2020).

In this context, the adoption of merged satellite-gauge products seems promising. The analysis of 3-daily totals indicated a better performance (KGE) of both GM3 and GR3 when compared with IDW, and a lower β when compared with the IMERG-derived products. These results highlighted the high potential of the merging techniques to improve the accuracy and decrease the bias of the original satellite-derived estimates, particularly in the case of GSMaP. This indicates the applicability of these products in hydrological studies, with the advantages of an hourly temporal resolution and continuous spatial coverage when compared with IDW. On the other hand, all merging techniques improved the spatial variability of the calculated indices, as visualized in Figure 8, Figure 9, and Figure 10. This might be explained by the location of the source rain gauges, given that the worst values of (KGE) were observed in the north of the basin, far from the source gauges. Therefore, this research added to previous literature that indicated the high importance of the gauge network density to generate accurate and spatially consistent satellite-gauge rainfall estimates (Dinku et al., 2014; Manz et al., 2016; Woldemeskel et al., 2013).

Regarding the merging techniques, a comparison between MBC and RIDW highlighted very similar improvements for the GSMaP-derived products. On the other hand, the MBC technique seemed to be ineffective to correct the IMERG estimates, as demonstrated by the high spatial variability of the calculated indices in the case of the IM3 product (see Figure 8 and Figure 10). This variability might be explained by the multiplicative nature of MBC. The multiplicative correction factor is sensitive to low rainfall intensities, as it is calculated as the ratio between the gauge and satellite estimates. Therefore, the existence of low satellite estimates can result in extremely high correction factors, producing unrealistic rainfall values. RIDW is not sensitive to these factors because a differential correction factor is adopted instead. Another possible explanation is the adoption of a uniform factor in the MBC technique. While RIDW performs a spatial interpolation of the correction factors, MBC assumes a uniform correction factor for the entire basin. This might produce inaccurate estimates for rainfall events with high spatial variability, especially considering the uneven spatial distribution of the rain gauges from Group 1. In this context, Nerini et al. (2015) also identified a better performance of non-parametric techniques that account for the spatial variability of the

correction factors. This limitation of the uniformity of MBC is exacerbated in large areas with complex topography and climate, which often present high spatial rainfall variability (Nerini et al., 2015). In this case, this research indicated that the RIDW technique seems to be a more stable and robust option to merge satellite and gauge rainfall data.

Overall, the validation process provided an extensive assessment of the analyzed rainfall products for three temporal scales, thus building on the understanding of their strengths and limitations. Apart from an overall statistical evaluation of the different rainfall sources (Beck et al., 2017; Palharini et al., 2020; Rozante et al., 2018; Q. Sun et al., 2018; A. Zhang et al., 2019) and merging techniques (Dinku et al., 2014; Nerini et al., 2015), this study also presented a more in-depth analysis of the products. This includes a spatial evaluation of the errors and a validation of the products per rainfall intensity class. Therefore, this study combined the potential of the KGE index (Baez-Villanueva et al., 2018) with a discretization of the space-time structure and intensity of the rainfall events. The results presented in Figure 8 to Figure 11 can be adopted as a baseline to select a rainfall data source over the Itajaí-Açu river basin for a specific hydrological application. In addition, while the performance of the satellite products significantly varies across the globe (Beck et al., 2017), the methods described in Chapters 3.2 to 3.5 can be replicated to evaluate the rainfall products in another location. On the other hand, the proposed method also presented limitations, as the point-to-pixel approach that was adopted in the analysis. Satellite products represent an areal distribution of rainfall, typically presenting a lower mean and variance when compared with point rainfall (Ombadi, Nguyen, Sorooshian, & Hsu, 2018). Therefore, the adoption of methods to downscale the satellite-derived estimates to finer resolutions, as in Zorzetto & Marani (2019), could provide improved rainfall estimates, adding to the proven potential of the merging techniques.

5.2   Sub-objective 2: representation of spatial rainfall variability

This study proposed a framework to generate spatially distributed design storms from satellite-derived rainfall estimates to represent the spatial rainfall variability over large catchment areas. The framework involved the estimation of IDF curves for each pixel of the satellite image. This resulted in a total of 195 hyetographs representing a single design storm, and a total of four design storms for return periods of 2, 5, 10, and 25 years (see Chapter 4.3).

On one hand, the proposed framework provided an opportunity to investigate the effects of spatial rainfall variability on frequency analysis. The results indicated that the assumption of spatially distributed rainfall significantly influenced the generation of IDF curves (see Figure 14) and design storms (Figure 15 to Figure 18) for the Itajaí-Açu river basin. In the case of IDF curves, a high difference between the minimum and maximum values among the analyzed pixels highlighted a significant spatial variability of the rainfall events. This variability was even higher for shorter durations, which might be influenced by higher uncertainties when fitting the Gumbel distribution, as demonstrated in Figure 12. In this sense, this study supported previous studies (Marra et al., 2017; Noor et al., 2021) that indicated the potential of satellite-derived rainfall products for the generation of IDF curves. This potential is even more expressive in the case of sparse gauge networks, given the limitations of gauge interpolation methods to represent the spatial rainfall variability, as discussed in Chapter 5.1.

On the other hand, several data and methodological limitations were identified. First, Marra et al. (2017), Noor et al., (2021), and Ombadi, Nguyen, Sorooshian, & Hsu (2018) demonstrated that satellite-derived IDF curves are often inaccurate, given that satellite estimates tend to underestimate rainfall extremes. In this case, a comparison between satellite- and gauge-derived IDF curves would be important to validate the results of this research. However, the absence of rain gauges with long records of hourly measurements impaired the validation in this specific case study area. In addition, satellite products represent the areal

distribution of rainfall, as already mentioned in Chapter 5.1. Therefore, a method to convert these averaged rainfall amounts to a point location would be recommended to validate the IDF curves against ground observations. Finally, Ombadi et al. (2018) highlighted that the adoption of merging techniques can significantly improve the accuracy of satellite-derived IDF curves when compared with the original estimates. In this sense, the application of the RIDW merging technique would possibly result in less biased design storms, if a denser gauge network was available.

5.3   Sub-objective 3: setting up of hydrological model

This study settled an OpenLISEM hydrological model schematization of the Itajaí-Açu river basin through the adoption of open-source datasets, as presented in Chapters 3.1 and 3.7. The 2013 flood was adopted to calibrate the model (see Chapter 4.4) because of the availability of discharge measurements at 15-minute intervals during the event. The calibrated Manning's coefficient of 0.055 for the entire channel was considered realistic to represent the study area, according to the recommendation of Chow (1959) and the conditions of the riverbed, as illustrated in Figure 21. An obtained NSE of 0.97 added to previous studies that demonstrated the potential of the model to simulate flash floods and riverine floods (Baartman, Jetten, Ritsema, & de Vente, 2012; Bout & Jetten, 2018). This is particularly relevant considering the scale of the analysis – of more than 15,000 km² – as the performance of the model in such a large catchment has not been fully explored in previous research. In addition, the good performance highlighted the applicability of the model despite the coarse spatial resolution adopted in the analysis. On the other hand, a bias ratio of 0.619 in the GSMaP rainfall estimates during the 2013 flood event is a limitation of this research. Although the model could be effectively calibrated, the adopted initial soil moisture of 79% most probably does not represent the original conditions in 2013, as the calibration aimed to decrease the effects of the bias in the satellite-derived rainfall. These uncertainties in the calibration of the model parameters impaired a robust evaluation of OpenLISEM through validation with other flood events, given that the bias in the satellite estimates is not constant over time. Ideally, simulating multiple historical flood events could improve both the calibration and validation of the model.

Apart from the simulated hydrograph, the simulated flood extent was also compared with the observed event at the location of Blumenau, as presented in Chapter 4.4. The visual inspection of the flood maps demonstrated an overestimation of the simulated extent. In addition, the Kappa coefficient was calculated as 0.49, which indicated a moderate agreement of the model. Although adequate for large-scale analysis, these results highlighted a significant mismatch between the simulated and observed flood extents. Given the excellent performance of the hydrograph calibration, this mismatch might be explained by the coarse spatial resolution of the model, of 100 meters. In this sense, Grohmann (2015) indicated that resampled DTMs – to a coarser spatial resolution – often smooth out important topographic features that control hydrological processes. To further evaluate this limitation, it would be interesting to compare the sensitivity of the model results to different spatial resolutions, as the resolution is an important factor in flood hazard mapping (Goyal et al., 2018; Tan et al., 2018). However, the size of the catchment would demand complex computing solutions, as the adopted 100-meter model took approximately 12 hours to run. An option would be to integrate the discharge time series upstream from Blumenau as a boundary condition in another model with a finer spatial resolution, encompassing only a small extension over the analyzed urban area. While contributing to a more detailed evaluation of the model performance, this integration would make better use of the available DTM, which has an original spatial resolution of 1 meter.

5.4 Sub-objective 4: simulation of rainfall scenarios

As a final step, this research aimed to evaluate the sensitivity of the quantification of flood hazard and exposure to scenarios of spatially distributed (SD) and spatially uniform (SU) rainfall. The results are presented in Chapter 4.5. In an initial analysis, this study investigated the changes in flood peak discharge and total water volume at the outlets of the main sub-catchments of the Itajaí-Açu river basin. The results demonstrated an expected association between the variations in these parameters and the spatial distribution of the generated design storms, as presented in Figure 15 Figure 18. In this context, while the SU scenarios overestimated peak discharge and total water volume at the outlets of the sub-catchments in the north (Itajaí do Norte, Benedito, Luiz Alves), they underestimated these parameters at the outlets of the sub-catchments in the south (Itajaí do Sul, Itajaí do Oeste, Itajaí-Mirim). The variations ranged from ±0% to 23.76% for the peak discharge and from ±0% to 20.74% for the total water volume. These values were significantly lower than the findings of Arnaud et al. (2002), who identified variations of up to 80% in peak discharge and 30% in total water volume when comparing scenarios of spatially distributed and uniform rainfall. Two factors might be associated with these differences. First, Arnaud et al. (2002) modelled catchment areas from 20 to 1,500 km², which are more than ten times smaller than the case study area. In this context, Peleg et al. (2017) highlighted the expected differences in the sensitivity of hydrological simulations to the spatial rainfall variability when comparing low- and middle-sized with large-sized catchments. Second, Arnaud et al. (2002) did not consider design storms in the analysis but adopted 50 historical rainfall events. Real rainfall events are often concentrated over a specific region, especially in the case of large catchments with localized rainfall. This was the case of the 2013 rainfall event analyzed in this research, as illustrated in Figure 20. During the event, the difference between the driest and wettest pixels was 60 mm, thus highlighting a higher spatial variability when compared with the generated design storms (see Figures Figure 15 to Figure 18). Another factor that might have influenced the low variations in the hydrological parameters is the proven role of the natural floodplains in attenuating riverine floods in the Itajaí-Açu river basin, as investigated by Fleischmann et al. (2019). These floodplains store large amounts of water, regulating the discharges and possibly decreasing the differences between the hydrographs from both rainfall scenarios.

The sensitivity of the simulations was also evaluated in terms of the flooded area, per sub-catchment and flood depth class. Although the results indicated a considerable variation in the flooded area when comparing the SU and SD scenarios, of almost 35% depending on the analyzed sub-catchment, the highest variations were observed when evaluating a specific flood depth class. In this case, changes in the rainfall scenario resulted in differences of more than 400% depending on the sub-catchment, return period, and flood depth. These observations indicated that the water levels are more sensitive than the extension of flood areas. This might be explained by the mountainous topography of the basin (see Figure 2), with narrow valley bottoms confined by steep slopes. In addition, the SU scenarios underestimated floods deeper than 1.5 m for 5-, 10-, and 25-year events. This demonstrated the importance of considering the spatial rainfall variability in flood risk research, especially for higher return periods, given that the vulnerability component is often calculated as a factor of the flood depth (van Westen et al., 2013). Overall, it was notable that the quantification of flood hazard was little sensitive to the assumption of spatial rainfall variability when analyzing the total flooded area in the Itajaí-Açu river basin. However, significant variations in the flood extent and depth when evaluating each sub-catchment individually highlighted large sensitivities that would not have been captured in a large-scale analysis of the entire basin.

Finally, the sensitivity of the simulations to the rainfall scenarios was evaluated in terms of the exposed urban area, per sub-catchment and flood depth class. It was observed that more than 80% of the exposed urban area is in the sub-catchments of Itajaí-Mirim and Itajaí-Açu, regardless of the return period. This high concentration is explained by the location of the most populous cities in the basin, including Itajaí,

Navegantes, Blumenau, and Brusque, as illustrated in Figure 1. In the entire basin, the SD simulations indicated an exposed urban area of 49.22 km² for a 2-year event, which increased to 118.60 km² for a 25-year event. The high extension of exposed areas – even for a return period of 2 years – supported the discussions presented by de Paula et al. (2014) and Espíndola & Nodari (2013), who highlighted the high concentration of urban settlements in the valley bottoms and floodplains in the basin. However, the hazard maps presented in this research were possibly influenced by the low spatial resolution of the model. The coarse resolution affected the delineation of the river network, especially in floodplains, as demonstrated in Figure 19. In this context, the accuracy of the flood extent estimations is questionable at the location of floodplains, as in the case of the cities of Itajaí and Navegantes (see Figure 19e). In addition, it was observed that several hard-engineering projects were executed at the location of the cities, including the construction of drainage systems and the enlargements of canals. In this case, to properly represent this structure and produce more accurate flood maps in the region, a finer spatial resolution would be required, as demonstrated by the low Kappa coefficient of 0.49 during the validation of the simulated flood extent for the 2013 event (see Chapter 4.4.3).

In any case, this research enabled a large-scale evaluation of changes in flood exposure due to spatial rainfall variability. The flood exposure quantification proved to be less sensitive to the rainfall scenarios when compared with flood hazard. The variations in the exposed urban area in each sub-catchment were up to 10% for exposure against 35% for hazard. When comparing specific flood depth classes, a maximum variation of 321.65% was obtained for floods between 1.0 and 1.5 m in the Luiz Alves (5) sub-catchment, when considering a 25-year event. This value was lower than the variation in flood hazard, of more than 400% depending on the sub-catchment and return period. This reduced sensitivity of flood exposure might be explained by the location of the urban areas. On the other hand, the analysis of flood exposure also demonstrated that the SU scenarios underestimated floods deeper than 1.5 m for return periods of 5, 10, and 25 years. Therefore, considering the complexity and the several dimensions of this analysis, a site-specific evaluation is highly recommended for a more detailed understanding of the problem.

6   CONCLUSION AND RECOMMENDATIONS

This study proposed an evaluation of the sensitivity of the quantification of flood hazard and exposure to the assumption of spatial rainfall variability. To perform this analysis, the Itajaí-Açu river basin was selected as a case study area, a catchment of more than 15,000 km² located in southern Brazil. The methodology involved the validation of 11 gauge, satellite, and merged satellite-gauge rainfall products, which were compared to select the most accurate representation of the space-time structure of rainfall. The selected product was then adopted to generate scenarios of spatially distributed and spatially uniform design storms. These two rainfall scenarios were further simulated in a calibrated OpenLISEM model for different return periods. The results were compared in terms of the differences in flood peak intensity, total runoff volume, flooded area, and exposed urban area.

Initially, as part of sub-objective 1, this study presented two well-documented merging techniques with the potential to integrate the accuracy of the rain gauge observations with the space-time structure of the satellite-derived rainfall estimates: mean bias correction (MBC) and residual inverse distance weighting (RIDW). These techniques were compared with the original satellite products (GSMaP and IMERG) and the IDW interpolation of the gauge measurements. The validation demonstrated a high potential of the merging techniques to improve the accuracy of satellite rainfall when adopting 3-daily timesteps. The best performance was obtained with RIDW, which proved to be more robust and stable, particularly for IMERG estimates. In its turn, GSMaP proved to be more accurate than IMERG to represent rainfall over the Itajaí-Açu river basin, despite its stronger tendency to underestimate intensities. This tendency to underestimation effectively decreased with the application of the RIDW technique. In this context, the GR3 product presented the best results for 3-daily and monthly totals among all products, overperforming the gauge-based IDW. On the other hand, the merging techniques intensified the uncertainties in the spatial representation of the rainfall events, as demonstrated by a higher spatial variability among the calculated statistical parameters. For this reason, the original GSMaP product (GOr) was adopted as a rainfall input in the methodology, as this research focuses on the representation of the spatial rainfall variability. However, the adoption of the GR3 product for hydrological studies in the basin is still highly recommended.

As a further step, a framework was developed to generate design storms representing the spatial rainfall variability, as defined by sub-objective 2. The proposed framework encompassed the definition of intensity-duration-frequency (IDF) curves for each pixel of the rainfall product, resulting in a total of 195 curves. This number refers to the number of pixels of the adopted GSMaP product that intersect the case study area. The generation of IDF curves highlighted a high variability among the pixels, with large intervals between the minimum and maximum values, especially for shorter durations. These results demonstrated the high influence of spatial rainfall variability on the estimation of IDF curves and design storms. As an example, for a duration of 1 hour, a rainfall intensity of 12 mm/h can represent both a 5- and a 25-year event in different pixels over the basin. The IDF curves were later adopted to generated design storms with a 24-hour duration based on the alternating block method, resulting in a time series of rainfall maps. The design storms were generated for return periods of 2, 5, 10, and 25 years. To explore the impacts of the rainfall variability on flood hazard and exposure, two scenarios of rainfall were generated: spatially distributed (SD) and spatially uniform (SU) design storms. While the first represented the original rainfall maps with a different hyetograph at each pixel location, the second was generated by calculating the mean rainfall intensity over the study area.

Following the generation of the design storms, an OpenLISEM hydrological model of the Itajaí-Açu river basin was settled as part of sub-objective 3. The model was calibrated with the 2013 flood event. The event

had a total duration 1,920 minutes, with an average peak intensity of 6.73 mm/h and an average total rainfall volume of 85.36 mm. The highest rainfall amounts were observed upstream, concentrated mostly over the Itajaí do Oeste and Itajaí do Norte sub-catchments. The analysis of the simulations against discharge measurements demonstrated the excellent performance of the calibrated model. The NSE was calculated as 0.97, with an error in flood peak intensity and total water volume of 0.30% and -1.74%, respectively. Spatial validation of the model was also performed through the comparison of the simulations with historical flood maps in Blumenau. The validation resulted in a Kappa coefficient of 0.49, considered a moderate agreement, with an overestimation of the simulated flood extent. Therefore, despite the outstanding performance of the hydrological simulation, the model did not accurately represent the flood extent. This was possibly caused by the coarse spatial resolution of the model, of 100 meters.

As a final step, sub-objective 4 addressed the sensitivity of the flood hazard and exposure estimations to the SD and SU rainfall scenarios. An initial analysis evaluated the differences in flood peak discharge and total water volume between the rainfall scenarios. The results indicated an association of the percentual differences with the spatial pattern of the design storms, with higher values for the SD scenarios over the sub-catchments in the south, higher values for the SU scenarios over the north. The analysis of the discharge amounts also enabled visualization of the sub-catchments that contributed the most to the total water volume at the outlet, which is important to understand where interventions are needed. The four most considerable contributions were observed at the outlets of the Itajaí do Oeste, Itajaí do Norte, Itajaí-Mirim, and Itajaí-Açu sub-catchments, with percentages ranging from 14.83% to 22.67% of the total water volume depending on the sub-catchment and the analyzed return period. These sub-catchments also presented the largest flooded areas, regardless of the return period. On the other hand, the largest exposed urban areas were observed only in the Itajaí-Açu and Itajaí-Mirim sub-catchments, which might be explained by the large concentration of cities in the region, including Itajaí, Navegantes, Blumenau, and Brusque. Finally, the analysis between rainfall scenarios demonstrated that the quantification of flood hazard and exposure can be sensitive to the adopted rainfall pattern, with variations in the flooded area ranging from $\pm 0\%$ to 35% depending on the sub-catchment. Differences in flood depths demonstrated to be even more sensitive to the rainfall scenarios, with variations of more than 400% depending on the sub-catchment and the return period. This might be explained by the mountainous topography in most of the basin, which confines the extension of the flooded areas along the valley bottoms. Overall, the results were highly dependent on the specific location in the basin, the flood depth class, and the return period. Therefore, a more detailed study in a specific location would be highly recommended.

6.1   Recommendations

This research addressed specific questions and objectives. In this process, several other questions could be identified, which brought new perspectives for future studies. To conclude this report, some of these perspectives are summarized in the following recommendations:

- For the rainfall validation, more satellite-derived rainfall products and merging techniques could be included in the analysis, thus providing a more complete assessment of the rainfall data sources.
- Depending on the availability and density of the gauge network, cross-validation could be performed in the bias correction and the validation of the satellite estimates. This could help to understand the spatial performance of the merging techniques as a function of the distance from the source rain gauges. In any case, cross-validation could improve the robustness of the estimated statistical parameters.
- To support hydrological studies, the methodology and the scripts could be automatized to perform a validation of gauge, satellite, and merged satellite-gauge rainfall products in any study area within the

Brazilian territory. This would demand the integration of the Google Earth Engine platform and the HidroWeb portal to combine satellite and gauge rainfall data.

- For the IDF curves, validation could be performed through the comparison of satellite- and gauge-derived curves. This could support the discussion on the applicability of satellite-derived products in extreme value statistics in the study area.

- For the hydrological modelling, other flood events could be included in the analysis to validate the hydrological parameters adopted in the calibration of the OpenLISEM model.

- In addition, the sensitivity of the model results to the spatial resolution of the DTM could be tested, including flood extent and hydrograph.

- For the quantification of flood hazard and exposure, a more local analysis could be performed in a specific urban area. The Municipality of Blumenau would be a great option because of the availability of historical flood maps and discharge measurements to calibrate and validate the hydrological model.

LIST OF REFERENCES

AlertaBlu. (2020). Enchentes registradas Blumenau [Registered river floods Blumenau]. Retrieved September 28, 2020, from http://alertablu.cob.sc.gov.br/p/enchentes

Amorim, J. da S., Viola, M. R., Junqueira, R., de Oliveira, V. A., & de Mello, C. R. (2020). Evaluation of satellite precipitation products for hydrological modeling in the Brazilian Cerrado biome. *Water (Switzerland)*, *12*(9). https://doi.org/10.3390/W12092571

ANA. (n.d.). Portal HidroWeb [HidroWeb Portal]. Retrieved May 23, 2021, from https://www.snirh.gov.br/hidroweb/apresentacao

ANA. (2019). Base hidrográfica ottocodificada multiescalas de bacias do Atlântico Sul e Sudeste [Multi-scale ottocodified hydrographic database of the South and Southeast Atlantic basins]. Retrieved May 17, 2021, from https://metadados.snirh.gov.br/geonetwork/srv/search?keyword=Ottobacia

Arnaud, P., Bouvier, C., Cisneros, L., & Dominguez, R. (2002). Influence of rainfall spatial variability on flood prediction. *Journal of Hydrology*, *260*(1–4), 216–230. https://doi.org/10.1016/S0022-1694(01)00611-4

Baartman, J. E. M., Jetten, V. G., Ritsema, C. J., & de Vente, J. (2012). Exploring effects of rainfall intensity and duration on soil erosion at the catchment scale using openLISEM: Prado catchment, SE Spain. *Hydrological Processes*, *26*(7), 1034–1049. https://doi.org/10.1002/hyp.8196

Baez-Villanueva, O. M., Zambrano-Bigiarini, M., Ribbe, L., Nauditt, A., Giraldo-Osorio, J. D., & Thinh, N. X. (2018). Temporal and spatial evaluation of satellite rainfall estimates over different regions in Latin-America. *Atmospheric Research*, *213*(May), 34–50. https://doi.org/10.1016/j.atmosres.2018.05.011

Bárdossy, A., & Das, T. (2008). Influence of rainfall observation network on model calibration and application. *Hydrology and Earth System Sciences*, *12*(1), 77–89. https://doi.org/10.5194/hess-12-77-2008

Beck, H. E., van Dijk, A. I. J. M., de Roo, A., Dutra, E., Fink, G., Orth, R., & Schellekens, J. (2016). Global evaluation of runoff from ten state-of-the-art hydrological models. *Hydrology and Earth System Sciences Discussions*, (May), 1–33. https://doi.org/10.5194/hess-2016-124

Beck, H. E., Vergopolan, N., Pan, M., Levizzani, V., van Dijk, A. I. J. M., Weedon, G. P., … Wood, E. F. (2017). Global-scale evaluation of 22 precipitation datasets using gauge observations and hydrological modeling. *Hydrology and Earth System Sciences*, *21*, 6201–6217. https://doi.org/10.5194/hess-21-6201-2017

Bout, B., & Jetten, V. G. (2018). The validity of flow approximations when simulating catchment-integrated flash floods. *Journal of Hydrology*, *556*, 674–688. https://doi.org/10.1016/j.jhydrol.2017.11.033

CanalRural. (2020). Estudo mapeia as áreas de silvicultura em Santa Catarina [Study maps planted forestry areas in Santa Catarina]. Retrieved June 28, 2021, from https://blogs.canalrural.com.br/florestasa/2020/06/25/estudo-mapeia-areas-silvicultura-sc/?web=1&wdLOR=c5C0E9C5E-D0E5-4032-BD08-2A831C571194

CEPED UFSC. (2013). *Atlas brasileiro de desastres naturais 1991 a 2012 - volume Santa Catarina [Brazilian atlas of natural disasters 1991 to 2012 - volume Santa Catarina]*. Retrieved from http://150.162.127.14:8080/atlas/Atlas Pernambuco.pdf

Chow, V. Te. (1959). *Open-channel hydraulics*. New York: McGraw-Hill Book Company.

Chow, V. Te, Maidment, D. R., & Mays, L. W. (1988). Design storms. In *Applied hydrology* (pp. 466–467). Singapore: McGraw-Hill Book Company.

Cohen, J. (1960). A coefficient of agreement for nominal scales. *Educational and Psychological Measurement*, *20*, 37–46. https://doi.org/10.1177/001316446002000104

Comitê do Itajaí. (2010). Plano de recursos hídricos da bacia do Itajaí: caderno síntese [Water resources plan of the Itajaí basin: synthesis report]. In *Fundação Agência de Água do Vale do Itajaí*. Retrieved from http://www.aguas.sc.gov.br/base-documental-rio-itajai/noticias-rio-itajai/item/download/173_162158b668453a53c5b010ac0aa1f41f

CPRM. (2020). *Atlas pluviométrico do Brasil. Equações intensidade-duração-frequência. Equações definidas em 2020. [Rainfall atlas of Brazil. Intensity-frequency-duration equations. Equations defined in 2020]*. Retrieved from https://rigeo.cprm.gov.br/bitstream/doc/21959/3/equacoes_idf_2020_meta_gdag.pdf

de Paula, S. M., Nodari, E. S., & Espíndola, M. A. (2014). O crescimento urbano e as enchentes em Blumenau (SC) [Urban growth and the floods of Blumenau (Santa Catarina)]. *Revista Do Arquivo Geral Da Cidade Do Rio de Janeiro*, *8*, 201–212. Retrieved from http://wpro.rio.rj.gov.br/revistaagcrj/wp-content/uploads/2016/11/e08_a11.pdf

de Sousa, L., Poggio, L., Batjes, N., Heuvelink, G., Kempen, B., Riberio, E., & Rossiter, D. (2020). SoilGrids 2.0: producing quality-assessed soil information for the globe. *SOIL Discussions*, (November), 1–37. https://doi.org/10.5194/soil-2020-65

Dingman, S. L. (2015a). Principles of subsurface flow. In *Physical hydrology* (Third, pp. 313–344). https://doi.org/10.1177/030913338901300106

Dingman, S. L. (2015b). Runoff generation and streamflow. In *Physical hydrology* (Third, pp. 455–530). https://doi.org/10.1177/0309133389013001906

Dinku, T., Hailemariam, K., Maidment, R., Tarnavsky, E., & Connor, S. (2014). Combined use of satellite estimates and rain gauge observations to generate high-quality historical rainfall time series over Ethiopia. *International Journal of Climatology*, *34*(7), 2489–2504. https://doi.org/10.1002/joc.3855

dos Santos, C. F., Tornquist, C. S., & Marimon, M. P. C. (2014). Indústria das enchentes? Impasses e desafios dos desastres socioambientais no vale do Itajaí [Flood industry? Impasses and challenges of socio-environmental disasters in the Itajai valley]. *Geosul*, *29*(57), 197. https://doi.org/10.5007/25740

Espíndola, M. A., & Nodari, E. S. (2013). Enchentes inesperadas? Vulnerabilidades e políticas públicas em Rio do Sul - SC, Brasil [Unexpected flooding? Vulnerabilities and public policies in Rio do Sul - SC, Brazil]. *Esboços - Revista Do Programa de Pós-Graduação Em História Da UFSC*, *20*(30), 9. https://doi.org/10.5007/2175-7976.2013v20n30p9

Fensterseifer, C., Allasia, D. G., & Paz, A. R. (2016). Assessment of the TRMM 3B42 precipitation product in southern Brazil. *Journal of the American Water Resources Association*, *52*(2), 367–375. https://doi.org/10.1111/1752-1688.12398

Fleischmann, A., Collischonn, W., & Paiva, R. (2018). Integrando reservatórios e planícies de inundação para a simulação de cheias em grandes bacias: aplicação na bacia do rio Itajaí-Açu [Integrating reservoirs and wetlands for flood simulation in large bains: application in the Itajaí-Açu river basin]. *I Encontro Nacional de Desastres*, (July), 1–8. Porto Alegre.

Fleischmann, A., Collischonn, W., Paiva, R., & Tucci, C. E. (2019). Modeling the role of reservoirs versus floodplains on large-scale river hydrodynamics. *Natural Hazards*, *99*(2), 1075–1104. https://doi.org/10.1007/s11069-019-03797-9

Ghanbarpour, M. R., Salimi, S., & Hipel, K. W. (2013). A comparative evaluation of flood mitigation alternatives using GIS-based river hydraulics modelling and multicriteria decision analysis. *Journal of Flood Risk Management*, *6*(4), 319–331. https://doi.org/10.1111/jfr3.12017

Goyal, M. K., Panchariya, V. K., Sharma, A., & Singh, V. (2018). Comparative assessment of SWAT model performance in two distinct catchments under various DEM scenarios of varying resolution, sources and resampling methods. *Water Resources Management*, *32*(2), 805–825. https://doi.org/10.1007/s11269-017-1840-1

Grohmann, C. H. (2015). Effects of spatial resolution on slope and aspect derivation for regional-scale analysis. *Computers and Geosciences*, *77*, 111–117. https://doi.org/10.1016/j.cageo.2015.02.003

Gupta, H. V., Kling, H., Yilmaz, K. K., & Martinez, G. F. (2009). Decomposition of the mean squared error and NSE performance criteria: implications for improving hydrological modelling. *Journal of Hydrology*, *377*(1–2), 80–91. https://doi.org/10.1016/j.jhydrol.2009.08.003

Hessel, R., Jetten, V., & Baoyuan, L. (2003). *Calibration of the LISEM model for a small Loess Plateau catchment*. *54*, 235–254. https://doi.org/10.1016/S0341-8162(03)00067-5

Hsieh, L., Hsu, M., & Li, M. (2006). An assessment of structural measures for flood-prone lowlands with high population density along the Keelung river in Taiwan. *Natural Hazards*, *37*, 133–152. https://doi.org/10.1007/s11069-005-4660-1

IBGE. (2019). BC250 - Base cartográfica contínua 1:250000 [BC250 - Continuous cartographic base 1:250000]. Retrieved May 24, 2021, from https://geoftp.ibge.gov.br/cartas_e_mapas/bases_cartograficas_continuas/bc250/versao2019/

INPE. (2008). TOPODATA. Banco de dados geomorfométricos do Brasil [TOPODATA. Geomorphometric database of Brazil]. Retrieved October 21, 2020, from http://www.webmapit.com.br/inpe/topodata/

IPCC. (2012). *Managing the risks of extreme events and disasters to advance climate change adaptation* (C. B. Field, V. Barros, T. F. Stocker, Q. Dahe, D. Jon Dokken, K. L. Ebi, … P. M. Midgley, Eds.). Retrieved from Cambridge University Press website: https://www.ipcc.ch/site/assets/uploads/2018/03/SREX_Full_Report-1.pdf

Jetten & De Roo. (2018). *OpenLISEM - document & user manual.* Retrieved from https://blog.utwente.nl/lisem/download/

Jetten, V. (2015). *PCRaster script: generation of a LISEM input database.*

Jetten, V. G., & Maneta, M. P. (2011). Calibration of erosion models. In *Handbook of erosion modelling* (pp. 33–51). Blackwell Publishing Ltd.

Jetten, V., & Shrestha, D. P. (2020). *PCRaster script: Saxtons pedotransfer function SWAP model 2005.*

Jongjin, B., Jongmin, P., Dongryeol, R., & Minha, C. (2016). Geospatial blending to improve spatial mapping of precipitation with high spatial resolution by merging satellite-based and ground-based data. *Hydrological Processes*, *30*(16), 2789–2803. https://doi.org/10.1002/hyp.10786

Klonner, C., Marx, S., Usón, T., de Albuquerque, J. P., & Höfle, B. (2016). Volunteered geographic information in natural hazard analysis: a systematic literature review of current approaches with a focus on preparedness and mitigation. *International Journal of Geo-Information*, *5*(103). https://doi.org/10.3390/ijgi5070103

Krvavica, N., & Rubinić, J. (2020). Evaluation of design storms and critical rainfall durations for flood prediction in partially urbanized catchments. *Water (Switzerland)*, *12*(7). https://doi.org/10.3390/w12072044

Lee, J. E., Heo, J. H., Lee, J., & Kim, N. W. (2017). Assessment of flood frequency alteration by dam construction via SWAT simulation. *Water (Switzerland)*, *9*(4), 264. https://doi.org/10.3390/w9040264

Manz, B., Buytaert, W., Zulkafli, Z., Lavado, W., Willems, B., Robles, L. A., & Rodríguez-Sánchez, J. P. (2016). High-resolution satellite-gauge merged precipitation climatologies of the tropical Andes. *Journal of Geophysical Research*, *121*(3), 1190–1207. https://doi.org/10.1002/2015JD023788

MapBiomas. (2020). MapBiomas Brasil coleção 5 (1985-2019) [Mapbiomas Brazil collection 5 (1985-2019)]. Retrieved October 21, 2020, from https://mapbiomas.org/

Marra, F., Morin, E., Peleg, N., Mei, Y., & Anagnostou, E. N. (2017). Intensity-duration-frequency curves from remote sensing rainfall estimates: comparing satellite and weather radar over the eastern Mediterranean. *Hydrology and Earth System Sciences*, *21*(5), 2389–2404. https://doi.org/10.5194/hess-21-2389-2017

Martha, T. R., van Westen, C. J., Kerle, N., Jetten, V., & Vinod Kumar, K. (2013). Landslide hazard and risk assessment using semi-automatically created landslide inventories. *Geomorphology*, *184*, 139–150. https://doi.org/10.1016/j.geomorph.2012.12.001

Mendonça de Moura, J. M. B., Vieira, R., & Bohn, N. (2015). Barragem de contenção de cheias e políticas públicas: o caso de Ituporanga – SC, Brasil [Flood control dams and public policies: the case of Ituporanga – SC, Brazil]. *Sustentabilidade Em Debate*, *6*(3), 70. https://doi.org/10.18472/sustdeb.v6n3.2015.15687

Michaelides, S. (2008). Precipitation: advances in measurement, estimation and prediction. In *Springer*.

Murara, P., Acquaotta, F., Garzena, D., & Fratianni, S. (2019). Daily precipitation extremes and their variations in the Itajaí river basin, Brazil. *Meteorology and Atmospheric Physics*, *131*(4), 1145–1156. https://doi.org/10.1007/s00703-018-0627-0

Nerini, D., Zulkafli, Z., Wang, L. P., Onof, C., Buytaert, W., Lavado-Casimiro, W., & Guyot, J. L. (2015). A comparative analysis of TRMM-rain gauge data merging techniques at the daily time scale for distributed rainfall-runoff modeling applications. *Journal of Hydrometeorology*, *16*(5), 2153–2168. https://doi.org/10.1175/JHM-D-14-0197.1

Noor, M., Ismail, T., Shahid, S., Asaduzzaman, M., & Dewan, A. (2021). Evaluating intensity-duration-frequency (IDF) curves of satellite-based precipitation datasets in Peninsular Malaysia. *Atmospheric Research*, *248*(August 2020), 105203. https://doi.org/10.1016/j.atmosres.2020.105203

Ochoa-Rodriguez, S., Wang, L. P., Gires, A., Pina, R. D., Reinoso-Rondinel, R., Bruni, G., … Ten Veldhuis, M. C. (2015). Impact of spatial and temporal resolution of rainfall inputs on urban hydrodynamic modelling outputs: a multi-catchment investigation. *Journal of Hydrology*, *531*, 389–407. https://doi.org/10.1016/j.jhydrol.2015.05.035

Ombadi, M., Nguyen, P., Sorooshian, S., & Hsu, K. lin. (2018). Developing intensity-duration-frequency (IDF) curves from satellite-based precipitation: methodology and evaluation. *Water Resources Research*, *54*(10), 7752–7766. https://doi.org/10.1029/2018WR022929

Palharini, R. S. A., Vila, D. A., Rodrigues, D. T., Quispe, D. P., Palharini, R. C., de Siqueira, R. A., & de Sousa Afonso, J. M. (2020). Assessment of the extreme precipitation by satellite estimates over South America. *Remote Sensing*, *12*(13), 1–23. https://doi.org/10.3390/rs12132085

Pathiraja, S., Anghileri, D., Burlando, P., Sharma, A., Marshall, L., & Moradkhani, H. (2018). Time-varying parameter models for catchments with land use change: the importance of model structure. *Hydrology and Earth System Sciences*, *22*(5), 2903–2919. https://doi.org/10.5194/hess-22-2903-2018

Peleg, N., Blumensaat, F., Molnar, P., Fatichi, S., & Burlando, P. (2017). Partitioning the impacts of spatial and climatological rainfall variability in urban drainage modeling. *Hydrology and Earth System Sciences*, *21*(3), 1559–1572. https://doi.org/10.5194/hess-21-1559-2017

Peleg, N., Marra, F., Fatichi, S., Paschalis, A., Molnar, P., & Burlando, P. (2018). Spatial variability of extreme rainfall at radar subpixel scale. *Journal of Hydrology*, *556*(October), 922–933. https://doi.org/10.1016/j.jhydrol.2016.05.033

Pérez-Molina, E., Sliuzas, R., Flacke, J., & Jetten, V. (2017). Developing a cellular automata model of urban growth to inform spatial policy for flood mitigation: a case study in Kampala, Uganda. *Computers, Environment and Urban Systems*, *65*, 53–65. https://doi.org/10.1016/j.compenvurbsys.2017.04.013

Pitidis, V., Tapete, D., Coaffee, J., Kapetas, L., & de Albuquerque, J. P. (2018). Understanding the implementation challenges of urban resilience policies: investigating the influence of urban geological risk in Thessaloniki, Greece. *Sustainability (Switzerland)*, *10*(10). https://doi.org/10.3390/su10103573

Pratomo, R. A., Jetten, V., & Alkema, D. (2016). Rural flash-flood behavior in Gouyave watershed, Grenada, Caribbean Island. *Geoplanning: Journal of Geomatics and Planning*, *3*(2), 161. https://doi.org/10.14710/geoplanning.3.2.161-170

Quan Luna, B., Blahut, J., Camera, C., van Westen, C., Apuani, T., Jetten, V., & Sterlacchini, S. (2014). Physically based dynamic run-out modelling for quantitative debris flow risk assessment: a case study in Tresenda, northern Italy. *Environmental Earth Sciences*, *72*(3), 645–661. https://doi.org/10.1007/s12665-013-2986-7

Refice, A., D'Addabbo, A., & Capolongo, D. (2018). Methods, techniques and sensors for precision flood monitoring through remote sensing. In *Flood monitoring through remote sensing* (pp. 1–26).

Rozante, J. R., Vila, D. A., Chiquetto, J. B., Fernandes, A. de A., & Alvim, D. S. (2018). Evaluation of TRMM/GPM blended daily products over Brazil. *Remote Sensing*, *10*(6), 1–17. https://doi.org/10.3390/rs10060882

SDS-SC. (2012). Sistema de Informações Geográficas do Estado de Santa Catarina [Geographic Information System of the State of Santa Catarina]. Retrieved May 23, 2021, from http://sigsc.sc.gov.br/

Shen, J., & Tan, F. (2020). Effects of DEM resolution and resampling technique on building treatment for urban inundation modeling: a case study for the 2016 flooding of the HUST campus in Wuhan. In *Natural Hazards* (Vol. 104). https://doi.org/10.1007/s11069-020-04198-z

Shrestha, B. B., & Kawasaki, A. (2020). Quantitative assessment of flood risk with evaluation of the effectiveness of dam operation for flood control: a case of the Bago river basin of Myanmar. *International Journal of Disaster Risk Reduction*, *50*, 101707. https://doi.org/10.1016/j.ijdrr.2020.101707

Shrestha, D. (2020). What is inverse distance weighting (IDW)? What are its importance in spatial interpolation? How does it work? Retrieved May 25, 2021, from https://dineshrestha83065549.wpcomstaging.com/what-is-inverse-distance-weighting-idw-what-are-

its-importance-in-spatial-interpolation-how-does-it-work/

Smith, T. M., Arkin, P. A., Bates, J. J., & Huffman, G. J. (2006). Estimating bias of satellite-based precipitation estimates. *Journal of Hydrometeorology*, *7*(5), 841–856. https://doi.org/10.1175/JHM524.1

SoilGrids. (2020). SoilGrids 250m 2.0 - global gridded soil information. Retrieved May 23, 2021, from https://soilgrids.org/

Speckhann, G. A., Borges Chaffe, P. L., Fabris Goerl, R., Abreu, J. J. de, & Altamirano Flores, J. A. (2018). Flood hazard mapping in southern Brazil: a combination of flow frequency analysis and the HAND model. *Hydrological Sciences Journal*, *63*(1), 87–100. https://doi.org/10.1080/02626667.2017.1409896

Su, Z., Ho, M., Hao, Z., Lall, U., Sun, X., Chen, X., & Yan, L. (2020). The impact of the Three Gorges Dam on summer streamflow in the Yangtze river basin. *Hydrological Processes*, *34*(3), 705–717. https://doi.org/10.1002/hyp.13619

Sun, Q., Miao, C., Duan, Q., Ashouri, H., Sorooshian, S., & Hsu, K. L. (2018). A review of global precipitation data sets: data sources, estimation, and intercomparisons. *Reviews of Geophysics*, *56*(1), 79–107. https://doi.org/10.1002/2017RG000574

Sun, Y., Wendi, D., Kim, D. E., & Liong, S. Y. (2019). Deriving intensity–duration–frequency (IDF) curves using downscaled in situ rainfall assimilated with remote sensing data. *Geoscience Letters*, *6*(1). https://doi.org/10.1186/s40562-019-0147-x

Tan, M. L., Ficklin, D. L., Dixon, B., Ibrahim, A. L., Yusop, Z., & Chaplot, V. (2015). Impacts of DEM resolution, source, and resampling technique on SWAT-simulated streamflow. *Applied Geography*, *63*, 357–368. https://doi.org/10.1016/j.apgeog.2015.07.014

Tan, M. L., Ramli, H. P., & Tam, T. H. (2018). Effect of DEM resolution, source, resampling technique and area threshold on SWAT outputs. *Water Resources Management*, *32*(14), 4591–4606. https://doi.org/10.1007/s11269-018-2072-8

Tay, L. T., Sagar, B. S. D., & Chuah, H. T. (2005). Analysis of geophysical networks derived from multiscale digital elevation models: a morphological approach. *IEEE Geoscience and Remote Sensing Letters*, *2*(4), 399–403. https://doi.org/10.1109/LGRS.2005.856008

Thomson, D. R., Ku, M., Boo, G., Hati, B., Grippa, T., Elsey, H., … Kabaria, C. (2020). Need for an integrated deprived area "slum" mapping system (IDEAMAPS) in low- and middle-income countries (LMICs). *Social Sciences*, *9*(80), 1–17.

Umer, Y. M., Jetten, V. G., & Ettema, J. (2019). Sensitivity of flood dynamics to different soil information sources in urbanized areas. *Journal of Hydrology*, *577*(July). https://doi.org/10.1016/j.jhydrol.2019.123945

UNDRR. (2015). *Sendai Framework for Disaster Risk Reduction 2015-2030*. Retrieved from https://www.preventionweb.net/files/43291_sendaiframeworkfordrren.pdf

van Westen, C. J., Damen, M., & Feringa, W. (2013). *National scale multi-hazard risk assessment. Theory book. Training package on national scale multi-hazard risk assessment.* https://doi.org/10.13140/RG.2.2.10126.56645

WMO. (2008). Guide to hydrological practices. Volume I. Hydrology - from measurement to hydrological information. In *WMO-No. 168* (Sixth, Vol. 53).

WMO. (2009). Guide to hydrological practices. Volume II. Management of water resources and application of hydrological practices. In *WMO Report No. 168* (Sixth). https://doi.org/10.1080/02626667.2011.546602

WMO. (2018). *Guide to climatological practices*. Geneva.

Woldemeskel, F. M., Sivakumar, B., & Sharma, A. (2013). Merging gauge and satellite rainfall with specification of associated uncertainty across Australia. *Journal of Hydrology*, *499*, 167–176. https://doi.org/10.1016/j.jhydrol.2013.06.039

Wolff, E. (2020). Uncharted terrain: the clash between "risk management" and informal urbanisation. *Urban Transcripts*, *3*(3). Retrieved from http://journal.urbantranscripts.org/article/uncharted-terrain-the-clash-between-risk-management-and-informal-urbanisation-erich-wolff/

Wright, D. B., Mantilla, R., & Peters-Lidard, C. D. (2017). A remote sensing-based tool for assessing rainfall-driven hazards. *Environmental Modelling and Software*, *90*, 34–54.

https://doi.org/10.1016/j.envsoft.2016.12.006

Wu, S., Li, J., & Huang, G. H. (2008). A study on DEM-derived primary topographic attributes for hydrologic applications: sensitivity to elevation data resolution. *Applied Geography*, *28*(3), 210–223. https://doi.org/10.1016/j.apgeog.2008.02.006

Yang, Z., Hsu, K., Sorooshian, S., Xu, X., Braithwaite, D., Zhang, Y., & Verbist, K. M. J. (2017). Merging high-resolution satellite-based precipitation fields and point-scale rain gauge measurements - a case study in Chile. *Journal of Geophysical Research*, *122*(10), 5267–5284. https://doi.org/10.1002/2016JD026177

Zambrano-Bigiarini, M., Nauditt, A., Birkel, C., Verbist, K., & Ribbe, L. (2017). Temporal and spatial evaluation of satellite-based rainfall estimates across the complex topographical and climatic gradients of Chile. *Hydrology and Earth System Sciences*, *21*(2), 1295–1320. https://doi.org/10.5194/hess-21-1295-2017

Zhang, A., Xiao, L., Min, C., Chen, S., Kulie, M., Huang, C., & Liang, Z. (2019). Evaluation of latest GPM-Era high-resolution satellite precipitation products during the May 2017 Guangdong extreme rainfall event. *Atmospheric Research*, *216*(May 2018), 76–85. https://doi.org/10.1016/j.atmosres.2018.09.018

Zhang, J., Fan, H., He, D., & Chen, J. (2019). Integrating precipitation zoning with random forest regression for the spatial downscaling of satellite-based precipitation : a case study of the Lancang – Mekong river basin. *International Journal of Climatology*, (June 2018), 3947–3961. https://doi.org/10.1002/joc.6050

Zorzetto, E., & Marani, M. (2019). Downscaling of rainfall extremes from satellite observations. *Water Resources Research*, *55*(1), 156–174. https://doi.org/10.1029/2018WR022950

APPENDIXES

Appendix 1. List of adopted and eliminated rain gauge stations

Gauge code	Gauge name	Latitude	Longitude	Adopted
2648001	Ilhota - Jusante	-26.9216	-48.8391	No
2648002	Luiz Alves	-26.7241	-48.9316	No
2648038	Gaspar (Montante ETA)	-26.9263	-48.9641	No
2649001	Warnow	-26.9436	-49.2894	No
2649002	Pomerode	-26.7366	-49.1702	Yes (Group 1)
2649003	Benedito Novo	-26.7811	-49.3650	Yes (Group 2)
2649004	Timbó Novo	-26.8297	-49.2719	No
2649005	Indaial	-26.9136	-49.2675	No
2649007	Blumenau (PCD)	-26.9180	-49.0652	Yes (Group 2)
2649009	Garcia	-26.9683	-49.0741	No
2649010	Itoupava Central	-26.7966	-49.0836	No
2649017	Doutor Pedrinho	-26.7172	-49.4830	No
2649053	Witmarsum	-26.9261	-49.8025	No
2649058	Barra do Prata	-26.6970	-49.8280	Yes (Group 2)
2649061	Barragem Norte	-26.8950	-49.6722	Yes (Group 2)
2650022	Iracema	-26.4586	-50.0030	Yes (Group 2)
2650023	Nova Cultura	-26.6930	-50.1477	No
2748000	Brusque (PCD)	-27.1008	-48.9180	No
2749000	Apiuna – Régua Nova	-27.0380	-49.3950	Yes (Group 2)
2749001	Ibirama	-27.0538	-49.5166	No
2749002	Ituporanga	-27.3986	-49.6058	No
2749003	Taió	-27.1130	-49.9944	No
2749005	Nova Bremen Dalbergia	-27.0341	-49.5897	No
2749006	Pouso Redondo	-27.2572	-49.9408	Yes (Group 2)
2749007	Lomba Alta	-27.7305	-49.3827	Yes (Group 2)
2749013	Trombudo Central	-27.2902	-49.7688	Yes (Group 1)
2749016	Neisse Central	-27.0402	-49.3813	Yes (Group 2)
2749017	Barragem Sul	-27.5019	-49.5530	Yes (Group 1)
2749033	Vidal Ramos	-27.3925	-49.3655	No
2749037	Saltinho	-27.6833	-49.3652	No
2749039	Rio do Sul – Novo	-27.2055	-49.6316	Yes (Group 2)
2749041	Agrolândia	-27.4113	-49.8313	No
2749045	Botuvera – Montante	-27.1966	-49.0872	Yes (Group 1)
2749046	Salseiro	-27.3319	-49.3283	Yes (Group 2)
2750014	Barragem Oeste	-27.0972	-50.0338	Yes (Group 2)
2750021	Cabeceira Ribeirão Caetano	-27.1411	-50.2644	No

Appendix 2. Thresholds for rainfall intensity percentiles.

Gauge code	Rainfall thresholds (mm/3days)		
	50th percentile	70th percentile	90th percentile
2649003	3.9	15.2	40.8
2649007	3.1	13.0	39.7
2649058	0.6	12.9	37.3
2649061	1.0	13.6	33.8
2650022	4.6	16.0	38.6
2749000	2.9	12.3	38.2
2749006	3.6	14.8	37.1
2749007	4.1	14.5	37.5
2749016	3.8	14.5	39.9
2749039	3.1	12.4	35.9
2749046	3.3	13.1	36.9
2750014	4.0	16.2	38.1

Appendix 3. Simulated flood peak discharge and total water volume. Results per rainfall scenario and sub-catchment.

Sub-catchment	Flood peak discharge (m3/s)							
	Rainfall scenario							
	SD2	SU2	SD5	SU5	SD10	SU10	SD25	SU25
Itajaí do Sul	522.6	490.7	1,066.4	956.7	1,335.6	1,179.9	1,623.8	1,415.2
Itajaí do Oeste	482.1	490.7	912.4	891.7	1,121.3	1,085.3	1,393.0	1,347.9
Itajaí do Norte	616.0	762.5	1,501.5	1,597.2	1,882.6	1,994.5	2,258.4	2,433.9
Benedito	251.3	276.9	429.8	486.7	527.0	594.0	613.0	689.6
Luiz Alves	83.8	82.2	99.0	109.8	116.0	132.1	135.0	150.3
Itajaí-Mirim	283.1	263.3	834.1	855.2	1,318.9	1,324.3	1,625.6	1,622.1
Itajaí-Açu	2,636.6	2,763.2	5,275.7	5,320.8	6,713.0	6,728.0	8,073.6	8,041.5
Sub-catchment	**Total water volume (hm3)**							
	Rainfall scenario							
	SD2	SU2	SD5	SU5	SD10	SU10	SD25	SU25
Itajaí do Sul	60.3	57.2	153.6	134.1	207.9	180.0	267.7	231.3
Itajaí do Oeste	86.4	79.8	207.6	197.0	287.9	272.0	390.5	369.5
Itajaí do Norte	78.1	90.4	196.2	214.2	269.2	290.3	354.8	381.5
Benedito	36.2	39.1	74.4	87.4	99.0	117.2	127.3	152.3
Luiz Alves	14.3	13.4	27.5	31.8	36.9	44.4	49.5	59.5
Itajaí-Mirim	66.2	59.5	170.7	163.3	298.7	286.6	438.0	424.8
Itajaí-Açu	446.6	446.9	1,023.0	1,023.8	1,426.6	1,426.2	1,933.3	1,933.6

Appendix 4. Quantification of flood hazard. Results per rainfall scenario and sub-catchment, classified by flood depth.

Flood depth	Sub-catchment	Total flooded area (km²)							
		Rainfall scenario							
		SD2	SU2	SD5	SU5	SD10	SU10	SD25	SU25
Below 0.5 m	Itajaí do Sul	26.15	22.95	60.75	58.16	67.18	66.15	79.09	73.30
	Itajaí do Oeste	88.65	72.47	147.72	145.08	153.78	151.47	164.71	162.77
	Itajaí do Norte	28.99	36.75	106.61	112.85	119.56	119.15	124.08	124.94
	Benedito	16.49	21.82	50.50	61.62	69.52	72.07	76.93	75.87
	Luiz Alves	14.39	11.51	47.23	51.53	57.05	49.23	50.13	47.61
	Itajaí-Mirim	60.97	47.62	78.75	77.16	79.97	79.08	81.31	81.80
	Itajaí-Açu	69.05	63.85	138.71	140.52	164.38	166.29	167.53	170.81
0.5 to 1.0 m	Itajaí do Sul	4.52	3.63	18.31	14.13	28.67	22.00	32.73	31.68
	Itajaí do Oeste	1.34	0.74	49.18	44.86	70.32	65.07	77.79	76.89
	Itajaí do Norte	0.55	2.92	19.96	22.90	39.51	45.04	58.38	62.24
	Benedito	0.28	0.37	12.85	12.02	13.02	16.47	22.88	29.95
	Luiz Alves	0.14	0.13	5.10	8.00	10.04	22.66	26.13	33.00
	Itajaí-Mirim	14.31	10.69	29.04	31.98	32.36	31.07	33.53	33.28
	Itajaí-Açu	16.46	18.04	22.15	23.99	37.88	42.39	61.82	63.86
1.0 to 1.5 m	Itajaí do Sul	0.23	0.14	7.07	7.31	11.43	9.29	16.25	13.12
	Itajaí do Oeste	0.07	0.00	11.36	10.39	22.14	20.05	34.29	33.21
	Itajaí do Norte	0.12	0.15	2.98	3.67	9.09	10.65	19.89	21.49
	Benedito	0.00	0.00	1.90	5.99	8.92	10.22	10.03	9.76
	Luiz Alves	0.01	0.01	0.14	0.24	0.59	1.74	2.12	3.94
	Itajaí-Mirim	1.78	0.63	25.75	27.23	25.37	25.48	25.36	23.85
	Itajaí-Açu	2.07	3.54	12.80	13.61	17.02	17.45	33.22	34.28
Above 1.5 m	Itajaí do Sul	0.00	0.00	7.39	2.98	14.64	10.13	25.85	18.68
	Itajaí do Oeste	0.00	0.00	1.14	0.86	10.41	9.20	28.12	22.56
	Itajaí do Norte	0.02	0.09	3.06	3.49	5.49	6.74	13.57	16.48
	Benedito	0.00	0.00	0.15	0.37	1.28	4.27	7.15	11.31
	Luiz Alves	0.00	0.00	0.05	0.08	0.19	0.29	0.61	0.99
	Itajaí-Mirim	0.03	0.00	23.37	12.65	45.99	40.83	68.92	64.07
	Itajaí-Açu	0.37	0.61	27.29	26.74	41.89	42.00	65.14	64.24
Total	Itajaí do Sul	30.90	26.71	93.52	82.58	121.92	107.58	153.92	136.77
	Itajaí do Oeste	90.07	73.22	209.40	201.19	256.65	245.80	304.92	295.43
	Itajaí do Norte	29.68	39.91	132.61	142.91	173.65	181.59	215.92	225.15
	Benedito	16.77	22.19	65.40	80.00	92.73	103.03	116.99	126.88
	Luiz Alves	14.54	11.65	52.52	59.85	67.87	73.91	78.99	85.53
	Itajaí-Mirim	77.09	58.94	156.91	149.01	183.69	176.46	209.13	203.00
	Itajaí-Açu	87.96	86.04	200.94	204.86	261.17	268.14	327.70	333.19

Appendix 5. Quantification of flood exposure. Results per rainfall scenario and sub-catchment, classified by flood depth.

Flood depth	Sub-catchment	Total exposed urban area (km²)							
		Rainfall scenario							
		SD2	SU2	SD5	SU5	SD10	SU10	SD25	SU25
Below 0.5 m	Itajaí do Sul	0.96	0.96	1.28	1.42	1.30	1.36	1.61	1.26
	Itajaí do Oeste	3.60	2.97	3.04	3.05	2.53	2.79	1.96	1.75
	Itajaí do Norte	0.89	0.99	0.82	0.79	0.77	0.69	0.56	0.57
	Benedito	2.96	3.34	2.91	2.93	3.02	3.00	3.01	3.14
	Luiz Alves	0.69	0.69	0.75	0.64	0.39	0.40	0.39	0.42
	Itajaí-Mirim	14.27	11.09	12.86	12.92	11.04	10.96	9.30	9.60
	Itajaí-Açu	19.23	18.99	21.65	21.83	21.88	21.15	18.59	18.92
0.5 to 1.0 m	Itajaí do Sul	0.36	0.26	0.48	0.50	0.55	0.50	0.76	0.56
	Itajaí do Oeste	0.03	0.01	1.72	1.61	2.17	1.82	1.97	2.04
	Itajaí do Norte	0.00	0.02	0.85	0.88	0.48	0.58	0.68	0.67
	Benedito	0.02	0.03	1.94	1.39	1.23	1.15	1.45	1.53
	Luiz Alves	0.00	0.00	0.12	0.29	0.61	0.64	0.65	0.60
	Itajaí-Mirim	2.52	2.58	8.03	9.08	6.59	6.76	5.47	5.24
	Itajaí-Açu	2.24	1.94	5.38	5.71	7.71	9.13	11.74	12.11
1.0 to 1.5 m	Itajaí do Sul	0.00	0.00	0.39	0.30	0.33	0.47	0.41	0.38
	Itajaí do Oeste	0.01	0.00	0.82	0.82	0.80	0.78	1.28	1.25
	Itajaí do Norte	0.00	0.00	0.03	0.07	0.64	0.64	0.68	0.67
	Benedito	0.00	0.00	0.49	1.43	1.72	1.41	1.33	1.19
	Luiz Alves	0.00	0.00	0.00	0.01	0.01	0.03	0.04	0.15
	Itajaí-Mirim	0.92	0.35	6.38	4.84	7.33	7.57	5.52	5.74
	Itajaí-Açu	0.40	057	2.72	2.99	4.86	5.05	7.20	7.21
Above 1.5 m	Itajaí do Sul	0.00	0.00	0.69	0.50	1.18	0.82	1.61	1.26
	Itajaí do Oeste	0.00	0.00	0.30	0.25	1.18	1.17	1.96	1.75
	Itajaí do Norte	0.00	0.00	0.01	0.02	0.04	0.06	0.42	0.56
	Benedito	0.00	0.00	0.02	0.03	0.22	0.19	1.46	2.13
	Luiz Alves	0.00	0.00	0.00	0.00	0.00	0.01	0.01	0.01
	Itajaí-Mirim	0.00	0.00	4.56	3.82	12.32	11.01	20.44	19.54
	Itajaí-Açu	0.03	0.00	6.29	6.19	11.14	11.18	18.51	18.30
Total	Itajaí do Sul	1.32	1.22	2.84	2.72	3.36	3.14	3.72	3.51
	Itajaí do Oeste	3.65	2.98	5.87	5.73	6.69	6.56	7.63	7.47
	Itajaí do Norte	0.90	1.01	1.71	1.75	1.92	1.97	2.14	2.20
	Benedito	2.99	3.37	5.36	5.77	6.19	6.75	7.26	7.99
	Luiz Alves	0.69	0.69	0.87	0.94	1.02	1.08	1.09	1.19
	Itajaí-Mirim	17.74	14.02	31.83	30.67	37.29	36.31	40.72	40.11
	Itajaí-Açu	21.93	21.66	36.04	36.73	45.59	46.52	56.04	56.55